VOLUME 38 JULY 1960 NUMBER 7

Canadian Journal of Physics

Editor: H. E. DUCKWORTH

Associate Editors:

L. G. ELLIOTT, *Atomic Energy of Canada, Ltd., Chalk River*
J. S. FOSTER, *McGill University*
G. HERZBERG, *National Research Council of Canada*
L. LEPRINCE-RINGUET, *Ecole Polytechnique, Paris*
B. W. SARGENT, *Queen's University*
G. M. VOLKOFF, *University of British Columbia*
W. H. WATSON, *University of Toronto*
G. A. WOONTON, *McGill University*

Published by THE NATIONAL RESEARCH COUNCIL

OTTAWA CANADA

CANADIAN JOURNAL OF PHYSICS

Under the authority of the Chairman of the Committee of the Privy Council on Scientific and Industrial Research, the National Research Council issues THE CANADIAN JOURNAL OF PHYSICS and five other journals devoted to the publication, in English or French, of the results of original scientific research. Matters of general policy concerning these journals are the responsibility of a joint Editorial Board consisting of: members representing the National Research Council of Canada; the Editors of the Journals; and members representing the Royal Society of Canada and four other scientific societies.

EDITORIAL BOARD

Representatives of the National Research Council

I. McT. Cowan (Chairman), *University of British Columbia*
L. Marion, *National Research Council*
H. G. Thode, *McMaster University*
D. L. Thomson, *McGill University*

Editors of the Journals

D. L. Bailey, *University of Toronto*
T. W. M. Cameron, *Macdonald College*
H. E. Duckworth, *McMaster University*
Léo Marion, *National Research Council*
J. F. Morgan, *Department of National Health and Welfare, Ottawa*
R. G. E. Murray, *University of Western Ontario*
J. A. F. Stevenson, *University of Western Ontario*

Representatives of Societies

D. L. Bailey, *University of Toronto*
Royal Society of Canada
T. W. M. Cameron, *Macdonald College*
Royal Society of Canada
H. E. Duckworth, *McMaster University*
Royal Society of Canada
Canadian Association of Physicists
P. R. Gendron, *University of Ottawa*
Chemical Institute of Canada
D. J. Le Roy, *University of Toronto*
Royal Society of Canada
J. F. Morgan, *Department of National Health and Welfare, Ottawa*
Canadian Biochemical Society
R. G. E. Murray, *University of Western Ontario*
Canadian Society of Microbiologists
J. A. F. Stevenson, *University of Western Ontario*
Canadian Physiological Society

Ex officio

Léo Marion (Editor-in-Chief), *National Research Council*
J. B. Marshall (Administration and Awards), *National Research Council*

Manuscripts for publication should be submitted to Dr. H. E. Duckworth, Editor, Canadian Journal of Physics, Hamilton College, McMaster University, Hamilton, Ontario.
For instructions on preparation of copy, see **NOTES TO CONTRIBUTORS** (back cover).

Proof, correspondence concerning proof, and orders for reprints should be sent to the Manager, Editorial Office (Research Journals), Division of Administration and Awards, National Research Council, Ottawa 2, Canada.

Subscriptions, renewals, requests for single or back numbers, and all remittances should be sent to Division of Administration and Awards, National Research Council, Ottawa 2, Canada. Remittances should be made payable to the Receiver General of Canada, credit National Research Council.

The journals published, frequency of publication, and subscription prices are:

Canadian Journal of Biochemistry and Physiology	Monthly	$9.00 a year
Canadian Journal of Botany	Bimonthly	$6.00 a year
Canadian Journal of Chemistry	Monthly	$12.00 a year
Canadian Journal of Microbiology	Bimonthly	$6.00 a year
Canadian Journal of Physics	Monthly	$9.00 a year
Canadian Journal of Zoology	Bimonthly	$5.00 a year

The price of regular single numbers of all journals is $2.00.

Canadian Journal of Physics

Issued by THE NATIONAL RESEARCH COUNCIL OF CANADA

VOLUME 38 JULY 1960 NUMBER 7

THERMAL AND ELECTRICAL PROPERTIES OF ARMCO IRON AT HIGH TEMPERATURES[1]

M. J. LAUBITZ

ABSTRACT

Thermal and electrical conductivity, thermoelectric power vs. platinum, and thermal expansion of Armco iron were determined in the temperature range of 0° C to 1000° C. All these properties show a discontinuous change at the $\alpha-\gamma$ transition of iron, and a change in slope at the Curie point. These measurements were carried out as a contribution to a co-operative determination of thermal conductivity of Armco iron at high temperatures.

1. INTRODUCTION

The thermal and electrical properties of iron at high temperatures have been repeatedly measured in the past. The agreement between the various experimental results is on the whole quite satisfactory. The one exception is the thermal conductivity, particularly at temperatures above the Curie point. So far three experimenters have published results of measurements of thermal conductivity at temperatures above 800° C. These are Maurer (1936), Powell (1939), and Lucks and Deem (1958). Powell made both comparative measurements for a linear heat flow and absolute measurements for radial flow in a cylinder. Maurer made absolute measurements for linear heat flow and Lucks and Deem comparative measurements for linear heat flow. Oddly, and perhaps significantly, none of the experimenters give estimates of the error, but at 1000° C their results differ by 27% of the mean value.

The situation is much better below the Curie point. Three further determinations have been done in the range of 0° C to 800° C, all absolute and with linear heat flow, by Powell (1934), Hattori (1937), and Armstrong and Dauphinee (1947). These authors do give estimates of their experimental error which are less than 2% for the results of Powell, 1.95% for Armstrong and Dauphinee, and 0.8% for Hattori. The maximum spread of results, between Armstrong and Dauphinee and Hattori, is 5.3% of the average at 30° C and 9.7% at 700° C, much larger than the sum of the quoted errors. There is, of course, the possibility that at least part of the discrepancy in the experimental results, particularly at lower temperatures, is due to the

[1]Manuscript received March 3, 1960.
Contribution from the Division of Applied Physics, National Research Council, Ottawa, Canada.
Issued as N.R.C. No. 5713.

variation in the chemical composition of the samples (Table I), but it is inconceivable that it could account for the large spread at high temperatures.

TABLE I

Chemical composition of the specimen of Armco iron used in experiments

Observer	Percentage composition of iron							
	C	Si	Mn	P	S	Cu	Ni	Fe (by difference)
Powell	0.023	0.007	0.025	0.007	0.020	—	—	99.918
Maurer	0.01	trace	0.02	0.011	0.040	0.05	—	99.87
Hattori	0.015	0.010	0.032	0.003	0.030	0.013	—	99.897
Armstrong and Dauphinee	0.028	—	0.035	—	0.039	0.067	0.024	99.807
Laubitz*	0.02	0.004	0.030	0.006	0.023	0.083	—	99.83

*As given by the distributor.

To resolve this conflict of experimental results, C. F. Lucks of the Battelle Memorial Institute proposed a co-operative measurement of thermal conductivity of Armco iron. Four laboratories agreed to participate: the National Physical Laboratory, Teddington, England, the National Bureau of Standards, Washington, U.S.A., the Battelle Memorial Institute, Columbus, U.S.A., and the National Research Council, Ottawa, Canada. The Battelle Memorial Institute obtained the specimen of Armco iron in the shape of 1 in. diameter rods, annealed them for half an hour at 850° C, and distributed them to the participants. This laboratory received a 12 in. long section marked No. 4 and No. 5 at its ends. The sample for the experiment was cut out from the middle of the section and X-rayed. The radiograph revealed no cracks or non-uniformities. The thermal and electrical conductivity and the thermoelectric power measurements were made on this sample. The thermal expansion measurements were made on another piece of Armco iron. The method, results, and errors are discussed separately for each of the properties in the following section.

2. METHOD, RESULTS, AND THEIR ERROR

2.1. Thermal Conductivity

Experimental Method

When Battelle proposed the co-operative thermal conductivity measurement, they suggested as an aim the determination of the conductivity in the temperature range of 0° C to 1000° C, with an experimental accuracy of 3.5% or better. However, the dimensions of the sample supplied were not ideally suited to such an experiment. They necessarily forced the adoption of a linear heat flow method, without giving quite enough room to make sure that the flow was rectilinear. The relatively small diameter of the sample made it difficult to devise a heat source that was truly uniform, particularly near the edges, and limited the temperature measurements to the surface of the sample, where the edge non-uniformities of the heat source have the greatest effect. When possible errors due to these effects were estimated, it was seen

that the conventional matched guard technique was not good enough to ensure an error less than 3% at 1000° C. The matching error is, of course, dependent on the geometrical ratios and thermal parameters of the components employed in the apparatus; for a reasonable system designed around the specimen supplied, the error due to a single guard is about 0.2% for perfect lateral guard and sample temperature matching at three points, and increases by about 0.5% for each degree of lateral mismatch. One cannot expect to match the sample and guard temperatures to less than 4° C at 1000° C (see, for instance, the experimental results of Powell (1934)), which puts the mismatch error alone at about 2%. To eliminate this error a method was developed that does not depend on temperature matching of sample and guard. A brief description of the method is here given with reference to the actual experimental arrangement, as shown in Figs. 1 and 2. An exact mathematical analysis is given in the Appendix.

The sample, which is in two halves, and its environment is shown in Fig. 1. There, (4) and (8) are the top and bottom parts of the sample, each of length 7.156 cm and diameter 2.324 cm; (6) is a thin central heater between them, equipped with current and potential leads; (1) and (11) are the heat sinks. The contact surfaces between the sample, the central heater, and the heat sinks (e.g. (9) and (17)) were coated with high purity tin and sweated together. Each part of the sample had three thermocouples (5) wedged into small holes (0.4 mm in diameter and 0.5 mm deep) in it that were in a straight line at 3-cm intervals, the central thermocouple being equidistant from the heater and the sink. The thermocouples, Pt/Pt–10% Rh 0.25 mm in diameter, were inserted into fine alumina tubes, taken halfway around the sample at the level of the point of contact and then brought out through the bottom heat sink.

Around the sample was an alumina guard (7), with an internal diameter of 4.96 cm. Five heaters (15) were wound on the outside of the guard, and six thermocouples (16) were positioned opposite the sample thermocouples. These thermocouples were taken halfway around the guard before they were brought out sideways through the radiation shields surrounding the guard. Grounded wires (14) were cemented to the guard on either side of the thermocouples to minimize leakage from the heaters. Around the guard were several radiation shields supported between the end plates (3) and (13). End heaters (12) and (18) were wound on the top and bottom sinks to control the temperature of the samples; these had several radiation shields around them ((2) and (10)). The space between the guard and sample was filled with fine alumina powder, and the whole arrangement was placed in vacuum, as shown in Fig. 2. Here (3) is the water-cooled vacuum vessel, with the port (5) connected to a pumping system having a pumping speed of 200 l/sec at 10^{-5} mm Hg. Both the top and bottom sinks had a constriction in them (2) to limit the loss of heat at high temperatures, and had water cooling provided (4) to withdraw heat at lower temperatures. Pressure was applied vertically to the sample by a spring (1) to maintain good thermal contact at temperatures above the melting point of the tin on the contact faces of the sample. All the

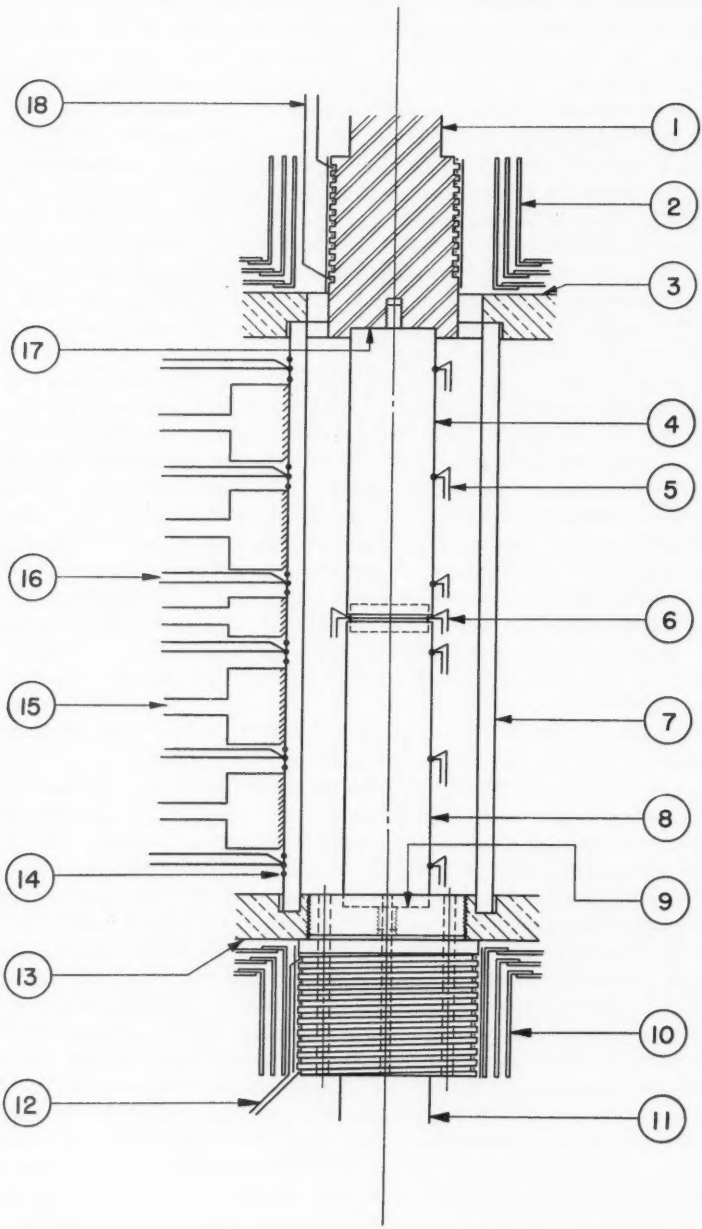

FIG. 1. Experimental arrangement of the sample and guard.

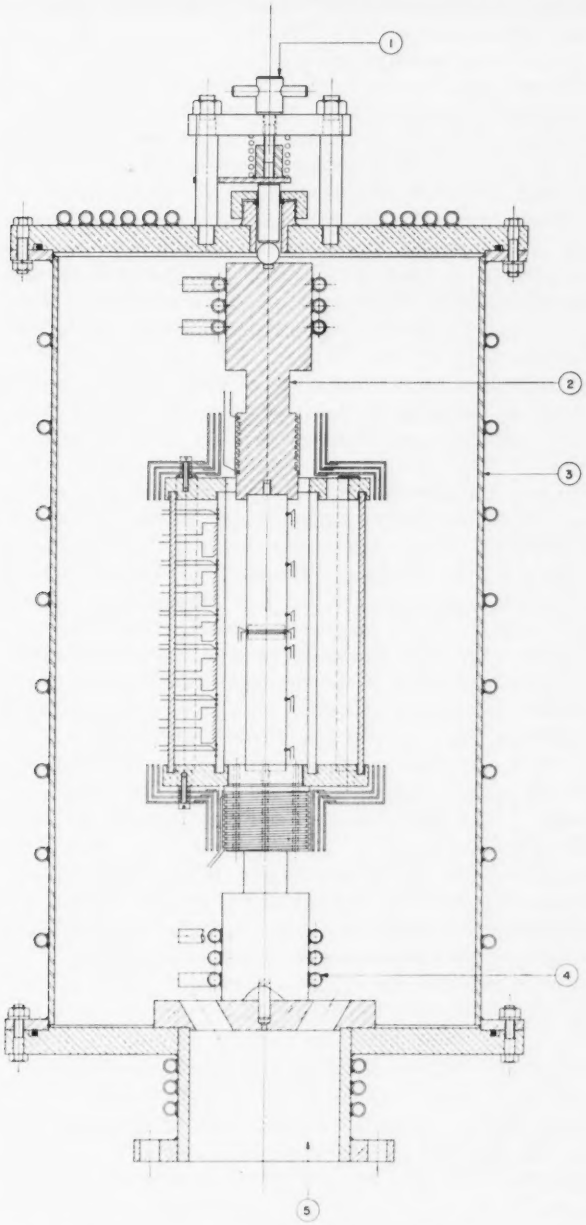

FIG. 2. Arrangement of the sample guard system in the vacuum vessel.

heater and thermocouple leads were brought out through the bottom of the vacuum vessel through kovar seals. The heaters were controlled by variacs powered from isolating transformers connected to a stabilized voltage source. The thermocouple e.m.f.'s were fed into a 12-point recording potentiometer for rough measurements; at thermal equilibrium the e.m.f.'s were switched over to a Wenner potentiometer and measured to 1/10th of a microvolt. The vacuum, as measured by an ionization gauge, was 2×10^{-6} mm Hg at room temperature and 3×10^{-5} mm Hg at 1000° C.

In the unmatched guard method the sample and guard are treated mathematically as a single system. The system must fulfil four conditions:

(1) That the plane through the center of the central heater and coplanar with it be a plane of zero longitudinal temperature gradient for the system.

(2) That the medium between sample and guard have a conductive mode of heat transfer.

(3) That the temperature at each of the sink ends of the system be uniform.

(4) That the temperature variation of the conductivities of all the components of the system be small for such temperature differences as may exist in the system.

Under these conditions the determination of the thermal conductivity involves two sets of temperature readings, with and without power developed in the central heater. These readings were taken as follows: The end heaters ((12) and (18) in Fig. 1) and the guard heaters were adjusted until the sample was at the desired temperature and the plane through the central heater was a plane of zero longitudinal temperature gradient. When thermal equilibrium was reached, the e.m.f.'s of the six sample thermocouples and the six guard thermocouples were measured in a set order at fixed time intervals. Two sets of readings were taken, the readings for each thermocouple being 12 minutes apart. (These fixed time intervals permitted the calculation of a correction for possible time variations in temperature.) Then, the central heater was switched on, dissipating approximately 30 watts. The power was measured with a Weston Model 310 wattmeter, and was corrected for the power loss in the wattmeter. The power to the end heaters was reduced so that the temperature of the sink ends of the sample did not change appreciably, and the end heaters were then adjusted so that the central plane remained a plane of zero longitudinal temperature gradient. The heaters on the guard remained untouched during this procedure. At equilibrium, two sets of temperature readings again were taken. Under these conditions the surface temperatures of each half of the sample are given by

$$(1) \qquad \Delta T(z)-\Delta T(L) = GL(1-z/L)-\sum_{n=0}^{\infty} A_n \cos\,(n+\tfrac{1}{2})\,\frac{\pi z}{L}$$

where z is the distance measured along the axis of the sample, $z=0$ corresponding to the plane of zero longitudinal temperature gradient, L is the length of each half of the sample, $\Delta T(z)$ is the difference between the temperatures measured on the surface of the sample at height z with the central heater

on and off, and G is the gradient *due to the central heater* set up in each half of the sample, so that

$$\dot{Q} = KA(G_t+G_b) \tag{2}$$

where $\dot{Q}$ is the power input into the central heater, A is the cross-sectional area of the sample, and K is the average conductivity of the sample. The subscripts t and b refer to the top and bottom half of the sample. It may as well be mentioned here that G ranged from 6 to 10° C/cm, and that the average temperature of the two parts of the sample never differed by more than 4° C.

As shown in the Appendix, the infinite series in equation 1 converges rapidly for $K_s/K_p > 100$, where K_s is the sample conductivity and K_p is the conductivity of the powder between the guard and sample. In our experiment $K_s/K_p \sim 1000$, for which $A_0/GL \sim 2\times10^{-2}$ and $A_1/GL \sim 2\times10^{-4}$, and therefore equation 1 can be written as

$$\Delta T(z)-\Delta T(L) = GL(1-z/L)-A_0\cos(\pi z/2L)-A_1\cos(3\pi z/2L). \tag{3}$$

The temperature being measured at three points, three unknowns could be evaluated from equation 3. These would normally be G, $\Delta T(L)$, and A_0. However, as $\Delta T(L)$ was kept very small, about 1° C to 3° C, a different calculating procedure was employed: $\Delta T(L)$ was extrapolated from the measured $\Delta T(z)$ by the equation

$$\Delta T(z) = a(L-z)^2+b(L-z)+c.$$

This should give a very good approximation to the true $\Delta T(L)$ as the gradient in the sample is almost linear, and $(L-z_3)$ is small, z_3 being the position of the thermocouple nearest the sink. The calculated $\Delta T(L)$ was then used to determine A_0 and A_1 from equation 3, and G was subsequently calculated from a modified form of equation 3:

$$\Delta T(z_1)-\Delta T(z_3) = G(z_3-z_1)-A_0(\cos\pi z_1/2L-\cos\pi z_3/2L) \\ -A_1(\cos 3\pi z_1/2L-\cos 3\pi z_3/2L). \tag{4}$$

This calculating procedure giving A_1 as well as A_0 was employed not from any mistaken idea of improving the accuracy of G, but to obtain an estimate of the correspondence of the experiment with theory. The theory gives definite expressions for the A_n's in terms of the geometry of the system and the conductivity ratios K_s/K_p. However, as K_p is known only very approximately the agreement between theory and experiment can be judged solely by the ratios of the A_n's, and not their absolute value.

It can be seen from the preceding description of the method that the guard does not play an important role in the measurements. It is there merely to help establish the plane of zero temperature gradient across the system, and to keep the temperature of the whole system reasonably uniform, so that the temperature variations in the thermal conductivity of the components of the system is small.

The actual experiment consisted of four separate runs, made with three sets of thermocouples and two different central heaters. The outside dimensions of the two central heaters were the same, 2.2 cm in diameter and 0.6 cm thick. One of them, however, was made out of steel, very much like that of Powell (1934). The other one was made out of alumina, into the middle of which was sintered a fine coil of Pt–20% Rh wire going in zigzags right across the heater. Two platinum disks were sintered onto each face of the central heater, so that it could be tinned to the sample. Although the ceramic heater was the stronger of the two mechanically, the temperature distributions across its faces were not as good as for the steel heater.

The experiments were done in the following order. First run: ceramic central heater, first set of thermocouples. Second run: ceramic central heater, second set of thermocouples, position of the two parts of the sample interchanged. Third run: steel central heater, second set of thermocouples, sample positioned as in second run. Fourth run: steel central heater, third set of thermocouples, sample position as in second run. The sample, sink, and central heater surfaces were retinned before each run. The thermocouple separations and their actual distances from the sink were measured before and after each run. The thermocouple separations were measured by passing a d-c. current through the sample and comparing the e.m.f.'s across the thermocouples to those across a knife-edge standard. The standard was placed against that half of the sample for which the thermocouple separation measurements were made in three different azimuthal positions relative to the thermocouples. The separation of the knife edges of the standard was approximately 6 cm, its exact value being measured with a travelling microscope before and after each set of measurements. The distance from thermocouple to sink was also measured electrically, the d-c. e.m.f. between any one of the thermocouples and a needle probe placed at the joint of sample and sink being compared with the e.m.f. across the thermocouples. From the known dimensions of the sample and central heater the distance of the thermocouples from the plane of zero longitudinal temperature gradient could be calculated. All the electrical measurements were done with the complete system assembled, except that if the ceramic central heater was to be used, a copper plug would be substituted for it. The sample dimensions were also checked before and after every run.

Experimental Results

The results obtained in the four runs are shown in Fig. 3, together with those of Powell, Maurer, and Lucks and Deem. The results as shown have had two corrections applied to them. The first was a correction for the non-uniform power distributions of the central heaters. This was done by measuring the surface temperature variation of each heater along two mutually perpendicular diameters, under conditions approximating those of the experiment. These measured temperature distributions, $T'(r, \theta)$, were fitted by Bessel functions

$$T'(r, \theta) = C\left[1+\sum_n \sum_l A_{n,l} J_n(m_l r) \cos n(\theta-\alpha)\right]$$

where θ is measured with respect to the position of the sample thermocouples, C is a constant, and the m's are so chosen that $J_n'(m_l a) = 0$, a being the radius of the central heater. Usually four terms with $n < 3$ were sufficient to obtain a good fit. Under the assumption of no heat loss from the surface of the sample, the sample surface temperatures will be given by

$$T(a, z, \theta) = GL\left[(1-z/L)+\sum_n \sum_l A_{n.l}\, J_n(m_l a) \cos n(\theta-\alpha) \times \sinh m_l(L-z)\right]$$

from which the required correction could be calculated. These were:

ceramic heater, top surface	$G_0 = 1.027\, G$
ceramic heater, bottom surface	$G_0 = 1.007\, G$
steel heater, top surface	$G_0 = 1.001\, G$
steel heater, bottom surface	$G_0 = 0.992\, G$

where G is the temperature gradient as calculated from equation 4 and G_0 is the corrected gradient. The correction factors are unfortunately not very accurate, due to the difficulty in obtaining meaningful surface temperature distributions. Successive traverses along one line differed by a magnitude equivalent to 10% of GL, which, if the correction factor is represented by $(1+\Delta)$, represent an uncertainty in Δ of 25%.

The other correction deals with deviations from thermal equilibrium. In the experiment, the thermocouple e.m.f.'s were recorded, so that their time variations were easily observed. It was noticed that after every change in the heaters the thermocouples would quickly settle down relative to each other, usually in the order of 30 to 60 minutes, while frequently there was a slow, uniform drift of all the thermocouples which, at high temperatures, was difficult to eliminate, but very easy to correct for. The correction calculated for linear heat flow with the suitable boundary conditions, is

$$G_0' = G_0+\left[\left(\frac{\Delta T}{\Delta t}\right)_G-\left(\frac{\Delta T}{\Delta t}\right)_0\right]\left(\frac{z_3+z_1}{2\alpha}+\frac{\Delta t_1}{z_3-z_1}\right)$$

where G_0' is the corrected and G_0 the uncorrected gradient, $\Delta T/\Delta t$ is the average rate of temperature change for each half of the sample, the subscripts G and 0 referring to the readings with the central heater on and off, respectively. α is the thermal diffusivity of iron, and Δt_1 is the time interval between the readings at $z = z_1$ and $z = z_3$. As the thermocouples were read in a specified order at fixed time intervals, the correction was easy to evaluate. The largest correction made was 0.7%, and the average 0.06%.

It can be seen in Fig. 3 that the corrected experimental points lie on two distinct curves, one for each of the central heaters, while there is no significant difference associated with the different sets of thermocouples used. The results for the ceramic and steel central heaters overlap in the range of 400° C to 800° C, where the difference between the two sets is $(3.4\pm0.3)\%$ of their average. Equal weight was given to the two sets of results, for although there

were more points taken with the ceramic central heater, the correction that had to be applied to them due to the non-uniformity of the power input was larger than that applied to the points taken with the steel heater. (As a matter of fact, the two sets of results were separated by only 1.4% when uncorrected, the set for the steel central heater being higher than that for the ceramic central heater. The power distribution correction pushed the ceramic heater results further down by approximately 1.7%, and the steel heater results further up by approximately 0.4%.) The average value for the thermal conductivity was taken as equal to the mean of the two sets in the temperature range 400° C to 800° C, as 1.017 times the value for the ceramic central heater in the temperature range of 0° C to 400° C, and as 0.983 times the value for the steel central heater in the range 800° C to 1000° C. The average value so computed is shown in Fig. 3, and is given in Table II together with

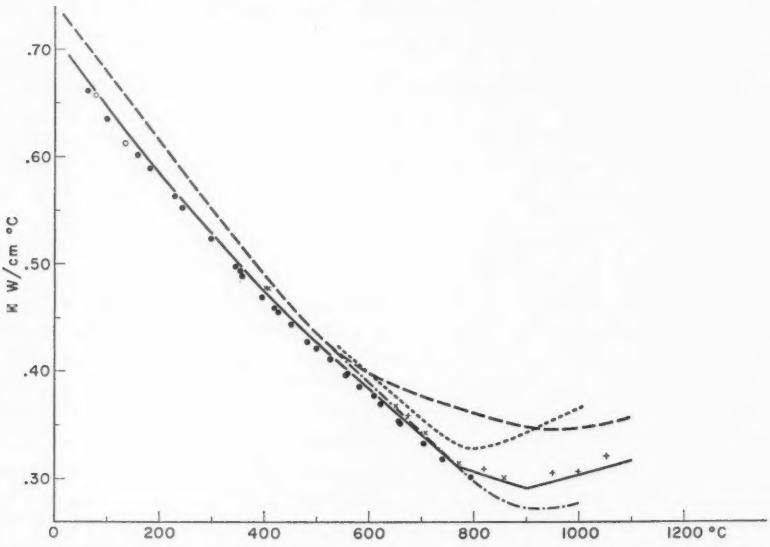

FIG. 3. Thermal conductivity of Armco iron as a function of temperature: ○ experimental points of the first run; ● experimental points of the second run; × experimental points of the third run; + experimental points of the fourth run; —— average value for this experiment; — — Maurer's results; — · — Powell's results; - - - results of Lucks and Deem.

the values of the other experimenters. The values listed in Table II are not corrected for the thermal expansion of iron.

Experimental Error

The uncertainties in the determination of the thermal conductivity will be discussed with reference to equations 2 and 4. There are two uncertainties associated with the determination of the thermal conductivity, K, as a function of temperature: the probable error in the determination of K, and the probable

TABLE II

The thermal conductivity of Armco iron as given by various observers

	Thermal conductivity, K, in watts/°C cm					
T, °C	Powell	Maurer	Hattori	Armstrong and Dauphinee	Lucks and Deem	Laubitz
30	.724	.724	.703	.741		.691
100	.682	.674	.665	.693		.647
200	.615	.611	.598	.625		.584
300	.552	.548	.531	.557		.528
400	.485	.490	.469	.493		.474
500	.433	.435	.414	.442	.444*	.427
600	.389	.398	.385	.392	.393*	.383
700	.343	.377	.377	.342	.360*	.340
800	.297	.360	—	—	.326*	.305
900	.272*	.347	—	—	.347*	.291
1000	.276*	.347	—	—	.364*	.303

*Taken from graph.

error in the measurement of the temperature to which K is supposed to correspond. In this experiment, the average of the readings of the four extreme thermocouples of the two halves of the sample, measured with the central heater on, was taken as the temperature of that particular point. Thus, individual errors in the thermocouples tend to average out, and the main error arises from the composition of that particular lot of wire from which the thermocouples were made. Deviations due to wire composition are usually less than 5° C and 1000° C, and therefore the uncertainty in the temperature should not exceed 0.5%. Effects due to contamination, cold work, etc., of the thermocouples appear negligible in view of the agreement of the results for the various sets of thermocouples, and for points taken at the same temperature at the beginning and the end of a run.

The uncertainty in K arises from uncertainties in the measurement of $\dot{Q}$, A, and G. $\dot{Q}$, the power input, was measured with a calibrated precision wattmeter, with an error less than 0.2% of full scale. For the power input used in the experiment the wattmeter read at the midpoint of its scale, and therefore the uncertainty in $\dot{Q}$ is less than 0.4%. A, the cross-sectional area, was measured before and after each run. The maximum change in A observed during a run was 0.26%, which introduces an uncertainty in A of not more than 0.13%.

The uncertainty in G, the measured temperature gradient, is more difficult to evaluate. It arises due to errors and uncertainties in the parameters entering into equation 4 directly, and from the experimental non-conformity to the conditions assumed in deriving equation 4. Into the first category fall the uncertainties in the temperature differences $\Delta T(z_1)$, and the thermocouple separation (z_3-z_1). The uncertainties in the absolute values of z are not important, as the correction term in A_0 and A_1 are less than 3% of $G(z_3-z_1)$. The $\Delta T(z_1)$, being a small temperature difference of a given thermocouple, should have a fractional error no larger than the fractional error in the temperature measurement, that is 0.5%. As $\Delta T(z_3)$ is small compared to $\Delta T(z_1)$, the uncertainty in $\Delta T(z_1)-\Delta T(z_3)$ is only slightly larger than the uncertainty

in $\Delta T(z_1)$, about 0.6%. The thermocouple separation was measured with a precision of 0.2%, but it was found that the numerical value would change during a run, on the average, by 0.8%, presumably due to changes in the tinned contacts of the sample. The uncertainty in z_1-z_3 is therefore of the order of 0.6%.

There are several factors contributing to the deviation of the experiment from theory. First, there is the finite size of the central heater. This, however, turns out to be negligible; according to a simplified calculation, the ceramic central heater affects the temperature distribution in the sample by less than 0.01%. Then there is the non-uniformity of heat input of the central heater. A correction has been made for this, but the correction factor itself is accurate only to 0.5%. There is also the non-uniformity of the contacts of the sample with the central heater and the sinks. It has been found that with all the interfaces freshly tinned and carefully joined, the measured thermocouple separation is a function of the azimuthal position of the standard, the variation being of the order of 1.2%, and that the change of such an azimuthal variation during a run is of the same magnitude. By taking as the thermocouple separation the average value for several azimuthal positions of the standard, the effect of the variation is wiped out. The change in the variation, however, does introduce an uncertainty of half the observed change, 0.6%. There may be, of course, also a radial variation of the quality of the contacts; the magnitude of the uncertainty that this would introduce is not known, but one may expect it to be comparable to the uncertainty due to the azimuthal variation, that is approximately 1.2%.

Finally, there will be deviation of experiment from theory due to such factors as non-uniformity of thermal conductivity of the powder separating guard and sample, non-uniformity of sink temperatures, lack of radial symmetry in the guard, etc. These are the most difficult to calculate, but an estimate can be made from the ratio of A_0/A_1 calculated from equation 3. Figure 4 gives the experimental value of $\beta_n(K_1/K_2)$, where

$$\beta_n(K_1/K_2) = A_n/GL$$

and $K_1 \equiv K_s$, $K_2 \equiv K_p$, and Fig. 9 in the Appendix gives β_n as a function of K_1/K_2. The experimental β_0 is approximately $+1.2\times10^{-2}$, and β_1 is between 0 and -0.6×10^{-2}, while, according to theory, all β_n's are positive, and for the above value of β_0, β_1 should be of the order of 10^{-4}. We can therefore say that the uncertainty in G is at least of the order of β_1 experimental, and probably more, of the order of twice β_1, which amounts to 1.2%. Of course, part of that uncertainty is probably caused by factors considered earlier, which does complicate the assessment of the total probable error. However, it was felt that the square root of the sum of squares of the individual uncertainties would probably be a fair indication of the accuracy of the measurement. Calculated that way, the over-all uncertainty in K is 2.1%. The 0.5% uncertainty in the temperature associated with K can be interpreted as a further error in K, increasing the latter to about 2.2% at 100° C and 2.5% at 800° C. The observed difference of 3.4% between the results for the two central heaters is therefore well within the estimated uncertainty in K.

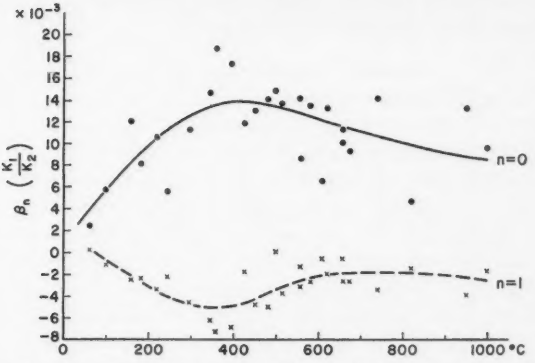

FIG. 4. Experimental values of the coefficients $\beta_n = A_n/GL$, for $n = 0$ and $n = 1$.

The over-all experimental uncertainty should not be confused with the precision of the results for each run. Thus, for the ceramic central heater, the maximum deviation of a point from the smooth curve drawn through all the points was 1.9%, and the r.m.s. deviation from that curve only 0.48%. For the steel heater, the maximum deviation from the curve was 0.9%, and the r.m.s. deviation 0.47%.

2.2. Electrical Resistivity

The electrical resistivity was measured during and after the last run with the steel central heater. Measurements were done with the sample in thermal equilibrium, and the heaters so adjusted that the temperature throughout the sample did not vary by more than 5° C. The measurement involved passing a d-c. current through the sample, and comparing the e.m.f. across the two platinum legs of the outside thermocouples of each part of the sample with the e.m.f. across a standard resistor in series with the sample. Six measurements were done at each temperature for each half of the sample, the current being reversed after every measurement. The average value at any temperature for both halves of the sample is shown in Fig. 5. The r.m.s. deviation from the curve drawn through these "average" points is 0.59% for one half of the sample, and 0.67% for the other, while the r.m.s. difference between the points of the two halves of the sample is 0.69. This indicates that there is no consistent difference between the results for the two halves.

The average value of the resistivity is given in Table III. Also given in there are Powell's results for his sample and, for purposes of comparison, the results obtained on high purity iron wire by Wallace, Sidles, and Danielson (1960). The average value of the resistivity was used in the calculation of the Lorentz function, L, which is shown in Fig. 5, together with the Lorentz function calculated by Powell for his specimen.

The uncertainties in the values assigned for the electrical conductivity come from the error in the determination of the ratio of the e.m.f. measured across the sample to the e.m.f. of the standard, and from the uncertainties in the cross-sectional area of the sample, in the separation of the thermocouples, and

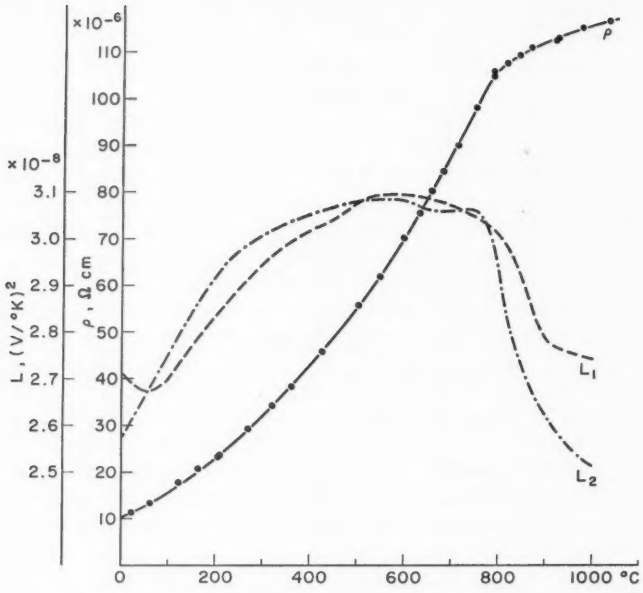

FIG. 5. The electrical resistivity and Lorentz function of Armco iron: ● experimental points of the electrical resistivity, ρ; L_1 Lorentz function calculated from the results of this experiment; L_2 Lorentz function obtained by Powell.

TABLE III

Electrical resistivity and the Lorentz function of Armco iron

	Electrical resistivity, Ω cm			Lorentz function $(V/°K)^2$	
	Armco iron		High purity		
T, °C	Laubitz	Powell	iron	Laubitz	Powell
0	10.4×10^{-6}	9.59×10^{-6}	—	2.71×10^{-8}	2.59×10^{-8}
100	15.6	15.1	14.69×10^{-6}	2.70	2.76
200	22.9	22.6	21.89	2.83	2.93
300	32.0	31.4	30.97	2.95	3.01
400	42.9	43.1	41.82	3.02	3.06
500	55.7	55.2	54.39	3.08	3.08
600	70.3	69.9	68.87	3.09	3.08
700	87.9	87.0	85.85	3.07	3.06
800	106.0	105.5	104.33	3.01	2.93
900	112.0	112.3*	110.78	2.77	2.62*
1000	115.3	115.4*	114.49	2.74	2.51*

*From graph.

in the temperature determination. Each e.m.f. was measured with an accuracy of 0.6%, so that the average of the e.m.f. ratio should be accurate to about 0.5%. The other three uncertainties are 0.2%, 0.6%, and 0.5% respectively, giving an over-all uncertainty of about 1.5% for the results of each half of the sample, and about 1.0% for their average.

The uncertainty in the Lorentz function is the combination of the uncertainty in the resistivity and thermal conductivity, about 3%.

2.3. Thermoelectric Power of Armco Iron vs. Platinum

The e.m.f. between the platinum wires of the three thermocouples of each half of the sample were determined simultaneously with every measurement of temperature during the thermal conductivity experiment. These differential Pt–Fe–Pt measurements were used as checks of the internal consistency of the Pt/Pt–10% Rh thermocouples. Furthermore, by subtracting the e.m.f.'s taken with the central heater on and off, and dividing by the corresponding difference of the temperature differentials $\Delta T(z_1)$, the thermoelectric power of iron vs. platinum was calculated with an accuracy of 0.5%. The results obtained for the two outside thermocouples of each half of the sample are shown in Fig. 6, and their average value as read off the curve is given in Table IV. The interesting feature of these results is the change in slope at the

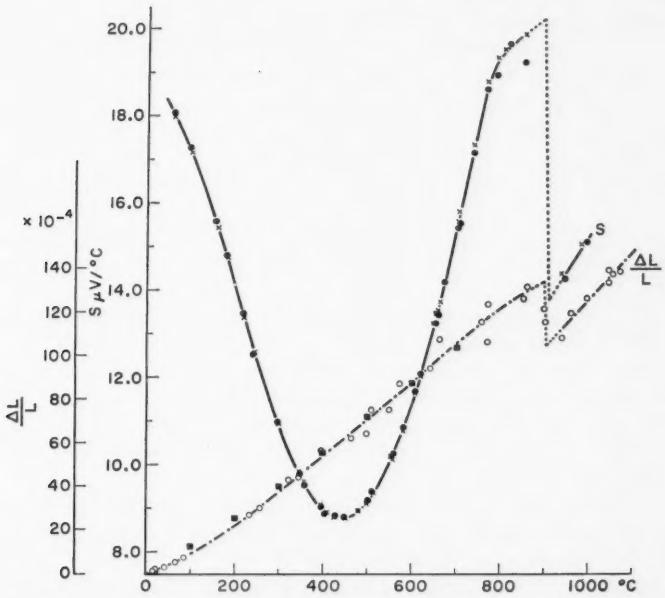

FIG. 6. The thermoelectric power vs. platinum and the thermal expansion of Armco iron: ●, × experimental points for the thermoelectric power vs. platinum, S, of the two halves of the sample; ○ experimental points of the total thermal expansion, $\Delta L/L$; ■ total thermal expansion calculated from data given in the Metals Handbook.

Curie point, and the 30% drop at the α–γ transition. There is no systematic difference between the results for the two halves of the sample, which is a good indication of the uniformity of the iron supplied for the test. The r.m.s. deviation of all the points from the curve drawn through them is 0.4%.

TABLE IV

Thermoelectric power vs. platinum and thermal expansion of Armco iron

T, °C	Thermoelectric power vs. platinum in μv/°C	Thermal expansion $\Delta L/L$	
		Laubitz	Metals Handbook
50	18.22	4×10^{-4}	—
100	17.12	9	12.1×10^{-4}
200	14.10	22	25.4
300	10.82	38	39.9
400	8.98	54	55.4
500	9.12	70	71.5
600	11.34	87	87.6
700	15.32	104	103.2
800	19.34	121	—
850	19.83	128	—
940	14.24	112	—
1000	15.20	125	—
1100	—	147	—

2.4. Thermal Expansion of Armco Iron

The thermal expansion measurements were made on a small piece of Armco iron, the expansion being measured relative to sintered alumina. The purpose of the measurement was to find the relative displacement of the sample thermocouples and the guard thermocouples in the thermal conductivity experiment. It was found, however, that on changing measurements from relative to absolute, using the values of Ebert and Tingwaldt (1936) for the expansion of alumina, very good agreement is obtained with values given by the Metals Handbook (1948) for iron in the temperature range of 0° C to 700° C. It was therefore decided to include the results of the expansion measurements in this report.

Figure 6 shows the experimental results for the total thermal expansion, $\Delta L/L$, and Table IV gives the average values as read off the curve. As could be expected, there is a sudden drop in the expansion at the α–γ transition, but the observed decrease is slightly larger than calculated from crystallographic data. The observed change in lattice parameters implies a density change of 0.4%, while the change in expansion observed here corresponds to a density change of 0.7%.

The accuracy of the expansion measurements is low; judging from the scatter of the experimental points, which represent four independent runs, the probable error in the expansion, $\Delta L/L$, is about 10%.

The values given in Table IV can be used to correct the thermal conductivity and electrical resistivity for the effect of thermal expansion of iron. The correction factor is simply $(1+\Delta L/L)$ for the electrical resistivity, and $(1-\Delta L/L)$ for the thermal conductivity.

3. DISCUSSION OF RESULTS

The results of the thermal conductivity measurements reported here are in very good agreement with those of Powell, in the range from room temperature to the Curie point. This close agreement is shown not by the thermal conductivity itself, but by the correspondence of the Lorentz functions (Fig. 5). One expects that differences in the iron of the samples will affect the Lorentz

function much less than either the thermal or electrical conductivity, as long as it is the electrons that are mainly responsible for the heat transfer. The comparison of the Lorentz function implies therefore that about 3/5 of the 5% discrepancy in the thermal conductivity at room temperature is due to basic differences in the constitution of the sample, presumably to the 0.09% difference in their purity. The remaining discrepancy, 2% at room temperature, is presumably due to experimental error, although part of it may be due to a further effect of the impurities in their scattering of the phonons. As can be expected, the effect of the impurities decreases with temperature, and the two thermal conductivity curves gradually approach each other, meeting at the Curie point.

Comparison with other results is not as satisfactory. There is little that can be said about the results of Hattori except that his experimental error is probably much larger than his estimate of it. Powell (1936) has already shown that Hattori's method of temperature measurement seriously affected the heat flow, which in any case was probably far from the rectilinear flow he assumed in the calculations. Maurer's results were obtained using a method open to the same criticism as Hattori's, and the good agreement with Powell's results at lower temperatures is probably fortuitous. The only serious difficulty is presented by the results of Armstrong and Dauphinee. They have performed what appears to be a very good experiment, and yet they obtained the highest conductivity for a sample of least purity. The difference between their and our results is 7% at room temperature, where the combined estimated error is only 4%.

At temperatures above the Curie point the results of the various observers spread so much that it is impossible to arrive at any correlation. Our results differ from previous ones not only in absolute value, but also in the shape of the temperature dependence curve. This is seen on an enlarged scale in Fig. 7,

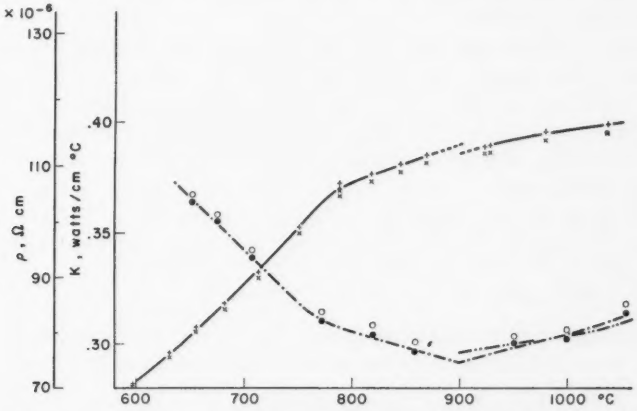

FIG. 7. Thermal conductivity and electrical resistivity of Armco iron in the vicinity of the Curie point (768° C) and the α–γ transition (900° C–910° C). ×, ○ Experimental points for the electrical resistivity and thermal conductivity respectively, uncorrected for thermal expansion; +, ● the same points corrected for the thermal expansion.

where the thermal conductivity and the electrical resistivity are shown after correction for the thermal expansion of iron. It is seen that the experimental points for the electrical resistivity definitely imply a discontinuous jump of about 1.8% at the α–γ transition. Such a jump is not surprising considering that other properties, such as thermoelectric power, thermal expansion, and specific heat, also show discontinuities at the transition. It is also not inconsistent with Powell's results, which display a peculiar little wiggle in that temperature region. Other observers have also reported unusual behavior in the electrical resistivity at the α–γ transition (see, for instance, Wallace, Sidles, and Danielson (1960)), but nothing as definite as our results. Any discontinuity in the electrical resistivity should have a corresponding discontinuity in the thermal conductivity, as in that temperature region about 85% of the heat is carried by electrons. In fact, as shown in Fig. 7, a discontinuous curve can be drawn through the experimental points for the thermal conductivity with a slightly better fit than obtained with a continuous curve. The discontinuity of about 1.7% is of the right order of magnitude.

4. SUMMARY

Thermal conductivity, electrical resistivity, and thermoelectric power vs. platinum were measured for a single piece of Armco iron in the temperature range of 0° C to 1000° C. The thermal conductivity was measured by a new unmatched guard method with an estimated uncertainty of 2.5%, and is in very good agreement up to 800° C with results obtained by Powell. All the properties, including thermal expansion measured on a different piece of Armco iron, indicate a greater or lesser discontinuous change at the α–γ transition in iron, and a change in slope at the Curie point.

APPENDIX

Mathematical Description of the Unmatched Guard Method of Measuring Thermal Conductivity

Figure 8 represents schematically each half of the sample, together with the powder between the guard and sample. K_1 and K_2 are the thermal conductivities of the sample and powder, assumed constant and uniform, a is the radius of the sample, b the inner radius of the guard, and L the length of each half of the sample. The assumed boundary conditions are:

(1) radial symmetry,

(2) $T(r,L) = T(L)$, a constant,

(3) $T(b,z) = f(z)+T(L)$, where $f(z)$ is an arbitrary function,

(4) $(\partial T/\partial z)_{z=0} = 0$.

The last condition imposes a restriction on $f(z)$.

Under these conditions, the solution of Laplace's equation is

$$T = \sum_n C_n I_0(\alpha_n r) \cos(\alpha_n z) + T(L) \qquad \text{in region 1}$$

$$T = \sum_n [A_n I_0(\alpha_n r) + B_n K_0(\alpha_n r)] \cdot \cos(\alpha_n z) + T(L) \qquad \text{in region 2}$$

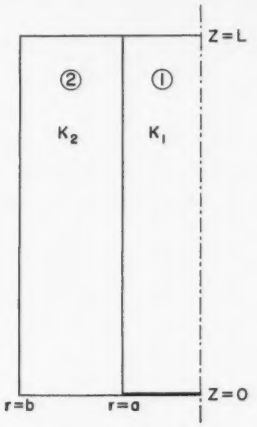

FIG. 8. Schematic representation of half of the guard-sample system.

where

$$\alpha_n = (n+\tfrac{1}{2})\,\pi/L,$$

$$C_n = A_n \frac{I_0(\alpha_n a)K_1(\alpha_n a)+I_1(\alpha_n a)K_0(\alpha_n a)}{I_0(\alpha_n a)K_1(\alpha_n a)+\rho I_1(\alpha_n a)K_0(\alpha_n a)},$$

$$B_n = A_n \frac{(-1)(\rho-1)I_0(\alpha_n a)I_1(\alpha_n a)}{I_0(\alpha_n a)K_1(\alpha_n a)+\rho I_1(\alpha_n a)K_0(\alpha_n a)},$$

$$\rho = K_1/K_2,$$

and

$$A_n I_0(\alpha_n b)+B_n K_0(\alpha_n b) = \frac{2}{L}\int_0^L T(b,z)\cos(\alpha_n z)\,dz.$$

I and K are the associated Bessel functions.

We assume that a wafer-thin central heater is located at $z = 0$ and extending to $r = a$, which, when switched on, establishes in the sample a uniform temperature gradient $(-G)$ for $z \to 0$ (due to the symmetry, that gradient is zero for $z = 0$). We further assume that the switching on of the central heater does not affect $f(z)$, but may change $T(L)$ to $T(L)+\Delta T(L)$. If we define $\Delta T(z)$ by

$$\Delta T(z) = T^G(a,z)-T^0(a,z)$$

where the superscripts G and 0 refer to temperatures with the central heater on and off, then

$$\text{(A.1)}\quad \Delta T(z) = GL(1-z/L)+\Delta T(L)+\sum_n (C_n{}^G-C_n{}^0)I_0(\alpha_n a)\cos(\alpha_n z)$$

$$= GL(1-z/L)+\Delta T(L)-GL\sum_n \beta_n(\rho)\cos(\alpha_n z)$$

where

$$\beta_n(\rho) = \frac{I_0(\alpha_n a)[I_0(\alpha_n a)K_1(\alpha_n a)+I_1(\alpha_n a)K_0(\alpha_n a)]}{\pi^2(n+\frac{1}{2})^2[I_0(\alpha_n b)I_0(\alpha_n a)K_1(\alpha_n a)+\rho I_1(\alpha_n a)I_0(\alpha_n b)K_0(\alpha_n a)} \cdots$$

$$\cdots \frac{}{-(\rho-1)I_0(\alpha_n a)I_1(\alpha_n a)K_0(\alpha_n b)]}.$$

Figure 9 shows the β_n as functions of $\rho = K_1/K_2$ for the geometry used in the experiment. K_2 has been measured in air, where it is approximately

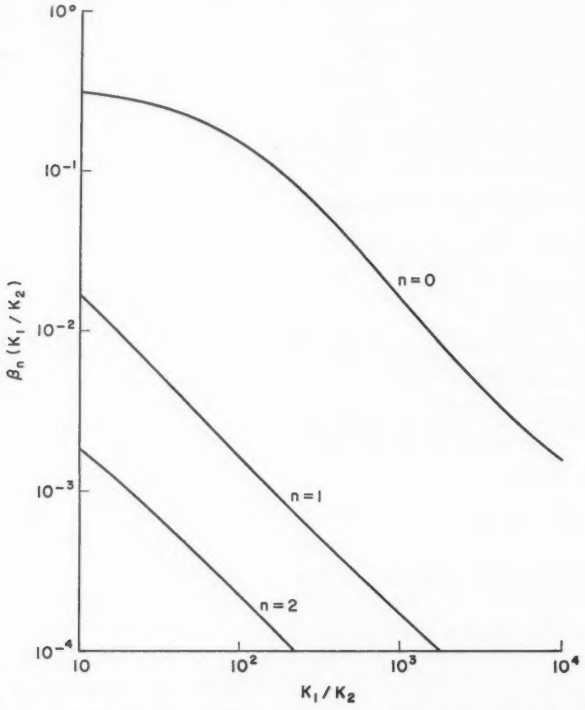

FIG. 9. Theoretical values of the parameters β_n as a function of K_1/K_2, for the geometry used in the experiment.

2 mw/°C cm. In vacuum K_2 is expected to be less than that, and therefore $K_1/K_2 \sim 10^2$ to 10^3. In that range of K_1/K_2 terms with $n > 1$ can be ignored in the infinite series in equation A.1.

G, of course, is the true temperature gradient established in the sample by that fraction of the heat input which flows along that sample. If only the total input into the central heater, $\dot{Q}$, is measured, then

$$\dot{Q} = K_1 A\ (G_t + G_b) \tag{A.2}$$

where $A = \pi a^2$ and the subscripts t and b refer to the top and bottom half of the sample.

It may be mentioned here that condition (4) $(\partial T/\partial z)_{z=0} = 0$ is unnecessarily rigid. It is sufficient to assume $(\partial T/\partial z)_{z=0} = g$, a constant, which may change to $g + \Delta g$ when the central heater is switched on. Equation A.1 then becomes

$$\Delta T(z) = G'L(1-z/L)+\Delta T(L)-G'L \sum_n \beta_n(\rho) \cos(\alpha_n z)$$

where $G' = G + \Delta g$ for one half of the sample and $G' = G-\Delta g$ for the other half. Equation A.2 therefore remains unchanged as

$$G'_t + G'_b = G_t + G_b.$$

REFERENCES

ARMSTRONG, L. D. and DAUPHINEE, T. M. 1947. Can. J. Research, A, **25**, 357.
EBERT, H. and TINGWALD, C. 1936. Physik. Z. **37**, 471.
HATTORI, D. 1937. Sci. Repts. Tôhoku Univ. **26**, 190.
LUCKS, C. F. and DEEM, H. W. 1958. ASTM Special Publ. No. 227, p.7.
MAURER, E. 1936. Arch. Eisenhüttenw, **10**, 1945.
METALS HANDBOOK. 1948. (American Society of Metals), p. 427.
POWELL, R. W. 1934. Proc. Phys. Soc. **46**, 659.
——— 1939. Proc. Phys. Soc. **51**, 407.
WALLACE, D. C., SIDLES, P. H., and DANIELSON, G. C. 1960. J. Appl. Phys. **31**, 168.

THE MAGNETIC SUSCEPTIBILITIES OF SOME DIAMAGNETIC ALLOYS

THE PRIMARY SOLID SOLUTIONS OF CADMIUM, INDIUM, TIN, AND ANTIMONY IN COPPER AND IN SILVER; ZINC, GALLIUM, GERMANIUM, AND ARSENIC IN SILVER; COPPER IN SILVER AND SILVER IN COPPER[1]

W. G. Henry and J. L. Rogers[2]

ABSTRACT

The results of the measurements of the variation with concentration of the magnetic susceptibility in the solid solutions of the following systems are presented: copper with silver, cadmium, indium, tin, and antimony as solutes; silver with copper, zinc, gallium, germanium, arsenic, cadmium, indium, tin, and antimony as solutes. The density of states for silver is calculated by using the approximation to nearly free electrons. It is found that the density of states is decreasing at an electron to atom ratio of 1.0. It is further found that the method used in an earlier paper to discuss the magnetic properties of the α-solid solutions formed with copper by zinc, gallium, germanium, and arsenic is applicable to the monovalent–polyvalent systems of the present paper. It is concluded from the magnetic measurements that the Fermi surface touches the (111) Brillouin zone face in both silver and copper and that the rate of decrease of the density of states with electron to atom ratio is given approximately by the approximation to nearly free electrons. The solid solutions in the silver–copper system are anomalous.

1. INTRODUCTION

The results of the measurements of the variation of the diamagnetic susceptibilities with concentration in the solid solutions formed with copper as solvent by the four metals following it in the periodic table were presented in an earlier paper (Henry and Rogers 1956*b*). This paper will be referred to hereinafter as II. It was found that the rate at which the alloys become diamagnetic increases with the valency of the solute. The increase in diamagnetism was ascribed to two major sources: (1) the diamagnetism of the solute ion and its localized Z electrons, where Z is the difference in valency between the solute and the solvent; (2) the decrease in the net paramagnetic susceptibility of the conduction electrons which results from a decrease in the density of states at the Fermi surface with increasing electron density (Jones 1937).

It was thought desirable to investigate: (1) the influence of the same series of solutes from the IVth period in another monovalent solvent, to determine whether or not the change in susceptibility did depend in part upon the solvent; (2) the influence of the solutes from the Vth period with the corresponding valency, to determine whether or not the apparent valency effects existed there as well.

[1]Manuscript received in original form November 24, 1959, and, as revised, April 1, 1960.
Contribution from the Division of Applied Chemistry, National Research Council, Ottawa, Canada.
Issued as N.R.C. No. 5717.
[2]Present address: Space Technology Laboratories, Los Angeles, California.

The measurements appear to indicate that the contribution of the polyvalent solute ion to the magnetic susceptibility of the alloy is fairly independent of the solvent and that there is an additional contribution which is proportional to the electron to atom ratio, with the constant of proportionality depending upon the solvent and being independent of the solute.

In order to make a quantitative calculation of the observed initial slope of the magnetic susceptibility, concentration curves, by the method suggested in II, it was necessary to calculate the density of states for silver by the method suggested by Jones (1937). The results of this calculation are presented in Section 4.

2. PREPARATION OF ALLOYS

The approximate purity, iron content in atomic parts per million, and the source of supply of the metals used in the preparation of the alloys are:

1. Copper, greater than 99.999%, 0.2 p.p.m., purchased from the American Smelting and Refining Co.
2. Zinc, 99.999%, less than 1.0 p.p.m., donated by the Consolidated Mining and Smelting Co.
3. Gallium, 99.99%, 2.0 p.p.m., purchased from the Eagle-Picher Co.
4. Germanium, 99.99%, 1.0 p.p.m., purchased from the Eagle-Picher Co.
5. Arsenic, 99.95%, less than 1.0 p.p.m. iron, 0.05 wt. % antimony, distilled by Dr. R. D. Heyding.
6. Cadmium, 99.99%, less than 1.0 p.p.m., donated by the Consolidated Mining and Smelting Co.
7. Indium, 99.99%, 1.0 p.p.m., donated by the Consolidated Mining and Smelting Co.
8. Tin, 99.99%, 1.5 p.p.m., purchased from Johnson Matthey and Co. Ltd.
9. Antimony, 99.99%, 5.0 p.p.m., purchased from A. D. Mackay, Inc.
10. Silver, 99.999%, 1.0 p.p.m., electrolytically refined (Henry and Rogers 1956*a*).

The latter paper will be referred to hereinafter as I. The iron analysis only has been made in this laboratory.

Although some of the alloys were prepared as described in paper II, about half were melted and chill-cast in an apparatus which has been described elsewhere (Craw and Henry 1956). The alloys prepared in this apparatus were superior to the earlier ones in that both lateral and vertical segregation were considerably reduced. Quartz crucibles were used in all cases for melting in this latter apparatus except for those alloys which contained gallium and indium; in these cases either purified graphite or alumina crucibles were employed. The alloys were cast in an atmosphere of purified argon. After a heat treatment, a specimen 7.5×20 mm was machined from the ingot. The specimens were acid-cleaned before measuring to remove iron contamination as a result of machining.

The alloys were heat-treated to remove local inhomogeneities in the concentration and to ensure a single phase, face-centered cubic, solid solution. The details of the heat treatment were varied according to the requirements of

the alloy system. A brief description of the relevant portions of the phase diagrams and the heat treatments is as follows.

Silver–Cadmium, –Indium, –Tin, and –Antimony

For these four systems the $\alpha/\alpha+\beta$ boundaries as determined by Owen and Roberts (1939) and by Hume-Rothery, Mabbott, and Evans (1934) are in good agreement. The limits of the α-solid solutions are: silver–cadmium, 39.9 at.% at 600° C, 42.6 at.% at 300° C; silver–indium, 19.5 at.% at 600° C, 19.1 at.% at 300° C; silver–tin, 10.9 at.% at 600° C, 9.8 at.% at 300° C; silver–antimony, 6.8_5 at.% at 600° C, 5.6 at .% at 300° C.

The alloys in these systems were annealed at 550° C, in a purified argon atmosphere in pyrex containers, for 10 days and then air-cooled prior to machining.

Copper–Silver, –Cadmium, –Indium, –Tin, and –Antimony

The limits of the α-solid solutions in these systems are: copper–silver (Chaston 1953), 4.8 at.% at 779° C, 0.0_5 at.% at 200° C; copper–cadmium (Owen and Pickup 1933), 1.7 at.% at 549° C, 0.28 at.% at 300° C; copper–indium (Owen and Roberts 1953), 10.9 at.% at 575° C, 6.8 at.% at 470° C; copper–tin (Raynor 1944), 15.8 at.% at 550° C, 1.2 at.% at 200° C; copper–antimony (Hume-Rothery, Mabbott, and Evans 1934), 5.6 at.% at 600° C, 2.8 at.% at 200° C.

The alloys in these systems were heat-treated prior to machining as follows: copper–silver, 3 weeks at 600° C then quenched in iced water followed by 24 hours at 850° C and then quenched in iced salt water; copper–cadmium, 10 days at 550° C and then quenched in a rapid quenching furnace of special design (Owen 1944); copper–indium, 2 weeks at 550° C and then quenched in iced water; copper–tin, 3 weeks at 550° C and then quenched in iced water; copper–antimony, 2 weeks at 575° C and quenched in the rapid quenching furnace. In all cases the annealing was carried out in pyrex containers in a purified argon atmosphere except for the high temperature annealing and quenching of the copper–silver alloys for which quartz containers were used.

Silver–Copper, –Zinc, –Gallium, –Germanium, and –Arsenic

The limits of the α-solid solutions in the systems are: silver–copper (Chaston 1953), 14.0 at.% at 779° C, 0.42 at.% at 200° C; silver–zinc (Owen and Edmunds 1938), 33.6 at.% at 680° C, 39.7 at.% at 331° C; silver–gallium (Owen and Rowlands 1940), 17.8 at.% at 615° C, 14.9 at.% at 300° C which are lower than the results of Hume-Rothery, Mabbott, and Evans (1934); silver–germanium (Owen and Rowlands 1940), 7.9_2 at.% at 575° C, 1.5 at.% at 270° C; silver–arsenic (Owen and Rowlands 1940), 8.5_5 at.% at 545° C, 4.2_3 at.% at 296° C.

The alloys in these systems were heat-treated prior to machining as follows: silver–copper, 3 weeks at 600° C then quenched in iced water followed by 24 hours at 800° C and then quenched in iced salt water; silver–zinc, 10 days at 600° C and then air-cooled; silver–gallium, 10 days at 600° C and then air-cooled; silver–germanium, 10 days at 600° C and then quenched in the rapid quenching furnace; silver–arsenic, 10 days at 600° C and then quenched

in the rapid quenching furnace. The silver–copper alloy measured at 717° C was given the same heat treatment as the ones measured at room temperature. In addition it was maintained at 717° C for 2 hours prior to measurement. No change occurred in the susceptibility during the measurement.

The alloys of highest concentration in the following systems were examined micrographically for the presence of β phase: silver–copper, silver–germanium, silver–arsenic, copper–silver, and copper–cadmium. No β phase was found.

The analysis of the silver–cadmium, –indium, –tin, and –antimony alloys was carried out by measuring the difference between the lattice parameter of pure silver and that of the alloy and by making a comparison with the results of Owen and Roberts (1939). The same method was applied to the silver–zinc system using the results of Owen and Edmunds (1938). All other alloys were chemically analyzed. In all cases a sample was taken from as near as possible to both the top and the bottom of the specimen. The error recorded with the analysis is the probable error in the mean value of the composition as determined from the two ends of the specimen. It is a measure of homogeneity rather than an indication of the error in the analysis. The estimated error in all the analyses is $\pm 0.05\%$.

3. MAGNETIC SUSCEPTIBILITY MEASUREMENT

The apparatus, the method of measurement, the errors in susceptibility, and the method of correcting for ferromagnetic iron were discussed in earlier papers I and II. All the measurements were made at room temperature, $23 \pm 2°$ C except for two at 717° C; a pure silver specimen and a silver–copper alloy containing 6.21 ± 0.07 at.%. The apparatus used for these measurements will be described in a later paper.

One atomic part per million of iron in solution in copper changes the susceptibility by about 0.1% (paper I). In view of the purity of the copper, the error from this source is of the order of the experimental error and no correction was applied to the copper alloys. The solubility of iron in solid silver is reported to be approximately 5.0 p.p.m. (Tammann and Oelsen 1930). It was not possible therefore to determine the influence of iron in solution in silver on the susceptibility of silver. If it is assumed that it is of the same order of magnitude as in copper then, in view of the purity of the materials, the error from this source may be neglected. Another difficulty arose, however, in connection with the silver alloys, presumably associated with the low solubility of iron in silver. There was a tendency for the silver alloys to have larger differences between χ_{10} and χ_{∞} where χ_{10} and χ_{∞} are the susceptibility at maximum field and the extrapolated susceptibility respectively. Some points for which this difference was greater than 5.0% of χ_{10} fell off the curve, outside the limits of experimental error, and were discarded. There were no points, however, for which the difference was less than 5.0% which did not fall on the curves. Only those points for which the difference was 5.0% or less have been reported.

The results of the measurements for the 14 solid solutions are shown in Tables I, II, and III, and Figs. 1, 2, and 3.

TABLE I

Magnetic susceptibility of solid solutions; silver with solutes from the Vth period

Alloy (silver)	Mean composition (at.%)	Mean $\chi_{10}\times10^6$ (c.g.s. e.m.u. per gram)	Mean $\chi_\infty\times10^6$ (c.g.s. e.m.u. per gram)	Mean $\chi_A\times10^6$ (c.g.s. e.m.u. per gram atom)
		Silver–cadmium system		
				-19.55_6
1	1.17±0.07	−0.1809	−0.1825	−19.70
2	1.24±0.01	−0.1787	−0.1812	−19.56
3	3.88±0.04	−0.1824	−0.1838	−19.86
4	4.09±0.01	−0.1825	−0.1840	−19.89
5	6.34±0.09	−0.1854	−0.1857	−20.09
6	6.88±0.00	−0.1858	−0.1863	−20.15
7	7.60±0.23	−0.1863	−0.1862	−20.16
8	12.60±0.09	−0.1920	−0.1924	−20.86
9	19.20±0.07	−0.2012	−0.2020	−21.89
10	26.26±0.11	−0.2074	−0.2115	−23.07
11	30.40±0.08	−0.2236	−0.2239	−24.47
12	37.38±0.08	−0.2402	−0.2407	−26.38
		Silver–indium system		
1	1.00±0.02	−0.1820	−0.1834	−19.80
2	3.08±0.07	−0.1893	−0.1906	−20.60
3	6.04±0.04	−0.1962	−0.1966	−21.29
4	8.62±0.14	−0.2042	−0.2051	−22.25
5	10.56±0.12	−0.2085	−0.2091	−22.71
6	14.01±0.17	−0.2190	−0.2191	−23.85
7	17.06±0.04	−0.2272	−0.2281	−24.88
		Silver–tin system		
1	1.14±0.03	−0.1868	−0.1874	−20.24
2	2.38±0.02	−0.1906	−0.1933	−20.91
3	2.42±0.01	−0.1940	−0.1954	−21.14
4	3.52±0.03	−0.1971	−0.1982	−21.46
5	4.94±0.05	−0.2042	−0.2045	−22.17
6	5.82±0.07	−0.2078	−0.2085	−22.62
7	7.30±0.11	−0.2139	−0.2153	−23.39
		Silver–antimony system		
1	1.05±0.01	−0.1853	−0.1886	−20.38
2	3.00±0.01	−0.1984	−0.2029	−21.97
3	3.46±0.00	−0.1946	−0.2053	−22.24

The initial slopes of the susceptibility, concentration curves were determined by fitting either a straight line or a parabola, by the method of averages, to the data (Table IV).

The increase in the rate of change of the susceptibility with increasing valency is apparent in Figs. 1, 2, and 3 in the three series Ag(V), Cu(V), and Ag(IV). The Roman numerals in parentheses indicate the period of the solute. In this respect the behavior of these three series is the same as that found for the Cu(IV) series in paper II. A more detailed discussion of the results is given in Section 5.

Other measurements of the magnetic susceptibility of the same solid solutions

TABLE II

Magnetic susceptibility of solid solutions; copper with solutes from the Vth period

Alloy (copper)	Mean composition (at.%)	Mean $\chi_{10}\times10^6$ (c.g.s. e.m.u. per gram)	Mean $\chi_\infty\times10^6$ (c.g.s. e.m.u. per gram)	Mean $\chi_A\times10^6$ (c.g.s. e.m.u. per gram atom)
		Copper–silver system		-5.46_7
1	1.16±0.10	−0.0872	−0.0878	−5.63
2	1.49±0.00	−0.0879	−0.0880	−5.65
3	2.92±0.01	−0.0906	−0.0911	−5.91
		Copper–cadmium system		
1	0.47±0.01	−0.0844	−0.0864	−5.51
2	0.61±0.02	−0.0874	−0.0875	−5.59
3	0.86±0.01	−0.0873	−0.0877	−5.61
		Copper–indium system		
1	1.97±0.01	−0.0933	−0.0934	−6.03
2	2.25±0.01	−0.0939	−0.0945	−6.12
3	3.66±0.12	−0.1014	−0.1018	−6.66
		Copper–tin system		
1	1.00±0.00	−0.0919	−0.0920	−5.90
2	1.94±0.01	−0.0972	−0.0975	−6.30
3	2.60±0.02	−0.1012	−0.1013	−6.58
4	5.15±0.02	−0.1144	−0.1147	−7.62
		Copper–antimony system		
1	0.90±0.00	−0.0929	−0.0929	−5.95
2	1.84±0.07	−0.0996	−0.0997	−6.45
3	2.78±0.02	−0.1065	−0.1067	−6.96

are as follows. Childs and Penfold (1957) measured one alloy in the silver–cadmium system containing 30.5 at.% cadmium. A correction for ferromagnetic impurity was made by extrapolating against $1/H$. Their value for pure silver and for the one alloy are included in Fig. 1. Stephens and Evans (1936) measured one alloy in the solid solution region of the silver–antimony system containing 2.7_6 at.% antimony. It is not stated that these measurements were corrected for ferromagnetic impurity. Their value for pure silver and for the one alloy are included in Fig. 1. Endo (1925) measured one alloy in the solid solution region of the copper–tin system containing 2.5_5 at.% tin. It is not stated that a correction was applied for ferromagnetic impurities. The value for pure copper and for the one alloy are included in Fig. 2. In all cases the slopes agree roughly with those found in the present work. The differences in the absolute values are presumably due to differences in calibration and in some cases to differences in the purity of materials. Meyer and Weiner (1957) measured the temperature dependence of several alloys in the solid solution region of the silver–zinc system. Comparison was not meant to be made among the alloys and thus their results have not been included.

TABLE III

Magnetic susceptibility of solid solutions; silver with solutes from the IVth period

Alloy (silver)	Mean composition (at.%)	Mean $\chi_{10}\times10^{-6}$ (c.g.s. e.m.u. per gram)	Mean $\chi_{\infty}\times10^{-6}$ (c.g.s. e.m.u. per gram)	Mean $\chi_A\times10^{-6}$ (c.g.s. e.m.u. per gram atom)
		Silver–copper system		-19.55_6
1	3.02±0.00	−0.1778	−0.1789	−19.06
2	6.16±0.02	−0.1766	−0.1778	−18.70
		Silver–copper 717° C		
				−19.32
3	6.21±0.07			−18.37
		Silver–zinc system		
1	2.10±0.05	−0.1821	−0.1822	−19.50
2	4.60±0.00	−0.1825	−0.1831	−19.39
3	4.69±0.13	−0.1750	−0.1829	−19.36
		Silver–gallium system		
1	1.06±0.02	−0.1818	−0.1838	−19.75
2	2.46±0.00	−0.1873	−0.1879	−20.10
3	4.78±0.05	−0.1809	−0.1923	−20.40
4	4.91±0.01	−0.1922	−0.1932	−20.48
5	5.06±0.00	−0.1919	−0.1925	−20.39
6	9.85±0.03	−0.2013	−0.2023	−21.07
		Silver–germanium system		
1	0.73±0.00	−0.1846	−0.1859	−20.01
2	0.78±0.00	−0.1824	−0.1836	−19.78
3	0.99±0.00	−0.1864	−0.1872	−20.13
4	1.88±0.03	−0.1850	−0.1917	−20.55
5	2.38±0.02	−0.1890	−0.1929	−20.65
6	4.98±0.01	−0.2023	−0.2027	−21.51
		Silver–arsenic system		
1	0.50±0.02	−0.1849	−0.1857	−20.00
2	1.49±0.00	−0.1923	−0.1937	−20.80
3	3.11±0.00	−0.2039	−0.2043	−21.83
4	5.26±0.01	−0.2126	−0.2127	−22.58

TABLE IV

Calculated and observed slopes

Solute	Slope in Cu	Slope in Ag	Experimental difference	Calculated difference	
	c.g.s. e.m.u. per gram atom per mole$\times10^6$				
Cu		15.7	−16		
Zn	− 7.2	3.5	−11	− 9	
Ga	−18.8	−21.7	3	7	
Ge	−26.7	−50.0	23	22	
As	−35.8	−81.8	46	42	
Ag	−14.2		−14		
Cd	−20.3	− 6.2	−14	−11	(−14)*
In	−30.6	−30.8	0	8	(2)
Sn	−42.4	−54.9	13	22	(13)
Sb	−55.0	−80.9	26	39	(25)

*Numbers in parentheses obtained by using $Z\times14\times10^{-6}$ instead of $Z\times17\times10^{-6}$.

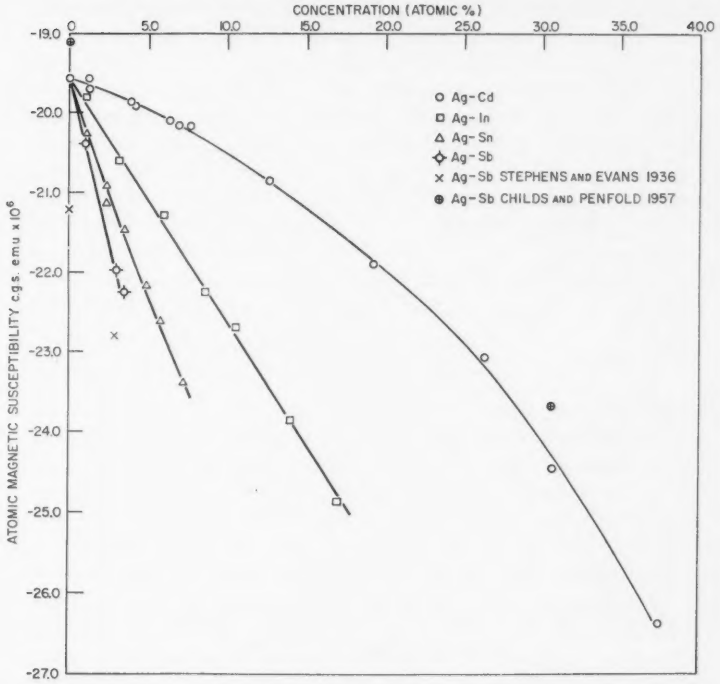

FIG. 1. Magnetic susceptibility of solid solutions; silver with solutes from the Vth period.

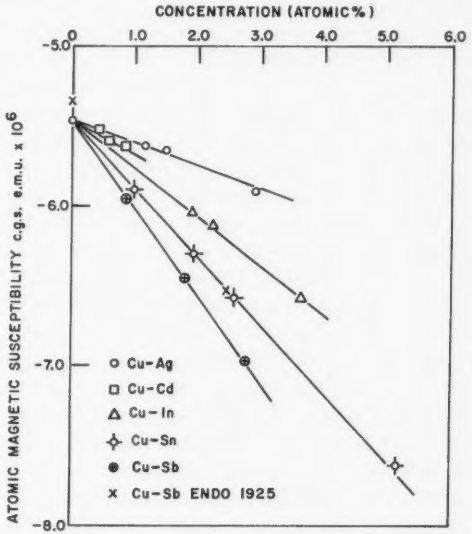

FIG. 2. Magnetic susceptibility of solid solutions; copper with solutes from the Vth period.

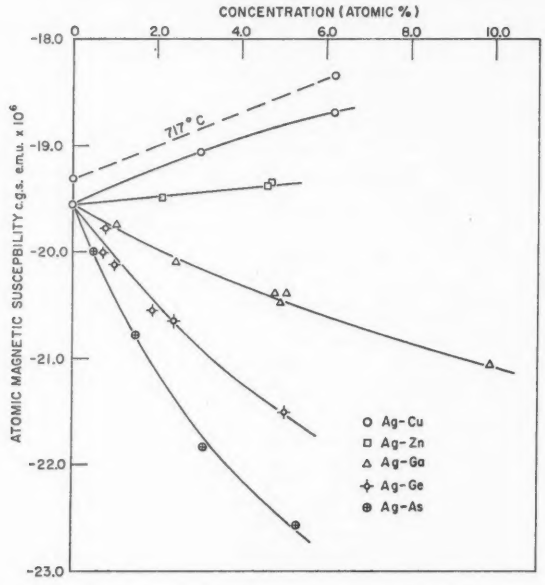

FIG. 3. Magnetic susceptibility of solid solutions; silver with solutes from the IVth period.

4. DENSITY OF STATES FOR SILVER

Jones (1937) calculated the density of states for copper by a method based on the approximation to nearly free electrons. As a result of the hyperbolic form of the surfaces of constant energy in the region of the (III) zone face, the peak in the density of states function occurs at an electron to atom ratio, e/a, of approximately 1.0. Thus, when the electron to atom ratio increases, as it is assumed to do upon the addition of a polyvalent solute, the density of states should decrease. In attempting to explain the magnetic properties of the solid solutions of the IVth period solutes in copper (paper II), the possibility of a decreasing density of states was found convenient.

Slater (1936) calculated the density of states for copper using the data of Krutter (1935) which was obtained by using the cellular method. At an electron to atom ratio of 1.0 the density of states is still rising. Howarth (1953, 1955) when comparing the results of the calculations of the eigenvalues and eigenfunctions of copper as calculated by the cellular method and the method of augmented plane waves, emphasizes the sensitive nature of the dependence of ΔE, the energy gap across the (III) face, on the choice of the potential. Further, ΔE depends markedly on the method employed. Howarth, when using the cellular method obtained an energy gap of 0.24 ev and when using the method of augmented plane waves obtained an energy gap of approximately 2.0 ev. It is reasonable to conclude therefore that the accuracy with which ΔE may be calculated by these methods is not great.

The position of the peak in the density of states obtained by Jones (1937) is at an energy $E_p = E_0 - \Delta E/2$, where E_0 is the energy of a free electron at the center of the zone face and ΔE is obtained from optical data. If the density of states were calculated by one of the more elegant methods, then it would appear that the accuracy with which the position of the peak might be determined would be directly related to the accuracy with which ΔE might be calculated. In view of the lack of agreement between the methods and the difficulty concerning the choice of potential, it was felt that it was worth while to calculate the density of states for silver using the method based on the approximation to nearly free electrons.

The energy gap for silver was determined by a method suggested by Jones (1934). To the accuracy given by the perturbation method,

$$\frac{\Delta E^{Ag}}{\Delta E^{Cu}} = \frac{(z-f_n)^{Ag} \cdot a^{Cu}}{(z-f_n)^{Cu} \cdot a^{Ag}} \tag{4.1}$$

where z is the atomic number and f_n is the atomic scattering power for X rays at $\sin \theta/\lambda = n/2a$; a^{Cu} and a^{Ag} are the lattice parameters of copper and silver respectively; n is the distance from the origin to the (111) zone face. The scattering powers may be obtained from tables (Peiser, Rooksby, and Wilson 1955). The value for ΔE for copper as chosen by Jones from the optical data is 4.1 ev. For silver ΔE is given by (4.1) to be 4.8 ev which agrees moderately well with an absorption edge in silver beginning at 4.0 ev (Mott and Jones 1936). The density of states calculation was carried out using a value of 4.8 ev. If the lower value were used the peak would be shifted 0.4 ev higher, but the form of the curve would not be appreciably altered.

The results of the calculation are shown in Figs. 4 and 5 with the corresponding results for copper obtained by Jones. It is to be noted that according to this approximation the energy on the Fermi surface ζ_0^{Ag} occurs well beyond the peak for silver where the density of states is decreasing. If the Fermi surface were spherical, the density of states would not decrease until $e/a = 1.36$ (Hume-Rothery 1947).

Since the explanation of the experimental results presented in this paper depends on the density of states decreasing with increasing electron to atom ratio in both silver and copper, it is appropriate to consider briefly some of the other experimental evidence bearing on this point. Rayne (1957, 1958) measured the electronic specific heat of copper–zinc and copper–germanium α-solid solutions. The results of his measurements indicate an initial rapid increase in the density of states with electron to atom ratio followed by a levelling off or even a slight decrease. Jones (1957), however, has shown that when the Fermi surface lies close to a zone boundary the electron–lattice interaction leads to a term linear with temperature. It is suggested that this factor is responsible for the apparent rapid rise in the electron specific heat of the α brasses. Childs and Penfold (1957) in criticizing the proposed explanation of the observed variation of the magnetic susceptibility with concentration in the copper solid solutions (paper II) cited specific heat data as an indication that the density of states is increasing at the Fermi surface. In order to explain

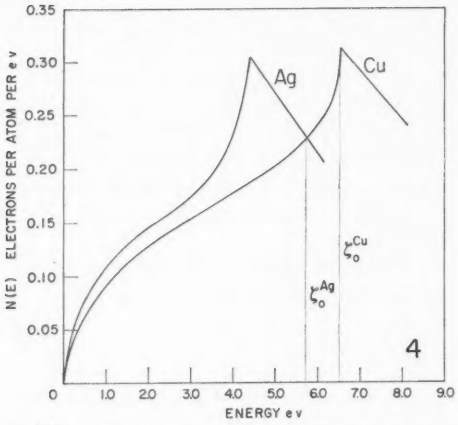

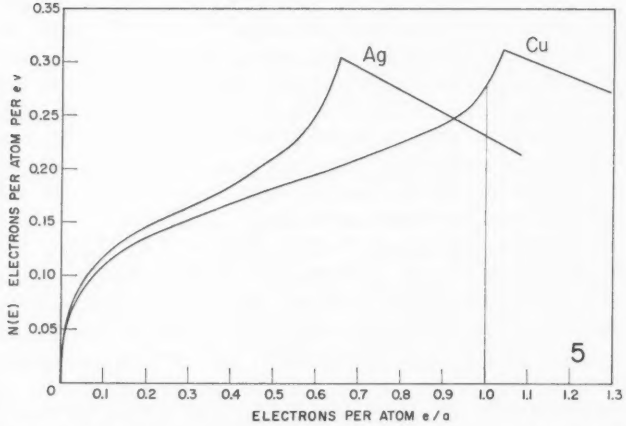

FIG. 4. Density of states for copper (Jones 1937) and silver as a function of energy.
FIG. 5. Density of states for copper and silver as a function of e/a.

the high Wiedeman–Franz ratio of copper, silver, and gold, Klemens (1954) suggested that the Fermi surface touches the zone boundary in all three metals. It is concluded from the work of Smit (1952) and Mortlock (1953), who investigated the influence of shear strain on the thermoelectric power of gold, and silver, and copper, respectively, that the Fermi surface touches the zone boundary in all three metals. On the other hand, Jones (1957) calculated an expression for the thermoelectric power of monovalent metals which, to be positive in agreement with experiment, requires that $N'(E)$ be large and positive, as it may be just before the Fermi surface touches the zone boundary. Recently Rowland (1958) has measured the Knight shift in the solid solutions formed by silver with the Vth period elements. A decrease in the Knight shift

is observed with increasing electron to atom ratio. This may be explained by either a decreasing density of states or an increase in the p-character of the wave functions at the Fermi surface. Cohen and Heine (1958) have recently surveyed the conflicting data on this subject. Their attempt to discredit the Jones (1937) model is, however, marred by a misunderstanding of the model.

5. DISCUSSION OF RESULTS

In paper II it was suggested that the atomic susceptibility of the alloys χ_A might be represented by

$$\chi_A = (1-x)\chi_{M^+} + \chi_{S^+} + \chi_F(x, a') \tag{5.1}$$

where x is the mole fraction; χ_{M^+} is the susceptibility of the solvent metal ion; χ_{S^+} is the susceptibility of the solute ion with a charge equal to its valency v plus the susceptibility of the Z localized electrons where $Z = v-1$. $\chi_F(x, a')$ is the net paramagnetic susceptibility of the conduction electrons, which is a function of the electron to atom ratio and the lattice parameter of the solid solution a'. It was assumed that

$$\chi_F(x, a') = [\beta N(E)_\zeta].\ a'^3/a^2 \tag{5.2}$$

where $N(E)_\zeta$ and a' are the density of states at the Fermi surface for a lattice with a lattice parameter a, and the lattice parameter of the alloy respectively. The constant β is given by

$$\beta = \chi_M^F(0)/N(E)_{\zeta_0} \tag{5.3}$$

where $\chi_M^F(0)$ is the net paramagnetic contribution of the conduction electrons in the pure solvent, which is equal to the difference between the susceptibility of the pure metal and its singly charged ion; $N(E)_{\zeta_0}$ is the density of states at the Fermi surface of the pure metal. Beyond the peak (see Figs. 4 and 5) the density of states varies approximately linearly with e/a. The density of states in this region is thus given by

$$N(E)_\zeta = N(E)_{\zeta_0} + N'(E)_{\zeta_0}\, x\, Z. \tag{5.4}$$

The initial slope of the susceptibility, concentration curve is thus given by

$$\frac{d\chi_A}{dx} = \chi_{S^+} - \chi_{M^+} + \chi_M^F(0)\left[2\xi + \left(\frac{N'(E)}{N(E)}\right)_{\zeta_0} Z\right] \tag{5.5}$$

where ξ is the proportional change in the lattice parameter for unit concentration (Owen 1947).

In order to apply the method of interpreting the results suggested in II, it is first necessary to decide on a value for χ_{Ag^+}. Since the self-consistent field with exchange for Ag^+ has not been done and since the approximate method of correcting for exchange used in II may be unreliable at this atomic number, alternative methods of arriving at a value are necessary. If $2\chi_M^F(0)\xi$, which turns out to be small, is neglected in (5.5), then both χ_{Ag^+} and $\chi_{Ag}^F(0)\{N'(E)/N(E)\}_{\zeta_0}$, may be calculated from the experimental slopes of the Ag(IV)

series. If it is assumed that χ_{S^+} is approximately independent of the solvent, then simultaneous equations may be set up of the form

$$(5.6) \qquad \begin{aligned} [d\chi_A/dx]_{expt} &= \chi_{Zn^+} - \chi_{Ag^+} + \gamma \\ [d\chi_A/dx]_{expt} &= \chi_{Ga^+} - \chi_{Ag^+} + 2\gamma \end{aligned}$$

where $[d\chi_A/dx]_{expt}$ is the experimentally determined slope; $\gamma = \chi^F_{Ag}(0)\{N'(E)/N(E)\}_{\zeta_0}$ and χ_{Zn^+} and χ_{Ga^+} are the susceptibilities of the singly charged Zn^+ and Ga^+ solute ions which were calculated in II. There are six sets of equations of this type. The results of the six determinations and the probable errors of χ_{Ag^+} and γ are $-50.5\pm2.3\times10^{-6}$ and $-25.6\pm0.7\times10^{-6}$ respectively. All susceptibilities are expressed in c.g.s. e.m.u. per mole.

Pauling (1927) calculated -44×10^{-6} for χ_{Ag^+} by a semi-empirical method. Pauling's empirical values agree within 10% with values calculated from self-consistent fields with exchange, where comparisons may be made. The diamagnetic susceptibility of the singly charged silver ion as calculated from the self-consistent field (Black 1935) is -61.8×10^{-6}. If this is corrected approximately for the effect of exchange by multiplying by 0.8 (II) then $\chi_{Ag^+} = -49.4\times10^{-6}$. These two theoretical values for χ_{Ag^+} are in reasonably good agreement with the experimental value. They do not agree, however, with the value of approximately -26×10^{-6} obtained from inorganic salts (Pacault 1946). Pauling's value for χ_{Ag^+} is used in the remainder of this discussion.

A comparison may be made at this point between the theoretical value and the experimental value of γ as determined from the Ag(IV) series. The ratio of the derivative of the density of states with respect to the electron to atom ratio, to the density of states at ζ_0^{Ag} is found from the results of Section 4 to be -0.91. $\chi^F_{Ag}(0)$ is equal to 24×10^{-6} ($\simeq -19.6\times10^{-6}+44\times10^{-6}$). Hence $\gamma = -22\times10^{-6}$ in apparent good agreement with the experimentally determined value. It must be admitted, however, that the degree of agreement may be to an undetermined extent fortuitous.

In order to demonstrate clearly the influence of the solvents, in Figs. 6 and 7 the sum of $[d\chi_A/dx]_{expt}$ and the theoretical value of χ_{M^+} (χ_{Ag^+}, -44×10^{-6}; χ_{Cu^+}, -14.7×10^{-6}) is plotted for each series of solutes in the two solvents. The results for the Cu(IV) systems have been taken from II. It is to be noted that the resulting curves fall into two series, the copper series and the silver series. On referring to (5.5), it is seen that the ordinate is the sum of the contribution of the solute ion and the rate of change of the contribution from the conduction electrons. If it is assumed that χ_{S^+} is approximately independent of the solvent, then the difference in the ordinates at a given valency must be due to the difference in the rate of change of the contribution of the conduction electrons in the two solvents.

Since the self-consistent fields for Cd^+, In^+, Sn^+, and Sb^+ have not been determined, the initial slopes of the susceptibility, concentration curves may not be calculated for the Cu(V) and Ag(V) series as was done for the Cu(IV) series in II. The difference in the slopes of the susceptibility, concentration curves for the same solute in the two solvents may, however, be calculated

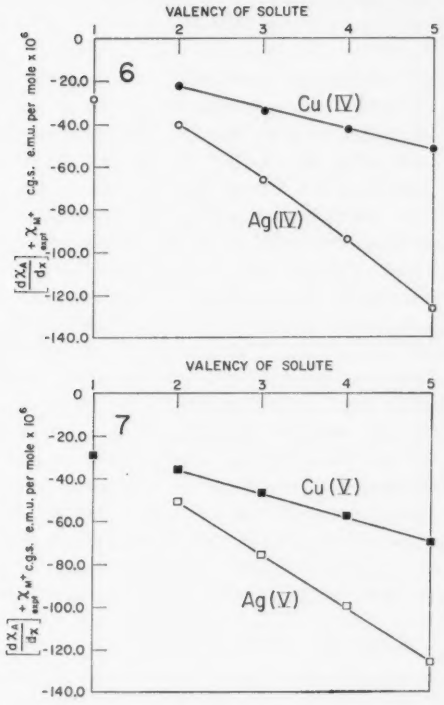

FIG. 6. Initial slopes of the susceptibility, concentration curves adjusted for the influence of the solvent ion.

FIG. 7. Initial slopes of the susceptibility, concentration curves adjusted for the influence of the solvent ion.

by using (5.5), subject to the assumption that χ_{S^+} is approximately independent of the solvent. The calculated difference for the four series will then be compared with the experimental difference and the degree of agreement used to determine the validity of the initial assumptions. The difference in slopes is given by

$$(5.7)\quad \left[\frac{d\chi_A}{dx}\right]_{Cu} - \left[\frac{d\chi_A}{dx}\right]_{Ag} = \chi_{Ag^+} - \chi_{Cu^+} + Z\left\{\chi^F_{Cu}(0)\left(\frac{N'(E)}{N(E)}\right)_{\xi_0{}^{Cu}} - \chi^F_{Ag}(0)\left(\frac{N'(E)}{N(E)}\right)_{\xi_0{}^{Ag}}\right\} + 2\chi^F_{Cu}(0)\xi^{Cu} - 2\chi^F_{Ag}(0)\xi^{Ag}.$$

In order to calculate the right-hand side of (5.7) the following data has been used: χ_{Ag^+}, -44×10^{-6} (Pauling 1927); χ_{Cu^+}, -14.7×10^{-6} (Hartree and Hartree 1936); $\chi^F_{Cu}(0)$, 9.3×10^{-6}; $\chi^F_{Ag}(0)$, 24×10^{-6}; $N'(E)_{\xi_0{}^{Cu}}$, -0.17 electron per atom per electron volt per electron to atom ratio; $N(E)_{\xi^{Cu}}$, 0.31

electron per atom per electron volt; $N'(E)_{\zeta_0^{Ag}}$, -0.21; $N(E)_{\zeta_0^{Ag}}$, 0.23 (Fig. 5). As in paper II it has been assumed that ζ_0^{Cu} is at or slightly beyond the peak in the density of states.

The observed and calculated differences in the initial slopes are shown in Table IV. The sum of the first two terms in (5.7), $\chi_{Ag^+} - \chi_{Cu^+}$, is -29×10^{-6}; the next term is $Z\times17\times10^{-6}$ and the last two terms taken together have a maximum absolute value of 3×10^{-6}. It is seen that the term involving the density of states makes a major contribution to the calculated slope. (Better agreement, as indicated by the figures in parentheses may be achieved for the silver group if a value of $Z\times14\times10^{-6}$ is used.) The degree of agreement between the observed and calculated values suggests that the form of (5.7) is correct for the polyvalent solutes and that the solute ion contribution is fairly independent of the solvent. It is important to emphasize that the form of (5.7) appears to be correct even though the details of the calculation of the coefficient of Z may be in error.

The treatment does not explain, however, why, for example, the absolute value of initial slope of the silver–arsenic system is greater than that of the silver–antimony system, whereas the reverse is true in the corresponding copper base alloys. Also the results for the copper–silver solid solutions do not fit the scheme suggested for the polyvalent solutes. Thus, for example, (5.5) would predict for the slope of the silver–copper system 29×10^{-6} whereas the observed slope is 15.7×10^{-6}. The experimental slope was corroborated at a temperature at which the equilibrium concentration exceeded the solute concentration.

If $\chi_M^F(0)$ is expressed in c.g.s. e.m.u. per mole and $N(E)_{\zeta_0}$ in electrons per atom per electron volt, then β for copper as determined from (5.3) is approximately 30 and for silver approximately 100. Although it is not possible here to attach any special significance to the relative magnitudes, it is interesting to consider the origin of the constants.

It is believed that there are three terms which contribute to the susceptibility of the electron gas; the Pauli susceptibility χ_S, the Landau–Peierls susceptibility, χ_{LP} (Mott and Jones 1936), and the interband contribution, χ_{int} (Adams 1953). The Pauli susceptibility is given by

$$\chi_S = \mu_\beta^2 N(E)_{\zeta_0} \tag{5.8}$$

where μ_β is a Bohr magneton. In II an attempt was made to show that the ratio of the diamagnetism, χ_{LP} to the paramagnetism, χ_S, is $-1/3$ for the special form of the E, $\mathbf{k}$ relationship in the approximation to nearly free electrons. The integration of the Landau–Peierls formula was done, however, over only one quarter of the crystal, with the field in the (111) direction, about which the function is symmetrical. If the direction of the field and the (001) direction are made to coincide and the integration done over the whole surface, then χ_{LP} is given by

$$\chi_{LP} = -1/3\mu_\beta^2[1-(8E_0/\Delta E)]N(E)_{\zeta_0} \tag{5.9}$$

where E_0 is the free electron energy at k_0 and ΔE is the energy gap across

the zone boundary. The Landau–Peierls contribution is therefore, according to the approximation to nearly free electrons, equal to a constant times the density of states. The sign of χ_{LP} is positive, i.e. when $N(E)$ decreases the system becomes less paramagnetic. Klee and Witte (1953) attempted to explain the observed variation of the magnetic susceptibility in the ternary $MgCu_2$–$MgZn_2$ system using the paramagnetic Landau–Peierls term. Adams (1953, 1954) also pointed out that χ_{LP} gives a paramagnetic contribution when the Fermi surface is not overlapped. Jones (1934) implied that χ_{LP} always gives a diamagnetic contribution, but this is not true because, contrary to his suggestion, $\partial^2 E/\partial k_x \partial k_y$ is not small in the approximation to nearly free electrons.

Adams (1953) discussed the magnetic properties of an electron gas when the Fermi surface is near a zone boundary and found a diamagnetic term, χ_{int}, which is large under the same conditions as χ_{LP} and of the same order of magnitude. This contribution, χ_{int}, is proportional to the density of states (Adams 1959). Adams and Zitter (1954) interpreted the results of Klee and Witte as providing an experimental demonstration of the strength of the band–band interaction. They were able to make their claim because, according to their calculations, χ_{LP}, which is responsible for the rapid rise of the observed paramagnetism just before the Fermi surface touches the zone boundary, is constant after the Fermi surface touches the zone boundary. Since χ_{LP} varies directly with the density of states, the constancy of χ_{LP} implies a constancy of the density of states in the same region. With the zone involved in the work of Klee and Witte a rapid decrease, even more rapid than that found for copper and silver, in the density of states would be expected for $E > E_F$. It is therefore difficult to understand the constancy of χ_{LP} in this region claimed by Adams and Zitter. If χ_{LP} is not in fact constant, then it becomes difficult to distinguish between χ_{LP} and χ_{int}.

From this discussion it is thus seen that β may be regarded as the sum of the constants of proportionality relating χ_S, χ_{LP}, and χ_{int} to the density of states and it is not surprising that β_{Cu} and β_{Ag} should be so different.

As a result of the measurement of the magnetic properties of these alloys, something may be said, in a general way, regarding the rate of change of the density of states as a function of electron to atom ratio. The susceptibility, concentration curves show no abrupt changes of slope and in some systems such as silver–indium and copper–gallium, the relationship is quite linear up to an electron to atom ratio of 1.30. If it is reasonable to expect that the passing through of a peak in the density of states curve would have a noticeable effect on the magnetic properties, it follows that there is no peak in the density of states curve for either copper- or silver-based alloys in the range of electron to atom ratio investigated.

There are two other physical properties which have been measured for these systems and with which some correlation might be sought; these are the change in lattice parameter produced by 1 at.% of solute (Owen 1947) and the change in resistivity produced by 1 at.% of solute (Linde 1932*a*, 1932*b*). A relationship has been suggested between the volume changes and

the changes in resistivity by Blatt (1957). Owen found that the lattice distortion was approximately proportional to the valency of the solute. The solvent effect on the magnetic properties does not appear to depend directly on the relative rates of change of the lattice parameter with concentration. Thus it is found that the rate of change of the lattice parameter with concentration is Ag(V) > Cu(IV) and Cu(V) > Ag(IV) whereas the absolute values of the adjusted initial slopes (Figs. 6 and 7) are Ag(V) > Cu(IV) and Cu(V) < Ag(IV). There may be a small volume effect such as suggested by equation (5.2) but there is no evidence to prove this.

We would like to take this opportunity of correcting an error in II. The atomic susceptibility of the singly charged aluminum ion, $\chi_{Al}{}^{+}$, was calculated by Slater's method and reported as -10.6×10^{-6}. The correct value is -15.1×10^{-6}, which agrees much better with $-15.1_4\times10^{-6}$, which is the sum of $\chi_{Al^{3+}}$ and $\chi_{Al(3S)^2}$ shown in Table II.

SUMMARY

The results of the measurement at room temperature of the variation of the magnetic susceptibility with concentration are presented for the solid solutions formed by the four elements following silver in the periodic table with both silver and copper as solvents, and for the solid solutions, formed by the four elements following copper in the periodic table with silver as solvent. These are compared with the results, obtained earlier, paper II, for the solid solutions formed by the four elements following copper in the periodic table with copper as solvent.

The four series are similar in that the rate of increase of the diamagnetism of the solid solutions in a series increases with valency. In the silver series the rate is greater than in the copper series. In both solvents the initial slope of the susceptibility, concentration curves are approximately linear functions of valency.

The results of the measurements are discussed in terms of a model suggested in paper II. The explanation appears to give both qualitative and quantitative results in reasonable agreement with experiment for the monovalent–polyvalent systems.

The explanation suggested requires that the density of states at the Fermi surface in both copper and silver decreases upon the addition of a polyvalent solute. A less specific alternative to this would be to require only that the expression for the initial slope of the susceptibility, concentration curve contains a term which is proportional to Z, the excess valency, and that the constant of proportionality depends only on the solvent. This was done for the silver base alloys with the IVth period solutes and the constant of proportionality determined.

In order to test the explanation offered in paper II, it was necessary to calculate the density of states for silver by the approximation to nearly free electrons (Jones 1937). It is found that the Fermi energy corresponding to an electron to atom ratio of 1.0 occurs at an energy of about 1.0 electron

volt beyond the peak. The calculated ratio of the rate of decrease of the density of states, beyond the peak, copper to silver, is 0.8.

It is argued that since the susceptibility, concentration curves show no abrupt changes of slope and are, in some cases, quite linear, there is no peak in the density of states curve in either copper- or silver-based alloys with an electron to atom ratio in the range 1.0 to approximately 1.30.

The solid solutions in the copper–silver alloy systems are anomalous and behave as though they are phase mixtures, i.e. the susceptibility is approximately a linear function of the susceptibilities of the pure metals.

ACKNOWLEDGMENTS

We are indebted to Mr. R. Talman for making some of the measurements, to Dr. L. D. Calvert for making the lattice parameter determinations, and to Mr. D. S. Russell for carrying out the chemical analyses.

REFERENCES

ADAMS, E. N. 1953. Phys. Rev. **89**, 633.
——— 1959. Private communication.
ADAMS, E. N. and ZITTER, R. 1954. Phys. Rev. **96**, 1705.
BLACK, M. M. 1935. Mem. Proc. Manchester Lit. & Phil. Soc. **79**, 29.
BLATT, F. J. 1957. Phys. Rev. **108**, 285.
CHASTON, J. C. 1953. Annotated equilibrium diagrams, No. 10 (The Institute of Metals, London).
CHILDS, B. G. and PENFOLD, J. 1957. Phil. Mag. **2**, 389.
COHEN, M. H. and HEINE, V. 1958. Advances in Phys. **7**, 395.
CRAW, D. A. and HENRY, W. G. 1956. J. Sci. Instr. **33**, 22.
ENDO, H. 1925. Sci. Repts. Tôhoku Univ. **14**, 479.
HARTREE, D. R. and HARTREE, W. 1936. Proc. Roy. Soc. A, **157**, 490.
HENRY, W. G. and ROGERS, J. L. 1956*a*. Phil. Mag. **1**, 223.
——— 1956*b*. Phil. Mag. **1**, 237.
HOWARTH, D. J. 1953. Proc. Roy. Soc. A, **220**, 513.
——— 1955. Phys. Rev. **99**, 469.
HUME-ROTHERY, W. 1947. Atomic theory for students of metallurgy (The Institute of Metals, London), p. 239.
HUME-ROTHERY, W., MABBOTT, G. W., and CHANNEL-EVANS, K. M. 1934. Phil. Trans. Roy. Soc. London, **233**, 1.
JONES, H. 1934. Proc. Roy. Soc. A, **144**, 225.
——— 1937. Proc. Phys. Soc. **49**, 250.
——— 1955. Proc. Phys. Soc. A, **68**, 1191.
——— 1957. Proc. Roy. Soc. A, **240**, 321.
KLEE, H. and WITTE, H. 1953. Z. physik. Chem. **202**, 353.
KLEMENS, P. G. 1954. Australian J. Phys. **7**, 70.
KRUTTER, H. M. 1935. Phys. Rev. **48**, 664.
LINDE, J. O. 1932*a*. Ann. phys. **14**, 353.
——— 1932*b*. Ann. phys. **15**, 219.
MEYER, L. and WEINER, D. 1957. Phys. Rev. **108**, 1426.
MORTLOCK, A. J. 1953. Australian J. Phys. **6**, 410.
MOTT, N. F. and JONES, H. 1936. The theory of the properties of metals and alloys (The Clarendon Press, Oxford), pp. 118 and 208.
OWEN, E. A. 1944. J. Sci. Instr. **21**, 65.
——— 1947. J. Instr. Metals, **73**, 471.
OWEN, E. A. and EDMUNDS, I. G. 1938. J. Inst. Metals, **63**, 265.
OWEN, E. A. and PICKUP, L. 1933. Proc. Roy. Soc. A, **139**, 526.
OWEN, E. A. and ROBERTS, E. W. 1939. Phil. Mag. **27**, 294.
OWEN, E. A. and ROBERTS, E. A. O. 1953. J. Inst. Metals, **81**, 479.
OWEN, E. A. and ROWLANDS, V. W. 1940. J. Inst. Metals, **66**, 361.
PACAULT, A. 1946. Rev. sci. Paris, **84**, 169.
PAULING, L. 1927. Proc. Roy. Soc. A, **114**, 181.
PEISER, H. S., ROOKSBY, H. P., and WILSON, A. J. C. 1955. X-Ray diffraction by polycrystalline materials (The Institute of Physics, London), p. 656.

RAYNE, J. A. 1957. Phys. Rev. **108**, 22.
——— 1958. Phys. Rev. **110**, 606.
RAYNOR, G. V. 1944. Annotated equilibrium diagrams, No. 2 (The Institute of Metals, London).
ROWLAND, T. J. 1958. Private communication.
SLATER, J. C. 1936. Phys. Rev. **49**, 537.
SMIT, J. 1952. Physica, **18**, 587.
STEPHENS, G. O. and EVANS, E. J. 1936. Phil. Mag. **22**, 435.
TAMMANN, G. and OELSEN, W. 1930. Z. anorg. Chem. **186**, 257.

AN ILLUSTRATION OF A TYPE OF TRIPLE CORRELATION MEASUREMENT WHICH CAN BE EASILY INTERPRETED[1]

A. E. Litherland and G. J. McCallum[2]

ABSTRACT

The $Mg^{26}(He^4,n\gamma)Si^{29}$ reaction has been used to illustrate the simplifications introduced in the interpretation of triple angular correlations by choosing a target and bombarding particles of zero spin and by observing the emitted particles, in this case neutrons, in a counter fixed at 0° to the beam. The angular correlations of the gamma rays with respect to the incident beam then depend only upon the properties of the final states in the residual nucleus. The angular correlation of the electric quadrupole 2.03-Mev gamma ray is predicted uniquely by theory and this prediction has been verified experimentally. The angular correlations of the 1.28-Mev and 2.43-Mev gamma rays have yielded for the $E2/M1$ amplitude mixing ratios $+0.25\pm0.05$ or -3.4 ± 0.5 and -0.26 ± 0.08 or -1.10 ± 0.16 respectively. In addition, the experiment provides an illustration of the value of the recently discovered technique of neutron – gamma-ray discrimination in an organic scintillator.

1. INTRODUCTION

This paper provides an illustration of a particular type of triple angular correlation measurement which can be of considerable value in the determination of nuclear spectroscopic data from nuclear reactions. In this type of measurement aligned nuclear states are selected by the detection of the second radiation with a counter which is axially symmetrical with respect to the incident beam direction. The expression for the angular correlation of the third radiation, a gamma ray for example, is then the same as that derived for the decay of a nucleus aligned at low temperatures (Cox and De Groot 1953). In the case of the selection of aligned nuclear states from a nuclear reaction the relative contributions from the different magnetic substates are unknown unless the details of the formation and decay of the compound nucleus are specified. However, the magnetic substates that can be populated are limited by the spins of the incident and emergent particle and the target (Litherland 1959). The example given in this paper illustrates that in certain cases the summation over the magnetic substates can be eliminated. The gamma-ray angular correlations then depend only upon the properties of the states in the residual nucleus.

In the experiment to be described the reaction $Mg^{26}(He^4,n\gamma)Si^{29}$ was chosen for study because of the zero spin of the target nucleus and the bombarding particle.* If neutrons from the reaction are then observed at 0° to the beam only the $m = \pm 1/2$ substates of the levels in the Si^{29} residual nucleus are populated. This is because the orbital angular momentum vector of the

[1]Manuscript received March 22, 1960.
Contribution from the Chalk River Laboratories, Chalk River, Ontario.
Issued as A.E.C.L. No. 1031.
[2]Seconded from the Institute of Nuclear Sciences, Wellington, New Zealand.
*In cases where the spins of the target nucleus and projectile are not zero, it is sometimes possible to remove the uncertainties in interpretation due to the summation over the magnetic substates (Litherland and Ferguson 1959).

neutron is perpendicular to its direction of motion. Consequently, only the spin of the neutron can have a projection on the direction of motion of the neutron. The full theoretical expression for the angular correlation under these conditions is given in Section 2 of this paper.

The reaction $Mg^{26}(He^4,n\gamma)Si^{29}$ has a number of other advantages which make it suitable for triple correlation measurements of the type described above.

(*a*) The states in Si^{29} have been studied by a number of reactions and the spins and parities of the ground, the 1.28-, 2.03-, and 2.43-Mev states have been assigned (Endt and Braams 1957). In addition, some measurements by Litherland and Gove (1958) on the gamma rays from the $Mg^{26}+He^4$ reaction have given information on the cascading from the 3.07- and 3.62-Mev states in Si^{29}. The most prominent gamma rays observed from the reaction $Mg^{26}(He^4,n\gamma)Si^{29}$ are shown in Fig. 1 and the yield curves of these gamma rays are shown in Fig. 2.

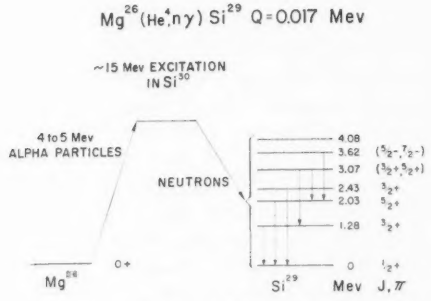

FIG. 1. The low-lying states in Si^{29}.

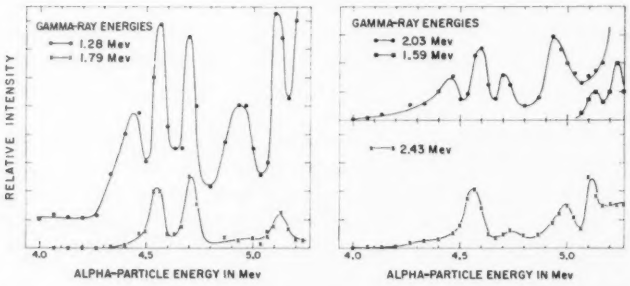

FIG. 2. Yield curves of the gamma rays from the reaction $Mg^{26}(He^4,n\gamma)Si^{29}$ obtained by Litherland and Gove (1958). The energy scale should be increased by approximately 25 kev.

(*b*) The low Q-value of the $Mg^{26}(He^4,n)Si^{29}$ reaction of +0.017 Mev (Endt and Braams 1957) ensures that at low bombarding energies only a limited number of low-lying states in Si^{29} are excited. Furthermore, the competing

reaction $Mg^{26}(He^4,p)Al^{29}$ has the unfavorable Q-value of -3.19 Mev which implies a low yield for this reaction at the He^4 energies used (i.e. between 4 and 5 Mev). Consequently, the gamma rays from the low-lying states of Si^{29} can be readily studied with little interference from other reactions or from the interference of multiple cascading in Si^{29} from high excited states. In the experiment described in this paper, it was possible to measure both the angular correlation of the gamma rays in coincidence with the neutrons and also, in some cases, to measure the angular distribution of the gamma rays with respect to the He^4 beam with the neutrons unobserved.

(*c*) The low Q-value of the reaction implies that the neutrons leaving Si^{29} in excited states will be of fairly low energy (2 to 4 Mev). This feature of the reaction is relevant to the correction for the finite size and asymmetry of the neutron counter used since the correction is smaller for low angular momentum neutrons than for high angular momentum neutrons. This effect is discussed briefly in Section 2 of this paper.

The practicability of the experiment described in this paper depends largely on the neutron – gamma-ray discrimination properties of some organic scintillators (Brooks 1959; Owen 1959) because it is necesssary to use an efficient fast-neutron detector which is insensitive to gamma rays, for the coincidence measurements. A method of discriminating against gamma-ray pulses from a large liquid scintillator is described in Sections 3 and 4. Sections 5 and 6 of this paper are devoted to a discussion of the experimental results and to the conclusions and possible future applications of the type of triple correlation measurement discussed in this paper.

2. THEORETICAL CONSIDERATIONS

Theoretical expressions for the angular distribution of the gamma rays with respect to the incident beam of alpha particles, suitable for the analysis of the reaction $Mg^{26}(He^4,n\gamma)Si^{29}$, have been given by Sharp *et al.* (1954). Expressions for the angular correlation of the gamma rays observed in coincidence with the neutrons are also given. In the latter case, the expression given is quite complex and involves extensive summations over vector coupling coefficients. As shown by Litherland and Ferguson (1959) considerable simplifications arise if the neutrons are observed in an axially symmetrical counter at 0° or 180° to the incident beam. In this case, the theoretical expression for the observed angular correlation of the gamma rays from the reaction is given by equation 1.

$$(1)\quad W_{LL'}(\theta) = \sum_{k,m} (-1)^{I+m+L+L'+\frac{1}{2}k} P(m)\ (JJm-m|k0) Z_1(LJL'J,Ik)\ Q_k P_k(\cos\theta).$$

In equation 1, the angular correlation of the gamma rays $W_{LL'}(\theta)$ is expressed in terms of Legendre polynomials. $P(m)$ is the population of the mth substate of the nuclear state of spin J, which decays to another state of spin I by emitting a gamma-ray quantum of total angular momentum L. The Clebsch–Gordan coefficient $(JJm-m|k0)$ has been tabulated by Sears

and Radtke (1954). The coefficient $Z_1(LJL'J,Ik)$ has been tabulated by Sharp *et al.* (1957). The attenuation coefficients Q_k can be calculated for a cylindrical gamma-ray counter by the method suggested by Rose (1953). Tables of these coefficients for 5 in. diameter by 4 in. long, 5 in. diameter by 6 in. long, and 3 in. diameter by 3 in. long NaI crystals have been prepared by Gove and Rutledge (1958) and Rutledge (1959). The full expression for the angular correlation must include a sum over the different multipole radiations that may be present. This expression, for the dipole–quadrupole case, is then given by equation 2.

$$W(\theta) = W_{1,1}(\theta)+2\delta W_{1,2}(\theta)+\delta^2 W_{2,2}(\theta) \tag{2}$$

In equation 2, δ is the amplitude of the electric quadrupole radiation present divided by the amplitude of the magnetic dipole radiation. An expression similar to equation 1 together with a table of angular distribution coefficients has been given by Wapstra *et al.* (1959).

Equation 1 also applies to the case when the neutron is unobserved and the angular distribution of the gamma rays is measured with respect to the beam. In this case, the populations of the gamma-ray emitting state have to be regarded as unknown parameters to be determined experimentally. If, however, the angular correlation of the gamma rays are observed in coincidence with the neutrons detected by an infinitely small counter situated at 0° to the incident beam then only the $m = \pm 1/2$ substates are populated as discussed earlier. The angular correlation of the gamma rays from the reaction then depends only upon the properties of the states of the residual nucleus. This conclusion does not depend upon the assumption that the reaction proceeds through an isolated resonance of the compound nucleus. For example, the angular correlation of an electric quadrupole gamma ray arising from a $5/2 \rightarrow 1/2$ transition is uniquely predicted to be

$$W(\theta) = 1+\frac{4}{7}Q_2P_2(\cos\theta)-\frac{4}{7}Q_4P_4(\cos\theta). \tag{3}$$

The 2.03-Mev gamma ray which was studied in the experiment reported in this paper arises from such a transition. Since the spins of the other states studied are known, a measurement of the angular correlation coefficients of

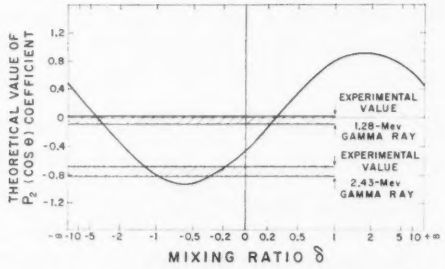

FIG. 3. The theoretical values of the triple correlation coefficient of $P_2(\cos\theta)$ are shown as a function of δ the $E2/M1$ amplitude ratio, together with the experimental values (discussed in Section 5) obtained from the angular correlations of the 1.28- and 2.43-Mev gamma rays.

the de-excitation gamma rays serves to determine the magnetic dipole – electric quadrupole mixing ratio δ. The angular correlation coefficient a_2/a_0 is shown as a function of δ in Fig. 3 for the case of a $3/2 \rightarrow 1/2$ transition.

Since infinitely small neutron counters cannot be used to detect the neutrons at 0° to the beam, it is necessary to consider the effect of the finite size of a neutron counter which is large enough to give a significant coincidence counting rate. As this effect has been treated in some detail by Litherland and Ferguson (1959), only their conclusions will be quoted here. In the particular reaction discussed in this paper the effect of using a small axially symmetrical neutron counter of half angle ξ is to introduce a contribution to the angular correlation of the gamma rays from the $m = \pm 3/2$ substates. In the case of the angular correlation of the 2.03-Mev gamma ray discussed in this paper the angular correlation then becomes

$$(4)\quad W(\theta) = 1+\frac{4}{7}Q_2P_2(\cos\theta)-\frac{4}{7}Q_4P_4(\cos\theta)+\frac{A\xi^2}{1+B\xi^2}\left[1+\frac{1}{7}Q_2P_2(\cos\theta)+\frac{6}{7}Q_4P_4(\cos\theta)\right].$$

In equation 4, A and B are unknown constants which are related to the formation and decay matrix elements of the compound nucleus. These constants can be calculated only if assumptions are made regarding the formation and decay of the compound nucleus. For example, consider the case of a 2+ resonance in Si^{30} formed by the capture of d-wave alpha particles by Mg^{26}. If this resonance then decays by the emission of a $d_{3/2}$ neutron to the 5/2+ 2.03-Mev excited state of Si^{29} it can be shown, by considering the triple angular correlation in detail, that the coefficients A and B are $+9/4$ and $-3/8$ respectively. Figure 4 shows the exact calculation of the angular correlation coefficients as a function of the angle ξ (no longer small). Two cases are shown; the compound state of spin 2+ decays either by the emission of an $s_{1/2}$ neutron or by the emission of a $d_{3/2}$ neutron. Since the emission of an $s_{1/2}$ neutron can result only in the population of the $m = \pm 1/2$ substates of the residual nucleus there is no attenuation of the correlation coefficient as a result of the finite size of the neutron counter.

3. APPARATUS

Experiments were carried out using 50 mμa of 4.5 to 5.0 Mev $He^{4}{}_{2+}$ ions from the Chalk River 3-Mv electrostatic accelerator. The ions bombarded a thin metallic target of Mg^{26} (50 kev thick for 4.7-Mev alpha particles) deposited onto a 0.02-in. tantalum backing.* The gamma rays were detected by a 5 in. diameter by 4 in. long NaI (Tl) crystal, the front face of which was 6.5 inches from the target. The crystal could be rotated from 0° to 120° with respect to the He^4 beam. The neutrons were detected at 0° by a 3 in. diameter by 3 in. long NE 212 liquid scintillator,† and a pulse-shape

*Obtained from the Electromagnetic Separator Group, Atomic Energy Research Establishment, Harwell, England.

†Obtained from Nuclear Enterprises Ltd., Winnipeg, Manitoba, Canada.

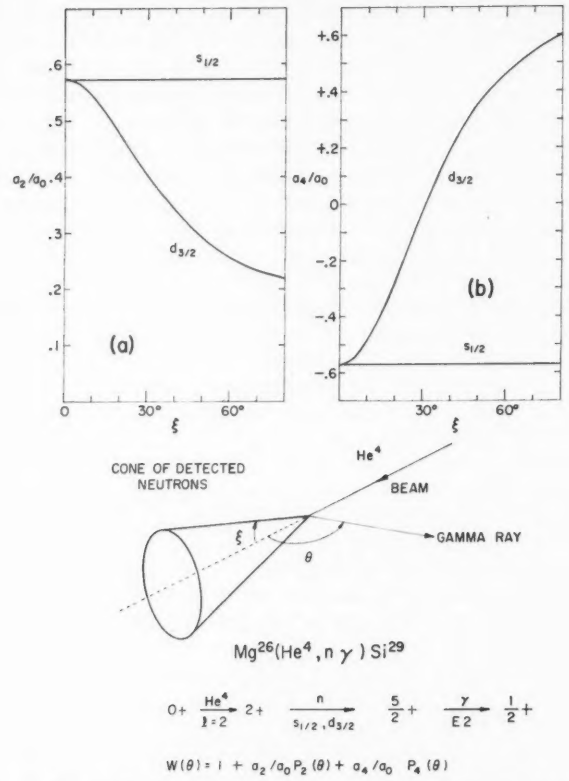

FIG. 4. The effect of the finite size of the neutron counter is illustrated in a particular case.

discrimination circuit of the type first described by Owen (1959) was used to discriminate between neutrons and gamma rays.

The experimental arrangement is illustrated in Fig. 5. At 0° to the beam the liquid scintillator could not be placed in a position to ensure complete

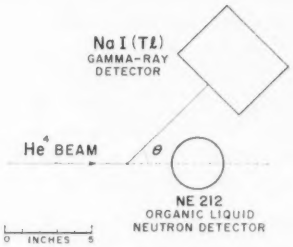

FIG. 5. Experimental arrangement of counters as described in the text.

axial symmetry because the scintillator did not completely fill its container. It was therefore placed on the beam axis with its axis of symmetry perpendicular to the beam at a distance of 4 inches from the target. The effect of the deviation from axial symmetry in the reaction studied is small for reasons discussed below.

A block diagram of the electronic equipment used in the experiment is shown in Fig. 6. The NaI (Tl) crystal was optically coupled to a Dumont

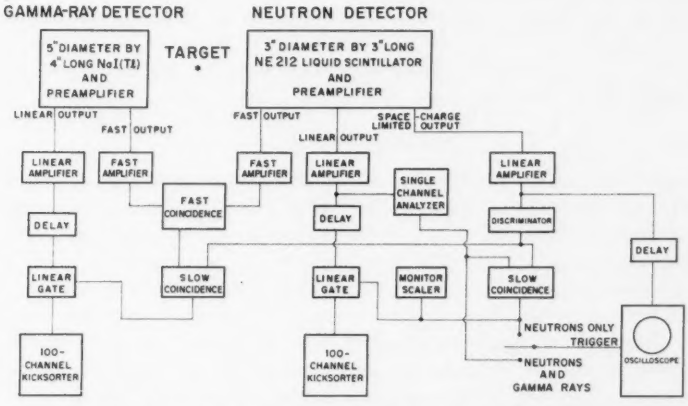

FIG. 6. Block diagram of the electronic equipment used in the experiment.

6364 photomultiplier and a Dumont 6363 photomultiplier was coupled to the liquid scintillator. Two pulses were taken from the multiplier connected to the NaI (Tl) crystal, a "linear" pulse for pulse height analysis from the last but one dynode and a "fast" pulse for coincidence analysis from the anode. Three pulses were taken from the multiplier connected to the liquid scintillator, a "linear"* pulse from the fifth dynode from the anode, a "fast" pulse from the third dynode from the anode, and a space-charge limited pulse from the last dynode. The space-charge limited pulse can be used to discriminate between neutron and gamma-ray induced pulses from the liquid scintillator in the manner described by Owen (1959) and by Litherland *et al.* (1959). The Dumont 6363 multiplier was used with approximately 1500 volts between anode and photocathode. The last dynode-to-anode voltage was made remotely variable between the limits of approximately 0 and 15 volts. For the measurements described in this paper and the particular photomultiplier used the optimum last dynode-to-anode voltage was found to be 4 volts. Under these conditions, the neutron-induced pulses at the last dynode (in the energy range studied) had a prominent negative component whereas the gamma-ray induced pulses were predominantly positive. After amplification, neutron-induced pulses could be selected by a discriminator which was triggered by the negative portion of the space-charge limited pulse.

*The pulse height, from a proton-induced pulse in a liquid scintillator, is not of course a linear function of the proton energy.

The outputs of the neutron discriminator and a fast coincidence unit of the type described by Bell *et al.* (1953) (resolving time $2\tau \sim 50$ mμsec) were applied to a slow coincidence unit which consequently gave an output only when a neutron and a gamma ray were in fast coincidence. This output pulse was used to open a linear gate which transmitted to a 100-channel transistor pulse-height analyzer* those gamma-ray pulses which were in coincidence with neutrons. A second pulse height analyzer displayed the spectrum of all neutrons within an energy range determined by the settings on a single-channel pulse-height analyzer and which were in coincidence with an output from the discriminator set on the space-charge limited pulses. The scaler shown in Fig. 6 was used as a monitor so that the coincidence spectra at each angle could be normalized to a given neutron flux.

4. EXPERIMENTAL PROCEDURE

When we were setting up the electronic equipment shown in Fig. 6, the experimental procedure adopted was to first adjust the neutron – gamma-ray discrimination circuit using a $\frac{1}{4}$ g plutonium–beryllium alloy as a source of neutrons and gamma rays. This was most readily accomplished by observing the space-charge limited pulses on an oscilloscope which was triggered by the pulses from a single channel analyzer set on the linear pulses. The single channel analyzer window was adjusted with the help of calibrating gamma-ray sources such as Na^{22} to cover the approximate range of proton recoil pulses of interest in the experiment. In this way it was possible to adjust the last dynode–anode voltage so that the neutron and gamma-ray induced pulses were opposite in sign over the proton recoil energy range studied. Adjusting the level of the discriminator on the space-charge saturated pulses and throwing the switch shown in Fig. 6 alternately to the positions marked "neutrons and gamma rays" and "neutrons only" permitted the discriminator level at which gamma-ray pulses were eliminated to be rapidly achieved. During the experiment, the operation of the neutron – gamma-ray discriminator was continuously monitored by the oscilloscope.

The satisfactory operation of the complete electronic system was ascertained by observing neutron – gamma-ray coincidences from the Pu–Be source and then observing the lack of coincidences from a Co^{60} source. Finally, small adjustments were made using the neutrons and gamma rays from the $Mg^{26}(He^4,n\gamma)Si^{29}$ reaction.

For convenience in setting up the apparatus, the upper and lower limits to the proton recoil spectrum were defined by the discriminator set on the space-charge limited pulse. This is possible because the negative part of the space-charge saturated pulse, characteristic of neutron-induced pulses, first increases and then decreases with increasing proton recoil energy. Consequently, the neutron-energy discriminator bias was adjusted so that neutrons feeding the fourth excited state in Si^{29} (shown in Fig. 1) were not counted. This setting was checked by the absence of 1.79-Mev gamma rays from the decay of the fourth excited state to the first excited state of Si^{29}. The action

*Obtained from Computing Devices of Canada Limited, Ottawa, Ontario, Canada.

of the neutron – gamma-ray discrimination circuit is illustrated in Fig. 7 where the spectrum of gamma-ray pulses from the NaI (Tl) crystal, in fast coincidence with pulses from the liquid scintillator, is shown (*a*) with the

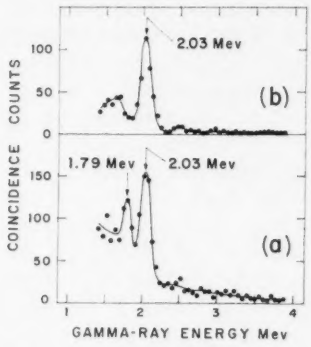

FIG. 7. Coincidence pulse spectra taken (*a*) without neutron – gamma-ray discrimination; and (*b*) with neutron – gamma-ray discrimination.

discriminator inoperative and (*b*) with the discriminator in operation. The 1.79-Mev peak seen in curve (*a*) arises from the de-excitation of the 3.07 level in Si^{29}. This peak is not visible in curve (*b*) showing that (i) the neutron – gamma-ray discriminator bias is set sufficiently high to eliminate (n,γ) coincidences from the excitation of the 3.07 level and (ii) (γ,γ) coincidences are effectively discriminated against. This latter feature is necessary because the 3.07-Mev state in Si^{29} also cascades through the 2.03-Mev state by emitting 1.04-Mev and 2.03-Mev gamma rays. As a further check on the rejection of (γ,γ) coincidences by the neutron – gamma-ray discrimination circuit a Co^{60} coincidence spectrum was measured both with and without the discrimination circuit operative. A reduction in coincidence counting rate by a factor of over 200 was obtained with the discrimination circuit in operation.

The angular correlations were carried out at 4.74- and 4.94-Mev He^4 bombarding energy with the neutron counter fixed first at 0° and then at 90° to the beam. The energy of the $He^4{}_{2+}$ ions was measured relative to the 4.00-Mev resonance in the reaction $Be^9(He^4,n\gamma)C^{12}$ (Gibbons and Macklin 1959). The angular correlations of the 1.28-, 2.03-, and 2.43-Mev gamma rays were obtained simultaneously at 4.94-Mev bombarding energy. At 4.74 Mev the yield of 2.43-Mev gamma rays was too low to permit an accurate angular distribution to be made.

Since the gamma rays traverse the neutron counter when they are observed near 0° a correction was made for the resulting attenuation. This correction was determined by observing the angular distribution of the 2.185-Mev gamma rays from a Pr^{144} radioactive source placed in the position of the target. The neutron counter was at 0° for this measurement. As the correction was large (amounting to $\sim$40% between 0° and 20°) it would be an advantage to detect

the outgoing neutrons near 180° and thus obviate the correction for attenuation of the gamma rays. This possibility is discussed below.

5. RESULTS AND DISCUSSION

In Fig. 8, the angular correlations of the 2.03-Mev electric quadrupole gamma rays from the decay of the 5/2+ second excited state of Si^{29} to the

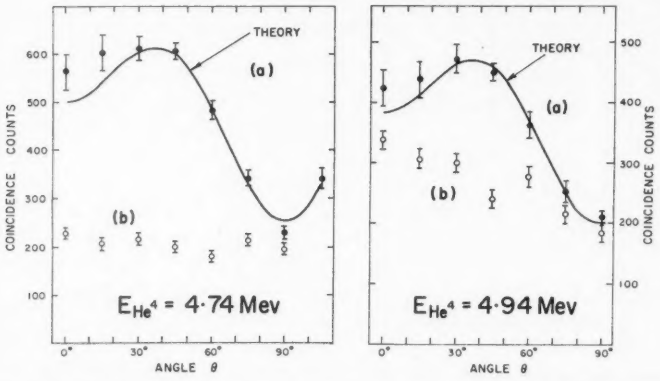

FIG. 8. The triple angular correlations from the reaction $Mg^{26}(He^4,n\gamma)Si^{29}$ leading to excitation of the 2.03-Mev level in Si^{29} are shown for two incident alpha-particle energies and for two geometrical arrangements of the counters.
(*a*) The neutron counter situated at 0° to the beam (Fig. 5) and the coincidence counting rate observed as a function of the angle θ of the gamma-ray counter.
(*b*) A similar correlation with the neutron counter situated at 90° to the beam.

1/2+ ground states are shown. The theoretical correlation, derived from equation 1, for the case with infinitely small neutron counter fixed at 0° (marked (*a*) in Fig. 8) and an infinitely small gamma-ray counter at an angle θ is $1+4/7[P_2(\cos\theta)]-4/7[P_4(\cos\theta)]$. The theoretical curves shown in Fig. 8 are corrected only for the finite aperture of the gamma-ray counter. The calculations of Gove and Rutledge (1958) were used for this correction. Agreement with theory is quite good despite the finite size of the neutron counter and its lack of exact axial symmetry. The results of a least squares analysis of the angular correlation data at the two energies are given in Table I. The

TABLE I

Angular correlation coefficients

He^4 energy	a_2/a_0	a_4/a_0
4.74 Mev	+0.62±0.06	−0.43±0.06
4.94 Mev	+0.55±0.06	−0.34±0.07
Theory	0.53	−0.43

attenuated theoretical coefficients are also quoted in Table I. The least squares fits reported in this paper were carried out using the Chalk River Datatron computer.

The good agreement with theory, without the correction for the finite size and partial asymmetry of the neutron counter, can be explained partly by the smallness of the correction term given in Section 2 of this paper and partly by assuming that the neutrons at the two resonances are predominantly *s*-wave, because as shown in Fig. 4 for *s*-waves the predicted triple correlation is independent of the angle of the neutron counter. This assumption is supported by the measurement, at 4.74-Mev bombarding energy, of the angular distribution of the 2.03-Mev radiation with the neutrons unobserved. These angular distribution coefficients are consistent with the neutrons being 60% *s*-wave and 40% *d*-wave. However, the observed triple correlations with the neutron counter at 90° are different at the two resonances studied and are different from the 0° correlations showing that there are differing admixtures of the higher angular momentum neutrons at the two energies.

Using the theoretical expression for the angular distributions given in equation 1 together with the measured angular distribution coefficients for the 2.03-Mev radiation given in Table II*a*, it is possible to determine the

TABLE II

Angular distribution coefficients

	He^4 energy	Gamma-ray energy	a_2/a_0	a_4/a_0
(*a*)	4.74 Mev	2.03 Mev	$+0.39\pm0.06$	-0.16 ± 0.07
(*b*)	4.94 Mev	2.43 Mev	-0.48 ± 0.08	

populations of the substates of the 2.03-Mev (5/2+) state in Si^{29}. These are quoted in Table III*a*. These population numbers give support to the con-

TABLE III

Population numbers deduced from angular distribution coefficients

	He^4 energy	Gamma-ray energy	$P(\pm1/2)$	$P(\pm3/2)$	$P(\pm5/2)$
(*a*)	4.74 Mev	2.03 Mev	0.36 ± 0.04	0.12 ± 0.04	0.02 ± 0.03
(*b*)	4.94 Mev	2.43 Mev	0.41 ± 0.04	0.09 ± 0.04	

jecture made earlier that the neutrons observed at each resonance are predominantly of low angular momentum.

The arguments outlined above are given because the experimental conditions were not ideal. Ideally, the neutron counter should have been axially symmetrical and it should have been adjustable in distance from the target. The effect of the finite size of the counter could then have been investigated by varying the distance of the counter from the target and observing the change in the angular correlation pattern. Such experiments would require an axially symmetrical counter with a hole through it to allow the beam to reach the target. The distance of the neutron counter would not then be limited by the necessity for the gamma-ray counter to observe the gamma rays near 0°. Such experiments are being planned. In order to interpret the results discussed in this paper, it will be assumed that the effects of the finite size of the neutron

counter are negligible compared with the errors in determining the experimental coefficients. The measurements of the angular distributions of the 2.03- and 2.43-Mev gamma rays and the triple angular correlation of the 2.03-Mev gamma ray can be used to support this assumption.

The correlations of the 1.28-Mev gamma rays obtained at 4.74- and 4.94-Mev bombarding energies are shown in Fig. 9, and a least squares fit of the

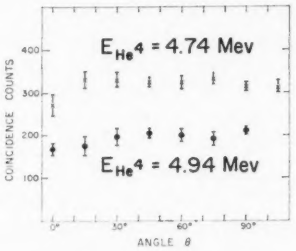

FIG. 9. Triple angular correlations of the 1.28-Mev gamma ray are shown for two incident alpha-particle energies. The neutron detector was at 0° to the incident beam in both cases.

data to an expression of the form $1 + \alpha_2 P_2 (\cos \theta)$ was obtained. From the two correlations a mean value of $\alpha_2 = -0.05 \pm 0.07$ was obtained. In Fig. 3, the experimental value of the $P_2 (\cos \theta)$ coefficient is given together with the theoretical value plotted as a function of δ, the magnetic dipole – electric quadrupole amplitude mixture. The theoretical coefficients were obtained from equation 1 with $P(m) = 1/2$ for $m = \pm 1/2$ and $P(m) = 0$ for $m \pm 3/2$. The theoretical value of the coefficient has been modified for the effects of the finite solid angle subtended by the gamma-ray counter. The mixing ratio δ (defined in Section 2) deduced from Fig. 3 is $\delta = +0.25 \pm 0.05$ or -3.4 ± 0.5.

At 4.74 Mev the yield of the 2.43-Mev gamma rays was too low to permit an accurate triple angular correlation measurement. The correlation of the 2.43-Mev radiation at 4.94 Mev, with the neutron counter at 0°, is shown in Fig. 10 together with the correlation obtained with the neutron detector at 90°. A least squares fit of the data, with the neutron counter at 0°, yielded a value of -0.75 ± 0.07 for the $P_2 (\cos \theta)$ coefficient. The angular distribution of the 2.43-Mev gamma ray with neutrons unobserved was measured at three angles from which a value of -0.48 ± 0.10 for the $P_2 (\cos \theta)$ coefficient was deduced. This coefficient is included in Table II*b* and from it the populations listed in Table III*b* were deduced. As in the case of the formation of the 2.03-Mev state these populations imply that the neutrons to the 2.43-Mev state are of low angular momentum. Consequently correcting only for the angular aperture of the gamma-ray counter, a mixing ratio of $\delta = -0.26 \pm 0.08$ or -1.10 ± 0.16 was obtained from Fig. 3.

7. CONCLUSIONS

Triple angular correlations from the reaction $Mg^{26}(He^4, n\gamma)Si^{29}$ have been used to determine values for the states in Si^{29}. The ambiguity of the results

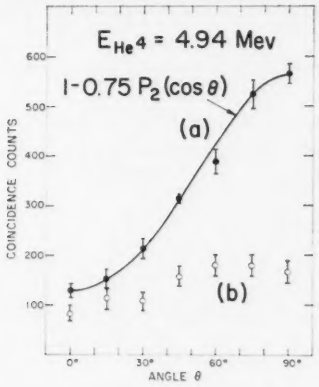

FIG. 10. Triple correlations of the 2.43-Mev gamma ray with neutron detector at 0° (*a*), and at 90° (*b*), for a bombarding energy of 4.94 Mev. The solid curve is a least squares fit to the experimental data taken with the neutron detector at 0°.

can in principle be eliminated by observing the linear polarization of the gamma rays. This was done by McGowan and Stelson (1958) for a number of gamma-ray transitions produced by Coulomb excitation. In addition, the experimental results described in this paper have illustrated the considerable advantages to be gained in the interpretation of triple correlation data by choosing zero-spin target and projectiles and by observing the neutrons at 0° to the beam of projectiles. The simplification in the interpretation is, however, obtained at the price of the experimental difficulty of using counters which are axially symmetrical with respect to the beam and which are situated at 0° or 180° to the beam. Though such ideal counters were not used in the experiment described above, the effect of the finite size of the counter and its lack of axial symmetry was quite small because the neutrons observed were mainly of low angular momentum. Since, in general, these simplifying conditions do not hold, further experiments are planned using a neutron counter which is axially symmetrical and which has a hole through its center so that neutrons can be observed at 180° to the incident beam. This counter will remove the uncertainties due both to the attenuation of the gamma rays in traversing the neutron detector when it is mounted at 0° to the incident beam, and to the azimuthal asymmetry of the detector. In addition, it would also permit the experimental evaluation of the correction to the data for the finite size of the neutron counter.

Since He^3 and H^3 induced reactions can excite a large variety of nuclear states, an attempt has been planned to use an axially symmetrical junction counter with a hole through the center to detect the alpha particles and protons from these reactions at 180° to the incident beam. A junction counter with these characteristics has been successfully made and tested by McKenzie and Bromley (1959).

ACKNOWLEDGMENTS

We are indebted to R. B. Owen of the United Kingdom Atomic Energy Authority for sending the details of his work on neutron – gamma-ray pulse-shape discrimination prior to publication.

We also wish to express our thanks to P. G. Ashbaugh and his staff for the successful operation of the accelerator and to C. E. L. Gingell for his help with the electronic system used in the experiments.

REFERENCES

BELL, R. E., GRAHAM, R. L., and PETCH, H. E. 1952 Can. J. Phys. **30**, 35.
BROOKS, F. D. 1959. Nuclear Instr. and Methods, **4**, 151.
COX, J. A. M. and DE GROOT, S. R. 1953. Physica, **19**, 683. See also GRAY, T. P. and SATCHLER, G. R. 1955. Proc. Phys. Soc. (London), A, **68**, 349.
ENDT, P. M. and BRAAMS, C. M. 1957. Revs. Modern Phys. **29**, 683.
GIBBONS, J. H. and MACKLIN, R. L. 1959. Phys. Rev. **114**, 571.
GOVE, H. E. and RUTLEDGE, A. R. 1958. Chalk River Report CRP-755, Chalk River, Ontario, Canada.
LITHERLAND, A. E. 1959. Bull. Am. Phys. Soc. Ser. II, **4**, 58.
LITHERLAND, A. E., ALMQVIST, E., BATCHELOR, R., and GOVE, H. E. 1959. Phys. Rev. Letters, **2**, 104.
LITHERLAND, A. E. and FERGUSON, A. J. 1959. To be published.
LITHERLAND, A. E. and GOVE, H. E. 1958. Unpublished.
MCGOWAN, F. K. and STELSON, P. H. 1958. Phys. Rev. **109**, 901.
MCKENZIE, J. M. and BROMLEY, D. A. 1959. Private communication; also Phys. Rev. Letters, **2**, 303.
OWEN, R. B. 1959. Nucleonics, **17** (9), 92.
ROSE, M. E. 1953. Phys. Rev. **91**, 610.
RUTLEDGE, A. R. 1959. Chalk River Report CRP-851, Chalk River, Ontario, Canada.
SEARS, B. J. and RADTKE, M. G. 1954. Chalk River Report TPI-75, Chalk River, Ontario, Canada.
SHARP, W. T., KENNEDY, J. M., SEARS, B. J., and HOYLE, M. G. 1957. Chalk River Report CRT-556, Chalk River, Ontario, Canada.
WAPSTRA, A. H., NIJGH, G. J., and VAN LIESHOUT, R. 1959. Nuclear spectroscopy tables (North-Holland Publ. Co., Amsterdam).

MAGNETO-OPTICAL ROTATION IN VERY HIGH FIELDS[1]

RICHARD STEVENSON

ABSTRACT

Magneto-optical rotation by transmission through or reflection from solids is examined by the classical free electron theory, with the view of taking such a measurement using fields in the megagauss range. In general the rotation is a markedly non-linear function of the magnetic field, and in some cases can change in sign as the field increases. For very low fields the rotation varies directly with B, but in the high field limit the rotation varies inversely with the field. For substances in which the intercollision time of the electron is small, measurements of the Kerr rotation (i.e. by reflection) will give the electron mobility as a function of the magnetic field, and thus will give important data which can be used in conjunction with high field magnetoresistance experiments.

1. INTRODUCTION

Measurements of the Faraday rotation at microwave and infrared frequencies have been suggested and used a number of times to obtain values of the effective electron mass in non-ferromagnetic substances. The theory for low fields at infrared frequencies as outlined by Mitchell (1955) indicates that the rotation has a λ^2 dependency and varies directly with the field. The theory of such experiments at microwave frequencies has been considered by Rau and Caspari (1955) and more recently by Lin (1959). More general use of Faraday rotation experiments has been considered by Stephen and Lidard (1959). Measurements by Suhl and Pearson (1953), Stern and Myers (1958), and Brown and Lax (1959) indicate that it is an acceptable technique for measuring the effective electron mass at low fields.

When the magnetic field is very large, approaching the megagauss mark, it appears that the energy density of the field can affect the band structure of the solid. Since some cyclotron resonance experiments are done at high fields, it would seem worth while to have another type of experiment which could be performed under similar conditions and would give similar information about the effective electron mass. Then it would be possible to study what effects, if any, could be attributed to the presence of the very strong field itself. For example, the high field experiments of Keyes *et al.* (1956) show a variation of effective mass, the reason for which is somewhat obscure without subsidiary information.

2. OUTLINE OF THE THEORY AND RESULTS

The solid is described in optical terms by a complex index of refraction

$$N = n - ik$$

and the index for radiation circularly polarized in one sense N_+ is distinguished

[1]Manuscript received August 31, 1959.
Contribution from the Eaton Electronics Research Laboratory, Physics Department, McGill University, Montreal, Que. Supported in part by the Office of Naval Research (U.S. Navy).

from that in the opposite sense N_-. If the extinction coefficient k is not zero the light transmitted in the Faraday effect or reflected in the Kerr effect will be elliptically polarized and the major axis of the ellipse rotated through an angle ϕ. In terms of the indices N_+ and N_-, the rotations and ellipticities (Argyres 1955) are:

(*a*) Faraday rotation and ellipticity

$$\phi_F = \frac{1}{2}\frac{\omega z}{c}\,\mathrm{R}[N_+ - N_-] \tag{1}$$

$$\epsilon_F = -\tanh\left\{\frac{1}{2}\frac{\omega z}{c}\,\mathrm{I}[N_+ - N_-]\right\}$$

(*b*) Kerr rotation and ellipticity

$$\phi_K = -\mathrm{I}\left[\frac{N_+ - N_-}{N_+ N_- - 1}\right] \tag{2}$$

$$\epsilon_K = -\mathrm{R}\left[\frac{N_+ - N_-}{N_+ N_- - 1}\right]$$

where R and I refer to the "real and imaginary parts of", ω is the frequency of incident radiation, z is the thickness of the sample, and c the velocity of light.

The rotation of the polarized light is due to the electrons in the solid, which have the equation of motion

$$\ddot{\mathbf{s}} + \frac{1}{\tau}\dot{\mathbf{s}} + \omega_0^2 \mathbf{s} = -\frac{e}{m^*}(\mathbf{E} + \dot{\mathbf{s}} \times \mathbf{B}) \tag{3}$$

where $\mathbf{s}$ = displacement vector of the electron,
τ = mean collision time of the electron,
ω_0 = the resonant frequency of a bound electron,
$\mathbf{E}$ = incident radiation field,
$\mathbf{B}$ = external magnetic field.

All quantum mechanical effects are contained in attributing to the electron an "effective mass" m^*. The term involving ω_0 will be dropped, so that the theory strictly applies only to free electrons. The type of analysis has been explained by Sommerfeld (1954) and its applicability has been considered by Givens (1958).

The incident beam of plane-polarized radiation is represented by:

$$E_\pm = A e^{i(k_\pm z - \omega t)} \tag{4}$$

where $$k_\pm = (\omega/c)\, N_\pm.$$

Then using Maxwell's equations we can obtain

$$N_\pm^2 = 1 + i\frac{\sigma}{\epsilon_0 \omega} - \frac{\sigma_0}{\epsilon_0 \omega}\frac{1}{(\omega\tau \pm \omega_c \tau) + i} \tag{5}$$

where we have defined the static conductivity,

$$\sigma_0 = \eta e^2 \tau / m^*$$

with η being the number of electrons per unit volume, and the cyclotron frequency is

$$\omega_c = eB/m^* .$$

The relation between the a-c. conductivity σ and the static conductivity is derived in a somewhat similar manner, as by Dresselhaus *et al.* (1955). According to our definition (4) of the incident radiation, we obtain

$$\sigma = \sigma_0\left[\frac{1-i\omega\tau}{1+(\omega_c^2-\omega^2)\tau^2-2i\omega\tau}\right]. \tag{6}$$

And from these equations the terms in (1) and (2) can be evaluated.

$$\begin{aligned}
\mathrm{R}[N_+-N_-] &= -\frac{\sigma_0}{\epsilon_0\omega}\frac{\nu_c}{n^2+k^2}\frac{n(\nu^2-\nu_c^2-1)+2k\nu}{(\nu^2-\nu_c^2-1)^2+4\nu^2} \\
\mathrm{I}[N_+-N_-] &= -\frac{\sigma_0}{\epsilon_0\omega}\frac{\nu_c}{n^2+k^2}\frac{k(\nu^2-\nu_c^2-1)+2n\nu}{(\nu^2-\nu_c^2-1)^2+4\nu^2} \\
\mathrm{R}[N_+N_--1] &= 2(n^2+k^2-1)-\frac{2\sigma_0}{\epsilon_0\omega}\frac{\nu(\nu_c^2-\nu^2-1)}{(\nu^2-\nu_c^2-1)^2+4\nu^2} \\
\mathrm{I}[N_+N_--1] &= -4nk-\frac{2\sigma_0}{\epsilon_0\omega}\frac{\nu_c^2+\nu^2+1}{(\nu^2-\nu_c^2-1)^2+4\nu^2}
\end{aligned} \tag{7}$$

where

$$\nu = \omega\tau,$$

$$\nu_c = \omega_c\tau.$$

Then from (1) a formula can be obtained for the Faraday rotation, which gives the general dependence on the magnetic field B.

$$|\phi_F| = \frac{e^2z}{2c\epsilon_0}\frac{\sigma_0}{\alpha}\frac{B}{m^{*2}}\frac{\nu^2}{\omega^2}\frac{1}{n^2+k^2}\left[\frac{n(\nu^2-\nu_c^2-1)+2k\nu}{(\nu^2-\nu_c^2-1)^2+4\nu^2}\right] \tag{8}$$

where the electron mobility

$$\alpha = e\tau/m^*$$

has been introduced. When the external field is small, i.e. $\nu_c \ll 1$, (8) reduces to either of the formulae derived by Mitchell (1955) or Rau and Caspari (1955) depending whether or not ν is large or small.

The very high field behavior is of some interest. Even at low fields the rotation becomes non-linear with respect to B, as has been reported by Brown and Lax (1959). As the field increases the Faraday rotation reaches a maximum, and can change in sign. For extremely high fields the rotation loses its dependence on the effective electron mass and tends to vary inversely with the field

$$|\phi_F| = \frac{\eta e}{2\epsilon_0 c}\frac{z}{n\nu^2}\frac{1}{B}. \tag{9}$$

Thus, however useful this technique may be at low fields to obtain values of

m^*, it does not appear that such an experiment can be used with the very high pulsed fields to give information complementary to that obtained from cyclotron resonance.

Measurements of the Kerr rotation evidently will give useful information about electron transport in metals at high fields. For most metals the inter-collision time of the electron is small, of the order of 10^{-15} sec or less at ordinary temperatures. Then in an experiment most metals will satisfy the conditions that ν^2, $\nu_c^2 \ll 1$ at infrared frequencies and fields up to a megagauss. From the factors (7) one can obtain an expression for the Kerr rotation of metals

$$|\phi_K| = \frac{n}{2(n^2+k^2)} \frac{e\tau}{m^*} B \tag{10}$$

which formula contains the assumption that the static conductivity of the metal is large. To give an idea of the size of the effect we can consider a metal such as zinc with the representative parameters $\tau \cong 10^{-16}$ sec and $m^* = .02\, m_0$ at a field $B = 10^6$ gauss. Then the Kerr rotation is calculated to be $\phi_K \sim 6°$, which is easily measurable.

The interesting feature of (10) is that it allows measurements of the electron mobility as a function of the magnetic field to be made independently of magnetoresistance measurements. Thus knowing the effective electron mass, it is possible to obtain data on the field dependence of the electron collision time τ. This is a topic of some theoretical interest on which there are evidently no experimental data. The measurement of electron mobility should also be useful in the accumulation of data on high field behavior of transport properties.

Since one effective mass has been used the model is strictly correct only for solids with spherical energy surfaces, which is, of course, consistent with the application of free electron theory. The quantum mechanical treatment of this type of problem gives the same results as the free electron theory, and specific high field behavior which causes a depression of the Fermi level and a removal of the degeneracy of the electrons (Kahn and Frederikse 1959) does not invalidate the use here of the free electron model. In some substances it may be possible to observe oscillatory behavior of the optical properties at the high fields.

REFERENCES

ARGYRES, P. N. 1955. Phys. Rev. **97**, 334.
BROWN, R. N. and LAX, B. 1959. Bull. Am. Phys. Soc. **4**, 133.
DRESSELHAUS, G., KIP, A. F., and KITTEL, C. 1955. Phys. Rev. **98**, 368.
GIVENS, M. P. 1958. Solid state physics, Vol. 6 (Academic Press, Inc., New York) p. 313.
KAHN, A. H. and FREDERIKSE, A. H. P. R. 1959. Solid state physics, Vol. 9 (Academic Press, Inc , New York) p. 257.
KEYES, R. J., ZWERDLING, S., FONER, S., KOLM, H. H., and LAX, B. 1956. Phys. Rev. **104**, 1804.
LIN, C. J. 1959. Bull. Am. Phys. Soc. **4**, 227.
MITCHELL, E. W. J. 1955. Proc. Phys. Soc. B, **68**, 973.
RAU, R. R. and CASPARI, M. E. 1955. Phys. Rev. **100**, 632.
SOMMERFELD, A. 1954. Optics (Academic Press, Inc., New York).
STEPHEN, M. J. and LIDARD, A. B. 1959. J. Phys. Chem. Solids, **9**, 43.
STERN, E. A. and MYERS, R. D. 1958. Bull. Am. Phys. Soc. **3**, 416.
SUHL, H. and PEARSON, G. L. 1953. Phys. Rev. **92**, 858.

DIFFUSION PHENOMENA AND ISOTOPE EFFECTS IN THE EXTRACTION OF FISSION-PRODUCT XENON AND KRYPTON FROM IRRADIATED U_3O_8[1]

T. J. KENNETT AND H. G. THODE

ABSTRACT

An investigation of the diffusion of fission-product xenon and krypton from irradiated U_3O_8 powder as a function of temperature has revealed isotopic fractionation and also a double-valued activation energy. The apparent fission yields of Xe^{131} and Xe^{132} show abnormal enrichments of up to a factor of 10. These enrichments appear to be related to the precursor half-lives of xenon. When isotopic fractionation exists, the diffusion results exhibit an extremely low energy of activation.

INTRODUCTION

In the determination of fission yields using mass spectrometer techniques, it is frequently desirable to extract both the solid and gaseous fission products from the same sample. The fission gases may be extracted either by heating the irradiated samples at high temperatures, or by dissolving them completely. During a study of the fission yields of nuclides produced in the thermal fission of Pu^{239}, a sample of fission gas was obtained by simply heating an irradiated sample of finely divided plutonium oxide under conditions such that only part of the fission-product gas was recovered. The yields of the xenon isotopes observed for this sample were found to differ markedly from those obtained when the total fission gas was extracted by dissolution.

The fractionation of the xenon isotopes which occurred in the partial extraction of the fission gas was too large to be accounted for on the basis of simple diffusion theory applied to xenon gas. Also, the isotope effects for the various xenon isotopes were not mass dependent. This rather puzzling result, coupled with the growing interest in the use of oxides as potential fuel-element material, suggested a more complete study should be made of this effect.

Experiments were therefore designed to determine the xenon and krypton isotopic abundances in fission gas fractions extracted at various temperatures from neutron-irradiated U_3O_8 powders. From these experiments, the isotope effects could be followed and the diffusion activation energies determined. The results are reported below.

EXPERIMENTAL

Sample Preparation

To prepare uranium oxide, analytical grade uranyl nitrate was decomposed by heating in air to about 750° C. A chemical analysis showed the prepared material to be U_3O_8. After this heat treatment, the oxide was ground until it would pass a 250-mesh screen (30 micron particle radius). Samples of 2

[1]Manuscript received March 23, 1960.
Contribution from the Department of Physics, McMaster University, Hamilton, Ont.

grams were then transferred into cylindrical quartz vials having an inside diameter of 5.5 mm, an outside diameter of 7.5 mm, and a length of 25 mm. The quartz containers were evacuated, sealed under vacuum, and then placed into self-serve aluminum capsules for subsequent irradiation in the N.R.X. Reactor at Chalk River. Three samples were irradiated, one after the other, in the same self-serve position, for periods of 2.5, 5, and 10 days. The neutron flux at this position was about 8.6×10^{12} neutrons cm^{-2} sec^{-1}.

A portion of the uranium oxide was separated by means of a sedimentary tube in order to determine the particle size distribution. This measurement indicated that the most probable radius was in the range of from 10 to 30 microns.

Rare Gas Extraction

Following the irradiation, the samples were stored for 2 months to permit the decay of the major activities. At the end of this period, the quartz vials were placed into high-vacuum lines similar to that shown in Fig. 1. The system

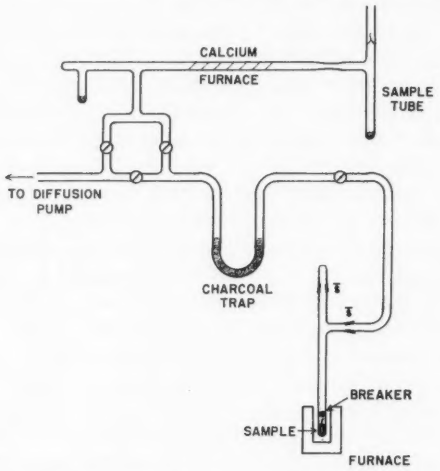

FIG. 1. A schematic representation of the system used to extract the fission-product rare gases at various temperatures.

was thoroughly evacuated before the vial was opened. With the vial opened, the system was connected to the vacuum pumps through a charcoal trap held at liquid air temperature. Such an arrangement ensures collection of any fission-product krypton and xenon released from the sample. A furnace which had been thermally calibrated surrounded the sample region. The sample was raised through a series of temperatures, remaining at each value for 3 hours. The rare gases liberated at each temperature plateau were collected and transferred to a calcium furnace for purification. The purified gas was then collected into a sample tube and removed from the line for subsequent mass spectrometric analysis.

Mass Spectrometry

The isotopic analysis of the rare gas samples was performed with a 10-in. directional-focussing mass spectrometer which employed an electron multiplier for the detector. The resolving power of the instrument was 650 which is sufficiently high to permit the separation of the rare gas isotopes from their respective isobaric hydrocarbon impurities. At high sensitivities these hydrocarbons are always present within the mass spectrometer tube itself and would mask small rare gas samples if a lower resolution were used. The isotopic abundances of normal krypton and xenon were found to agree within $\frac{1}{2}\%$ with the accepted values given by Nier (1950). The over-all sensitivity of the instrument permits the analyses of gas samples having a volume of 5×10^{-9} cc at N.T.P.

RESULTS

Isotopic Effects

The isotopic abundances and the corresponding volumes of the fission-product rare gases were accurately determined for each temperature plateau and an estimate was made of the corresponding volume of released gas. The irradiation conditions and the xenon abundances for the three U_3O_8 samples are given in Table I. Ten spectrograms were obtained for each sample at every

TABLE I

The abundance of fission-product xenon evolved from U_3O_8 as a function of temperature

Temperature plateau, °C	Isotopic abundance											
	Sample 1, irradiated 2.5 days				Sample 2, irradiated 5 days				Sample 3, irradiated 10 days			
	131	132	134	136	131	132	134	136	131	132	134	136
30	0.29	0.49	0.76	1.02	0.39	0.60	0.97	1.08	0.53	0.71	1.00	1.12
150	1.70	0.76	0.80	1.02	2.50	0.83	1.00	1.08	3.68	1.27	1.03	1.12
300	2.69	1.02	0.87	1.02	2.55	1.41	1.03	1.08	2.04	1.31	1.02	1.12
500	0.65	0.84	0.99	1.02	0.76	0.90	1.02	1.08	0.52	0.74	1.01	1.12
800	0.38	0.59	1.00	1.02	0.38	0.58	1.01	1.08	0.38	0.58	1.01	1.12
1200	0.36	0.55	1.00	1.02	0.36	0.55	1.00	1.08	0.36	0.55	1.00	1.12
Expected abundances	0.36	0.55	1.00	1.02	0.36	0.55	1.00	1.08	0.36	0.55	1.00	1.12

NOTE: The error for all abundances is less than 2%. The recorded values have been normalized to Xe^{136}, with a value of 1.00 for the Xe^{136} yield. The recorded values all exceed this value because of the contribution from the reaction $Xe^{135}(n,\gamma)Xe^{136}$.

temperature plateau and resulted in a most probable error of less than 2% for the relative abundances. In each case, the observed abundances were normalized to Xe^{136}. It should be noted that the Xe^{136} yield changes for each sample because the $Xe^{135}(n,\gamma)Xe^{136}$ contribution is a function of the irradiation time. The abundances observed for samples extracted between 800° and 1200° C were found to be in excellent agreement with the U^{235} fission yields (Blades *et al.* 1956) for these isotopes. These samples contained the bulk of the fission gas and fractionation effects were not detectable. Normal xenon, which can be detected by the presence of Xe^{129}, was observed for the 30° C

fractions but it dropped rapidly to zero as the temperature was increased. This indicates that a small amount of normal xenon was adsorbed on the surface of the U_3O_8 particles during the preparation of the samples.

The data tabulated in Table I show effects which would not be expected a priori. The Xe^{131} and Xe^{132} abundances do not remain constant relative to Xe^{136} but show remarkably high enrichments in the gas fractions extracted at 150, 300, and 500° C. For example, the Xe^{131} abundance for sample 3 is enriched by a factor of 10 while that for Xe^{132} by a factor of 2.4 in this temperature plateau. With the exception of sample 1, the abundance of Xe^{134} remains constant within the experimental error for all temperatures. These effects are most clearly seen in the graphical presentation given in Fig. 2 where the

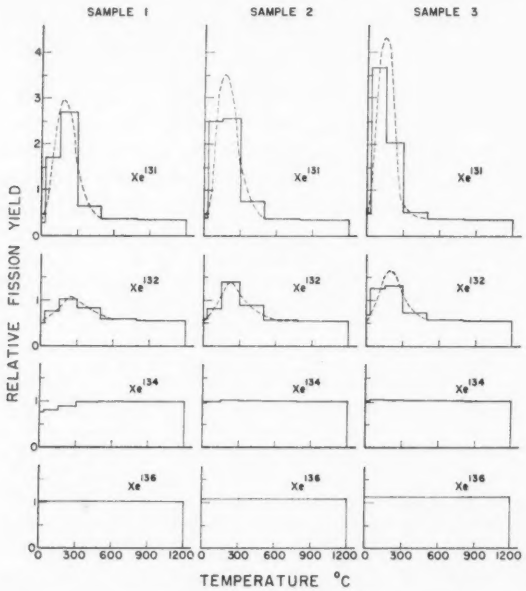

FIG. 2. Histograms showing the observed fission yields as a function of extraction temperature for the three samples studied. The true or expected fission yield is always observed at 1200° C. The dashed curves indicate the Maxwellian distribution which best fits the enrichment factor.

observed abundance is plotted as a function of temperature. It should be noted that the abundances observed in the region from 800° to 1200° C are identical with the accepted values for U^{235}, indicating no detectable isotope fractionation.

The experimental results yield only a histogram and, therefore, it is convenient to find a smooth curve which gives the differential abundance at every temperature within the interval. An inspection of the histograms for Xe^{131} and Xe^{132} shown in Fig. 2 suggests that the enrichment factor can be most easily represented by a Maxwellian distribution. The Maxwellian parameters were

obtained by determining the area and first moment of the respective temperature-abundance histograms. The curves determined in this manner are shown by the dashed lines in Fig. 2. The fit is very good and suggests that even higher enrichments could be obtained by measuring the abundance of fission gases released within smaller temperature intervals.

The krypton isotopes released from the U_3O_8 samples at different temperatures showed no deviation from their normal fission pattern. Because krypton is more abundant in nature and less abundant in fission than xenon, it was impossible to make meaningful measurements of the fission-product contribution in the low temperature fractions. Reliable measurements of isotopic abundance could only be made from 500° to 1200° C where the normal krypton contamination is small compared with the fission-product krypton. Therefore, it can be concluded that 500° C is too high a temperature to observe any appreciable krypton fractionation, if, indeed, such an effect does exist for the krypton isotopes.

The cumulative volume of gas released up to and including each temperature plateau is recorded in Table II. These values have been normalized to the total

TABLE II

The cumulative volume of rare gas evolved for 3-hour heating periods

	Temperature, °C					
	30	150	300	500	800	1200
Total xenon	2×10^{-4}	4×10^{-4}	7×10^{-4}	5×10^{-3}	0.13	1.00*
Total krypton			1×10^{-4}	5×10^{-3}	0.12	1.00*

*All the fission-product rare gas is assumed to escape when the U_3O_8 is maintained at 1200° C for 3 hours. The values recorded represent an average of the three samples investigated. The *total* volume of fission gas produced in sample 2, is calculated to be 6.3×10^{-4} cc for xenon and 1×10^{-4} cc for krypton (both at N.T.P.).

volume of gas which is assumed to have escaped by the time the U_3O_8 powder has been maintained at a temperature of 1200° C for a 3-hour period. This assumption appears valid since the measured volume at 1200° C was in good agreement with the volume calculated from the known sample size and irradiation conditions. The values quoted represent the average of the three samples for all isotopes. These data show that the abnormal xenon enrichments involve only about 0.5% of the total volume and also that from 500° to 1200° C the xenon and krypton diffuse at the same rate.

The results given in Tables I and II permit one to determine the cumulative abundances, i.e., the abundances which would be observed if all the gas released up to temperature T was collected and examined. Such a calculation was carried out and the results are given in Table III. It is interesting to note that even up to 800° C a 5 to 50% enrichment prevails in the Xe^{131} and Xe^{132} abundances.

To obtain more complete information about the enrichment mechanism, a subsidiary experiment was conducted. For this experiment, samples of U_3O_8 were prepared in a manner described previously; however, only particles

TABLE III

The cumulative abundance of fission-product xenon evolved from U_3O_8 as a function of temperature

Temperature plateau, °C	Isotopic abundance											
	Sample 1				Sample 2				Sample 3			
	131	132	134	136	131	132	134	136	131	132	134	136
30	0.29	0.49	0.76	1.02	0.39	0.60	0.97	1.08	0.53	0.71	1.00	1.12
150	0.40	0.51	0.76	1.02	0.51	0.69	0.99	1.08	1.29	0.83	0.98	1.12
300	0.84	0.61	0.78	1.02	1.63	1.09	1.01	1.08	1.70	1.09	1.01	1.12
500	0.81	0.65	0.82	1.02	0.85	0.92	1.02	1.08	0.67	0.78	1.01	1.12
800	0.53	0.61	0.94	1.02	0.41	0.61	1.01	1.08	0.38	0.58	1.01	1.12
1200	0.36	0.55	1.00	1.02	0.36	0.55	1.00	1.08	0.36	0.55	1.00	1.12

NOTE: The error for all abundances is less than 3%. The recorded values have been normalized to Xe^{136}.

having radii from 10 to 30 microns were used. This particle-size selection was achieved by the use of a sedimentary tube. The selected U_3O_8 was then uniformly distributed within a powdered-sulphur matrix in order to provide a trap for any fission fragments recoiling from the uranium particles. Two such samples were then irradiated at a low neutron flux to avoid melting the sulphur. In one sample, the rare gases trapped within the sulphur were removed by subliming the sulphur from the mixture under vacuum. The solid fission products of the second sample were obtained by treating the mixture with a CS_2+H_2O system and extracting from the water phase. In both cases, at least 10% of the fission products were found to be in the sulphur matrix. The isotopic abundances of the fission-product krypton, xenon, cesium, and neodymium from the sulphur matrix were determined. The krypton and neodymium did not deviate more than 10% from their "true" fission yields; however, the xenon and cesium yields, which are given in Table IV, showed

TABLE IV

The relative quantities* of xenon and cesium appearing in a sulphur matrix

	Mass number						
	131	132	133	134	135	136	137
Xenon ratio	3.7	2.6		1.0†		1.0	
Cesium ratio			1.0†		1.1		1.7

*For a "normal case" the recorded value would be 1.0.
†Cs^{133} and Xe^{134} have been normalized to 1.0.

marked enrichments. The results presented in Table IV are the ratios (observed yield)/(true yield) with a renormalization of the Xe^{134} and Cs^{133} ratios equal to 1.0. With such a representation of the data, a value of 1.0 will be obtained if no enrichment is present. Since cesium is monoisotopic (viz., Cs^{133}), only a lower limit for the normal cesium contamination can be given. Therefore, the Cs^{135} and Cs^{137} ratios represent only lower limits since they are measured relative to Cs^{133} which has been assumed to be entirely radiogenic. The sulphur experiment reveals a xenon fractionation not unlike that

for U_3O_8 and, in addition, discloses a similar effect for cesium. The data also indicate that no major isotope enrichment occurs in the krypton and neodymium mass regions.

Diffusion Effects

The properties of the gross diffusion process, whereby the rare gases are released from the U_3O_8 particles, can be ascertained by rather simple considerations. Since the U_3O_8 particles are approaching sphericity, the problem can be reduced to one of diffusion from a sphere. To obtain a solution to the problem, the diffusion equation

$$\partial C/\partial t = D\nabla^2 C, \tag{1}$$

must be solved with the boundary conditions,

(i) uniform initial concentration at time $t = 0$,
(ii) zero surface concentration for $t > 0$.

The solution of equation (1) under these conditions is

$$C(r, t) = -2C_0 \sum_{n=1}^{\infty} (-1)^n \frac{R}{n\pi r} \exp\left(\frac{-n^2\pi^2 Dt}{R^2}\right) \sin\frac{n\pi r}{R}, \tag{2}$$

where R is the particle radius and C_0 the initial concentration. The quantity of gas liberated in time t_0, Q_{t_0}, is given by

$$Q_{t_0} = -4\pi R^2 \int_0^{t_0} D(\nabla C)\, dt\,. \tag{3}$$

Defining F_{t_0} to be the fraction of the total gas released in time t_0 we can write

$$F_{t_0} = \frac{Q_{t_0}}{C_0 V} = 1 - \frac{6}{\pi^2} \sum_{n=1}^{\infty} \frac{1}{n^2} \exp\left(\frac{-n^2\pi^2 Dt_0}{R^2}\right), \tag{4}$$

where V is the particle volume. For small values of Dt_0/R^2, i.e., 10^{-3}, equation (4) reduces to

$$F_{t_0} = \frac{6}{\sqrt{\pi}} \left[\frac{Dt_0}{R^2}\right]^{1/2}. \tag{5}$$

By solving either equation (4) or (5) in the appropriate regions, F_{t_0} can be obtained as a function of the parameter Dt_0/R^2. Table II gives experimental F_{t_0} values, therefore, by means of this calculation, the corresponding Dt_0/R^2 value can be determined. The results of this computation are given in Table V where the parameter Dt_0/R^2 is given for each temperature plateau studied.

If the diffusion process can be described by an equation of the form

$$D = D_0 \exp(-U/NkT), \tag{6}$$

then by plotting $\ln(Dt_0/R^2)$* against the inverse temperature T^{-1}, a straight line should result, the slope of which is the activation energy U. A graph of

*The term Dt_0/R^2 can be written as αD since t_0 and R are constant throughout the experiment.

TABLE V

The diffusion parameter Dt_0/R^2 as a function of temperature for the fission-product rare gas and U_3O_8 system

Temperature, °C	Xenon		Krypton	
	F_{t_0}*	Dt_0/R^2	F_{t_0}	Dt_0/R^2
30	2×10^{-4}	3.5×10^{-9}		
150	4×10^{-4}	1.4×10^{-8}		
300	7×10^{-4}	4.3×10^{-8}	1×10^{-4}	8.7×10^{-10}
500	5×10^{-3}	2.2×10^{-6}	5×10^{-3}	2.2×10^{-3}
800	0.13	1.8×10^{-3}	0.12	1.8×10^{-3}
1200	1.00	6.0×10^{-1}	1.00	6.0×10^{-1}

*The quantity F_{t_0} represents the fraction of the total gas released after a time t_0 at a given temperature T. For the calculations in this table it has been assumed that had the sample been heated initially to temperature T, all the gas released at lower temperatures would be evolved at temperature T. Presumably the correct value to use would lie between the integral and differential quantities evolved. However, since the two limiting cases make no significant change in the results, the former assumption has been retained.

the data plotted in this manner is shown in Fig. 3. It is immediately apparent from Fig. 3 that two activation energies exist and also that the process can be satisfactorily described by equations of the form given in equation (6). At

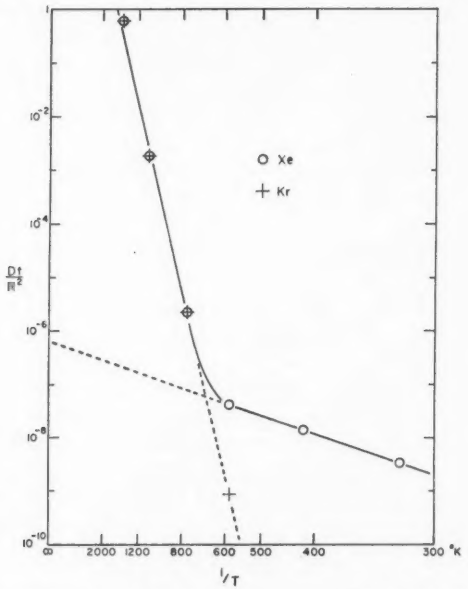

FIG. 3. The relationship found for the diffusion constant D and $1/T$. The dimensionless quantity Dt_0/R^2 is proportional to D since t_0/R^2 remained constant throughout the experiment. The existence of two activation energies is indicated by the different slopes found above and below 600° K.

temperatures below 410° C the predominant term has an activation energy of 3000 cal mole^{-1} (0.13 ev) while that above 410° C has a value of 39,000 cal mole^{-1} (1.7 ev). This effect appears to hold only for xenon since the krypton activation energy remains at 39,000 cal mole^{-1} over the region studied. The curve in Fig. 3 can be described by the equation

$$(7)\quad D = D_0 \exp(-39{,}000/NkT) + D_0' \exp(-3000/NkT)$$
$$= R^2/t_0\{1.6\times10^5 \exp(-39{,}000/NkT) + 6.7\times10^{-7} \exp(-3000/NkT)\}.$$

Since $t_0 = 1.08\times10^4$ sec and R lies between 10 and 30 microns, the value of the frequency factors D_0 and D_0' can be calculated. When this is done, the results are $D_0 = 7.4\times10^{-5\pm0.6}$ cm^2 sec^{-1} and $D_0' = 3.1\times10^{-16\pm0.6}$ cm^2 sec^{-1}. The errors in the exponent represent the spread in the radius of the particles. It is interesting that the fractionation was observed for gas samples extracted below 500° C which is precisely where the low activation process is prevalent.

DISCUSSION OF RESULTS

The most striking feature of this investigation has been the large isotope effect found for Xe^{131} and Xe^{132} and the association of this with an extremely low activation energy. It is rather early to propose a mechanism for this effect; however, several interesting features are revealed by the data.

In connection with isotopic effects for rare gases, we have noted that there is little or no fractionation apparent among the krypton isotopes or for Xe^{134} and Xe^{136}. These isotopes, which exhibit little or no fractionation, all share the common property of having short-lived precursors. In marked contrast to this, Xe^{131} and Xe^{132} have relatively long-lived precursors

$$(Te^{131} \xrightarrow{25\text{ months}} I^{131} \xrightarrow{8.1\text{ days}} Xe^{131},\ Te^{132} \xrightarrow{77\text{ hours}} I^{132} \xrightarrow{2.3\text{ hours}} Xe^{132}).$$

This apparent correlation of fractionation with precursor half-life suggests the diffusion properties and concentration distributions of tellurium and iodine are quite different from those of xenon. Another possibility is that the fractionation is related to the recoil range of the fission fragments. This seems rather unlikely, on the basis of our knowledge of recoil ranges (Finkle *et al.* 1951). Also, for the case of U_3O_8 powder, the initial distribution of the fission products is expected to be isotropic regardless of the range except for the boundary between the powder and the quartz container.

If we consider only the correlation of fractionation and half-life, then it would appear that there is a tendency for tellurium and iodine to concentrate on the surface of the U_3O_8 particles to a greater extent than for xenon. When the iodine decays, there is an enrichment of Xe^{131} and Xe^{132} at the surface or at grain boundaries. One then expects a large enrichment and a low activation energy to be associated with these isotopes.

The results of the sulphur matrix experiment depends upon recoil ranges and surface concentrations. If we restrict ourselves to the latter, then interface diffusion of tellurium and iodine and the recoil of xenon following β decay may possibly account for the isotopic distribution found in the sulphur matrix.

The cesium yields associated with the sulphur fraction also exhibit isotopic effects. Here one finds that the cesium enrichment increases with decreasing half-life of the xenon precursor. This suggests that cesium, iodine, and tellurium all behave in a similar manner at the surface of the U_3O_8 particles and all behave quite differently from xenon. The xenon appears to have a relatively low mobility and does not concentrate on the surface or at grain boundaries of the particles.

Although the diffusion data obtained in the course of this work are qualitative in nature, they do, however, suggest the following interesting features. The apparent existence of two activation energies can be associated with the observed isotopic effects. The activation energy below 600° K depends upon the particular isotope studied, while above this temperature, all the xenon and krypton isotopes have approximately the same value. Thus, below 600° K the apparent activation energy could be related to the precursor half-life of the xenon. The existence of this double value may possibly explain the wide range of activation energies found in the literature (Stubbs *et al.* 1957; Lindner and Matzke 1959).

The results obtained in this work have suggested many avenues of investigation which should be explored if a complete understanding of the observed effects is to be achieved. With this in mind, an active program has been initiated and results should be shortly forthcoming.

ACKNOWLEDGMENTS

The authors are grateful to the National Research Council of Canada for providing the financial support of this work. They also wish to thank A.E.C.L. for providing irradiation facilities.

REFERENCES

Blades, A. F., Fleming, W. F., and Thode, G. H. 1956. Can. J. Chem. **34**, 233.
Finkle, B., Hoagland, E. J., Katcoff, S., and Sugarman, N. 1951. N.N.E.S. The fission products, Papers 45 and 46 (McGraw-Hill, Book Co., Inc., New York).
Lindner, von R. and Matzke, Hj. 1959. Z. Naturforsch. **14a**, 582.
Nier, A. O. 1950. Phys. Rev. **79**, 450.
Stubbs, F. J., Walton, G. N., and Silver, P. J. 1957. Atomic Energy Research Establ. (Gt. Britain), C/R 2176.

INTENSITIES IN Σ–Δ AND Π–Δ TRANSITIONS OF DIATOMIC MOLECULES[1]

I. Kovács

ABSTRACT

Explicit expressions are obtained for the intensity distribution in the branches of $^1\Sigma$–$^3\Delta$, $^3\Sigma$–$^3\Delta$, and $^1\Pi$–$^3\Delta$ bands. They are valid with satisfactory accuracy for any value of the coupling constant of the $^3\Delta$ state.

Theoretical investigations of intensities in electronic bands have hitherto mostly dealt with transitions in which the orbital angular momentum remains unchanged or changes by ± 1. To be sure, some authors have extended their investigations also to other cases but these are of very special kinds (Schlapp 1932; Van Vleck 1934). Recent experimental data (Herzberg 1959), however, make necessary the study of further cases particularly of transitions between Σ and Δ states of the same and of different multiplicity. In the present paper the $^1\Sigma$–$^3\Delta$, $^3\Sigma$–$^3\Delta$, and $^1\Pi$–$^3\Delta$ transitions are considered.

It is well known that if the spin–orbit interaction is neglected, the electronic part of the wave function of any state of the molecule can be separated into the product of two factors, one depending on the orbital motions, and the other on the electron spins. On account of spin–orbit interaction the wave functions are modified and, as a result, the above-mentioned transitions are permitted with small intensity.

Let us denote the electronic parts of the wave functions of the individual components of the Σ, Π, Δ . . . states, neglecting the spin–orbit interaction to a first approximation, by the symbols $\phi_0(^1\Sigma_\Omega)$, $\phi_0(^3\Sigma_\Omega)$, $\phi_0(^1\Pi_\Omega)$ . . . etc.* Then, taking into account the spin–orbit interaction, the perturbed wave functions will be linear combinations of the unperturbed wave functions of the same Ω and of multiplicities 1 or 3. From the properties of the operators $\mathbf{l}$ and $\mathbf{s}$ it is readily verified that the spin–orbit interaction joins terms for which $\Delta\Lambda = 0$, ± 1, $\Delta S = 0$, ± 1, and $\Delta\Omega = 0$. One of the perturbed wave functions is the following:

$$(1) \qquad \phi(^3\Delta_{+2}) = a\phi_0(^3\Delta_{+2}) + l_1\phi_0(^3\Pi_{+2}) + l_2\phi_0(^3\phi_{+2}) + l_3\phi_0(^1\Delta_{+2})$$

where a is a constant of order unity, and l_1, l_2, l_3† are constants much less than unity if, as we shall suppose, the spin–orbit interaction is small.

Taking account of the degeneracy of the states which differ only by the orientation of the resultant Ω relative to the axis of the molecule ($+\Omega$ and $-\Omega$) and completing the wave functions by the parts arising from the rotations and vibrations of the nuclei, the new wave functions will be the following:

[1]Manuscript received March 31, 1960.
Contribution from the Department of Atomic Physics, Polytechnical University, Budapest, Hungary.

*For the explicit form of these wave functions, see, for example, Kovács (1958).

†These have a form similar to the factors inside the parentheses of eq. (5).

$$
\begin{aligned}
\psi\,(^1\Sigma_0^{\pm}) &= \phi(^1\Sigma_0^{\pm})Ru_{J,0,M}\\
\psi_a(^3\Sigma_1^{\pm}) &= \frac{1}{\sqrt{2}}\,[\phi(^3\Sigma_{+1}^{\pm})u_{J,+1,M}+\phi(^3\Sigma_{-1}^{\pm})u_{J,-1,M}]R\\
\psi_a(^3\Sigma_1^{\pm})' &= \frac{1}{\sqrt{2}}\,[\phi(^3\Sigma_{+1}^{\pm})u_{J,+1,M}-\phi(^3\Sigma_{-1}^{\pm})u_{J,-1,M}]R\\
\psi_a(^3\Sigma_0^{\pm}) &= \phi(^3\Sigma_0^{\pm})Ru_{J,0,M}\\
\psi\,(^1\Pi_1) &= \frac{1}{\sqrt{2}}\,[\phi(^1\Pi_{+1})u_{J,+1,M}\pm\phi(^1\Pi'_{-1})u_{J,-1,M}]R\\
\psi_a(^3\Delta_\Omega) &= \frac{1}{\sqrt{2}}\,[\phi(^3\Delta_{+\Omega})u_{J,+\Omega,M}\pm\phi(^3\Delta'_{-\Omega})u_{J,-\Omega,M}]R \qquad (\Omega = 3,2,1)
\end{aligned}
\tag{2}
$$

where R and u are the vibrational and rotational wave functions of the molecule. Since we are concerned with a definite vibrational level of each of the two states in question, the vibrational part of the wave function merely introduces into the intensities a factor independent of J and will therefore be omitted in what follows. The task of theory is the calculation of the so-called i factors for all branches occurring in the rotational transitions. For this the expressions for the matrix elements of the components of the electric moment of the molecule

$$
z_a(X_\Omega, {}^3\Delta_{\Omega'}) = \int \psi_a^*(X_\Omega) z\, \psi_a\,(^3\Delta_{\Omega'})d\tau \tag{3}
$$

are used, where $X = {}^1\Sigma$, ${}^3\Sigma$, and ${}^1\Pi$. If we remember that $z = \eta \sin\nu + \xi\cos\nu$ where ν is the angle between the ξ-axis and a preferential direction in space, taken as the z-axis, we may write the following explicit expressions for the amplitudes

$$
z_a(^1\Sigma_0^{\pm}J';{}^3\Delta_1,J'') = \frac{1}{\sqrt{2}}\,[1\pm(-1)^{\Delta J+\Sigma}]D_1 f_{J',0,M;J'',-1,M} \tag{4a}
$$

$$
\begin{cases}
z_a(^3\Sigma_1^{\pm}J';{}^3\Delta_2,J'') = \tfrac{1}{2}[1\mp(-1)^{\Delta J+\Sigma}]\,D_2 f_{J',-1,M;J'',-2,M}\\
z_a(^3\Sigma_1^{\pm\prime}J';{}^3\Delta_2,J'') = \tfrac{1}{2}[1\pm(-1)^{\Delta J+\Sigma}]\,D_2 f_{J',-1,M;J'',-2,M}\\
z_a(^3\Sigma_0^{\pm}J';{}^3\Delta_1,J'') = \dfrac{1}{\sqrt{2}}[1\mp(-1)^{\Delta J+\Sigma}]D_2 f_{J',0,M,J'',-1,M}
\end{cases} \tag{4b}
$$

$$
\begin{cases}
z_a(^1\Pi_1,J';{}^3\Delta_2,J'') = D_3 f_{J',-1,M;J'',-2,M}\\
z_a(^1\Pi_1,J';{}^3\Delta_1,J'') = D_4 f_{J',-1,M;J'',-1,M}
\end{cases} \tag{4c}
$$

where the exponent $\Delta J = |J'-J''|$ takes the values 1 in case of the P and R branches and 0 in case of the Q branch and Σ is equal to 0 or 1, according to whether we are dealing with Σ^+ or Σ^- states. The constants D are independent of J, for example D_1 is given by the following expression:

$$
\begin{aligned}
D_1 = {} & \left(\frac{\int \phi_0^*(^1\Pi'_{-1})\Sigma a_t(l_t s_t)\,\phi_0(^3\Delta'_{-1})d\tau}{W(^1\Pi'_{-1})-W(^3\Delta'_{-1})}\right)\int \phi_0^*(^1\Sigma_0^{\pm})\eta\phi_0(^1\Pi'_{-1})d\tau\\
& + \left(\frac{\int \phi_0^*(^3\Pi'_0)\Sigma a_t(l_t s_t)\,\phi_0(^1\Sigma_0^{\pm})d\tau}{W(^3\Pi'_0)-W(^1\Sigma_0^{+})}\right)^*\int \phi_0^*(^3\Pi'_0)\eta\phi_0(^3\Delta'_{-1})d\tau.
\end{aligned}
\tag{5}
$$

TABLE 1

Intensity formulae for $^3\Delta \leftrightarrow {}^1\Sigma$ band

Branches		i-factors		
$^1\Sigma \rightarrow {}^3\Delta$	$^3\Delta \rightarrow {}^1\Sigma$	$^3\Delta(a)$	Intermediate case	$^3\Delta(b)$
$^OP(J)$	$^SR(J-1)$	0	$\frac{(J-1)(J+1)(J+2)[u_3-(Y-2)]^2}{C_3(J)}$	$\frac{(J+2)(J+3)}{2J+1}$
$^PQ(J)$	$^RQ(J)$	0	$\frac{(2J+1)(J-1)(J+2)[u_3-(Y-2)]^2}{C_3(J)}$	$\frac{(J+2)(J+3)}{J+1}$
$^QR(J)$	$^QP(J+1)$	0	$\frac{(J-1)J(J+2)[u_3-(Y-2)]^2}{C_3(J)}$	$\frac{J(J+2)(J+3)}{(2J+1)(J+1)}$
$P(J)$	$R(J-1)$	0	$\frac{(J-1)(J+1)(J+2)}{C_2(J)}$	$\frac{(J-1)(J+2)}{J}$
$Q(J)$	$Q(J)$	0	$\frac{(2J+1)(J-1)(J+2)}{C_2(J)}$	$\frac{(2J+1)(J-1)(J+2)}{J(J+1)}$
$R(J)$	$P(J+1)$	0	$\frac{(J-1)J(J+2)}{C_2(J)}$	$\frac{(J-1)(J+2)}{J+1}$
$^QP(J)$	$^QR(J-1)$	$2(J+1)$	$\frac{(J-1)(J+1)(J+2)[u_1+(Y-2)]^2}{C_1(J)}$	$\frac{(J-2)(J-1)(J+1)}{(2J+1)J}$
$^RQ(J)$	$^PQ(J)$	$2(2J+1)$	$\frac{(2J+1)(J-1)(J+2)[u_1+(Y-2)]^2}{C_1(J)}$	$\frac{(J-2)(J-1)}{J}$
$^SR(J)$	$^OP(J+1)$	$2J$	$\frac{(J-1)J(J+2)[u_1+(Y-2)]^2}{C_1(J)}$	$\frac{(J-2)(J-1)}{2J+1}$

TABLE II

Intensity formulae for $^3\Sigma \leftrightarrow {}^3\Delta$ band

Branches		i-factors		
$^3\Sigma$-$^3\Delta$	$^3\Delta$-$^3\Sigma$	$^3\Delta(a)$	Intermediate case	$^3\Delta(b)$
$P_1(J)$	$R_1(J-1)$	$\frac{2(J-1)(J+1)}{2J-1}$	$\frac{(J+1)(J+2)[(J-1)(u_1+Y-2)+(J-2)(J+2)]^2}{(2J-1)C_1(J)}$	$\frac{(2J+1)(J-2)(J+1)}{(2J-1)J}$
$Q_1(J)$	$Q_1(J)$	$2J$	$\frac{(J-1)(J+2)[J(u_1+Y-2)+(J-2)(J+2)]^2}{J\,.\,C_1(J)}$	$\frac{4(J-2)(J-1)(J+1)^2}{(2J+1)\,.\,J^2}$
$R_1(J)$	$P_1(J+1)$	$\frac{2J(J+1)}{2J+3}$	$\frac{(J-1)J(J+2)[(J+1)(u_1+Y-2)+(J-2)(J+2)]^2}{(2J+3)(J+1)C_1(J)}$	$\frac{(2J+3)(J-2)(J-1)}{(2J+1)(J+1)}$
$^QP_{21}(J)$	$^QR_{12}(J-1)$	0	$\frac{(J-2)^2(J+1)(J+2)^2}{J\,.\,C_1(J)}$	$\frac{(J-2)(J+1)(J+2)^2}{(2J+1)J^2}$
$^RQ_{21}(J)$	$^PQ_{12}(J)$	0	$\frac{(2J+1)(J-2)^2(J-1)(J+2)^2}{J(J+1)\,.\,C_1(J)}$	$\frac{(J-2)(J-1)(J+2)^2}{J^2(J+1)}$
$^SR_{21}(J)$	$^OP_{12}(J+1)$	0	$\frac{(J-2)^2(J-1)J(J+2)^2}{(J+1)C_1(J)}$	$\frac{(J-2)(J-1)(J+2)}{(2J+1)(J+1)}$
$^RP_{21}(J)$	$^PR_{12}(J-1)$	$\frac{2J(J+1)}{2J-1}$	$\frac{(J-1)(J+1)(J+2)[J(u_1+Y-2)-(J-2)(J+2)]^2}{(2J-1)J\,.\,C_1(J)}$	$\frac{4(J-2)(J-1)(J+1)}{(2J-1)(2J+1)J^2}$
$^SQ_{21}(J)$	$^OQ_{12}(J)$	$2(J+1)$	$\frac{(J-1)(J+2)[(J+1)(u_1+Y-2)-(J-2)(J+2)]^2}{(J+1)C_1(J)}$	$\frac{(J-2)(J-1)}{(2J+1)J(J+1)}$
$^TR_{21}(J)$	$^NP_{12}(J+1)$	$\frac{2J(J+2)}{2J+3}$	$\frac{(J-1)J(J+2)^2[u_1+Y-J]^2}{(2J+3)C_1(J)}$	0
$^OP_{12}(J)$	$^SR_{21}(J-1)$	$\frac{(J+1)(J+2)}{2J-1}$	$\frac{(J+1)(J+2)(J+1-Y)^2}{(2J-1)C_2(J)}$	$\frac{(J+1)^2(J+2)}{(2J-1)\,.\,J}$
$^PQ_{12}(J)$	$^RQ_{21}(J)$	$\frac{(J-1)(J+2)}{J}$	$\frac{(J-1)(J+2)(J+2-Y)^2}{J\,.\,C_2(J)}$	$\frac{(J-1)(J+2)^2}{(J+1)\,.\,J^2}$
$^QR_{12}(J)$	$^QP_{21}(J+1)$	$\frac{(J-1)J(J+2)}{(2J+3)(J+1)}$	$\frac{(J-1)J(J+2)(J+3-Y)^2}{(2J+3)(J+1)C_2(J)}$	$\frac{(J-1)(J+2)(J+3)^2}{(2J+3)(J+1)^2}$

TABLE II *(Concluded)*

$P_3(J)$	$R_1(J-1)$	$\frac{(J+1)(J+2)}{J}$	$\frac{(J+1)(J+2)(Y-2)^2}{J\,.\,C_2(J)}$	$\frac{4(J+2)}{J^2}$
$Q_3(J)$	$Q_1(J)$	$\frac{(2J+1)(J-1)(J+2)}{J(J+1)}$	$\frac{(2J+1)(J-1)(J+2)(Y-2)^2}{J(J+1)C_2(J)}$	$\frac{4(2J+1)(J-1)(J+2)}{J^2(J+1)^2}$
$R_3(J)$	$P_1(J+1)$	$\frac{(J-1)J}{J+1}$	$\frac{(J-1)J(Y-2)^2}{(J+1)C_2(J)}$	$\frac{4(J-1)}{(J+1)^2}$
${}^{Q}P_{33}(J)$	${}^{Q}R_{33}(J-1)$	$\frac{(J-1)(J+1)(J+2)}{(2J-1)J}$	$\frac{(J-1)(J+1)(J+2)(J-2+Y)^2}{J(2J-1)C_2(J)}$	$\frac{(J-2)^2(J-1)(J+2)}{(2J-1)J^2}$
${}^{R}Q_{33}(J)$	${}^{P}Q_{33}(J)$	$\frac{(J-1)(J+2)}{J+1}$	$\frac{(J-1)(J+2)(J-1+Y)^2}{(J+1)C_2(J)}$	$\frac{(J-1)^3(J+2)}{J\,.\,(J+1)^2}$
${}^{R}R_{33}(J)$	${}^{O}P_{33}(J+1)$	$\frac{(J-1)J}{2J+3}$	$\frac{(J-1)J(J+Y)^2}{(2J+3)C_2(J)}$	$\frac{J^2(J-1)}{(2J+3)(J+1)}$
${}^{N}P_{13}(J)$	${}^{T}R_{31}(J-1)$	0	$\frac{(J-1)^2(J+1)(J+2)[u_3-Y-(J+1)]^2}{(2J-1)C_2(J)}$	0
${}^{O}Q_{13}(J)$	${}^{S}Q_{31}(J)$	0	$\frac{(J-1)(J+2)[J(u_3-(Y-2))-(J-1)(J+3)]^2}{J\,.\,C_2(J)}$	$\frac{(J+2)(J+3)}{(2J+1)J(J+1)}$
${}^{P}R_{13}(J)$	${}^{R}P_{31}(J+1)$	0	$\frac{(J-1)J(J+2)[(J+1)(u_3-(Y-2))-(J-2)(J+3)]^2}{(2J+3)(J+1)C_2(J)}$	$\frac{4J\,.\,(J+2)(J+3)}{(2J+1)(2J+3)(J+1)^2}$
${}^{O}P_{33}(J)$	${}^{S}R_{33}(J-1)$	0	$\frac{(J-1)^2(J+1)(J+2)(J+3)^2}{J\,.\,C_2(J)}$	$\frac{(J-1)(J+2)(J+3)}{(2J+1).J}$
${}^{P}Q_{33}(J)$	${}^{R}Q_{33}(J)$	0	$\frac{(2J+1)(J-1)^2(J+2)(J+3)^2}{J(J+1)C_2(J)}$	$\frac{(J-1)^2(J+2)(J+3)}{J(J+1)^2}$
${}^{Q}R_{33}(J)$	${}^{O}P_{33}(J+1)$	0	$\frac{(J-1)^2J(J+3)^2}{(J+1)\,.\,C_2(J)}$	$\frac{(J-1)^2J(J+3)}{(2J+1)(J+1)^2}$
$P_3(J)$	$R_1(J-1)$	0	$\frac{(J-1)(J+1)(J+2)[J(u_3-(Y-2))+(J-1)(J+3)]^2}{(2J-1)J\,.\,C_2(J)}$	$\frac{(2J-1)(J+2)(J+3)}{(2J+1)J}$
$Q_3(J)$	$Q_1(J)$	0	$\frac{(J-1)(J+2)[(J+1)(u_3-(Y-2))+(J-1)(J+3)]^2}{(J+1)C_2(J)}$	$\frac{4J^2(J+2)(J+3)}{(2J+1)(J+1)^3}$
$R_3(J)$	$P_1(J+1)$	0	$\frac{(J-1)J[(J+2)(u_3-(Y-2))+(J-1)(J+3)]^2}{(2J+3)C_2(J)}$	$\frac{(2J+1)J(J+3)}{(2J+3)(J+1)}$

TABLE III

Intensity formulae for $^1\Pi \leftrightarrow {}^3\Delta$ band

Branches		*i*-factors		
$^1\Pi$–$^3\Delta$	$^3\Delta$–$^1\Pi$	$^3\Delta(a)$	Intermediate case	$^3\Delta(b)$
${}_oP(J)$	${}^SR(J-1)$	0	$\frac{(J-1)^2(J+1)(J+2)[(u_3-Y+2)+\lambda(J+3)]^2}{2JC_3(J)}$	$\frac{(J-1)(J+2)(J+3)(\lambda+1)^2}{2(2J+1)J}$
${}^PQ(J)$	${}^RQ(J)$	0	$\frac{(2J+1)(J-1)(J+2)[(u_3-Y+2)+\lambda(J-1)(J+3)]^2}{2J(J+1)C_3(J)}$	$\frac{(J+2)(J+3)[1+\lambda(J-1)]^2}{2J(J+1)^2}$
${}^QR(J)$	${}^QP(J+1)$	0	$\frac{(J-1)J[(J+2)(u_3-Y+2)+\lambda(J-1)(J+3)]^2}{2(J+1)C_3(J)}$	$\frac{J(J+3)[(J+2)+\lambda(J-1)]^2}{2(2J+1)(J+1)^2}$
$P(J)$	$R(J-1)$	$\frac{(J+1)(J+2)}{J}$	$\frac{(J+1)(J+2)[(J-1)+\lambda(Y-2)]^2}{2J\,.\,C_2(J)}$	$\frac{(J+2)[(J-1)-2\lambda]^2}{2J^2}$
$Q(J)$	$Q(J)$	$\frac{(2J+1)(J-1)(J+2)}{J(J+1)}$	$\frac{(2J+1)(J-1)(J+2)[1+\lambda(Y-2)]^2}{2J(J+1)C_2(J)}$	$\frac{(2J+1)(J-1)(J+2)[1-2\lambda]^2}{2J^2(J+1)^2}$
$R(J)$	$P(J+1)$	$\frac{(J-1)J}{(J+1)}$	$\frac{(J-1)J[(J+2)+\lambda(Y-2)]^2}{2(J+1)C_2(J)}$	$\frac{(J-1)[(J+2)-2\lambda]^2}{2(J+1)^2}$
${}^QP(J)$	${}^QR(J-1)$	$\frac{(J-1)(J+1)}{J}$	$\frac{(J+1)(J+2)[(J-1)(u_1+Y-2)-\lambda(J-2)(J+2)]^2}{2JC_1(J)}$	$\frac{(J-2)(J+1)[(J-1)-\lambda(J+2)]^2}{2(2J+1)J^2}$
${}^RQ(J)$	${}^PQ(J)$	$\frac{2J+1}{J(J+1)}$	$\frac{(2J+1)(J-1)(J+2)[(u_1+Y-2)-\lambda(J-2)(J+2)]^2}{2J(J+1)C_1(J)}$	$\frac{(J-2)(J-1)[1-\lambda(J+2)]^2}{2J^2(J+1)}$
${}^SR(J)$	${}^OP(J+1)$	$\frac{J(J+2)}{J+1}$	$\frac{(J-1)J(J+2)^2[(u_1+Y-2)-\lambda(J-2)]^2}{2(J+1)C_1(J)}$	$\frac{(J-2)(J-1)(J+2)[1-\lambda]^2}{2(2J+1)(J+1)}$

While these constants determine the possibility of transitions between the above-mentioned states, we need not consider them for the problem of the intensity distribution except in case of the transition $^1\Pi$–$^3\Delta$, where two constants independent of each other occur, so that only one of these may be eliminated. The absolute values of the amplitudes are

$$(6) \qquad f_{J',\Omega',M;J'',\Omega'',M} = \left| \int u^*_{J',\Omega',M} u_{J'',\Omega'',M} \sin\nu \begin{matrix} \sin\nu \\ \cos\nu \end{matrix} d\nu d\omega \right| .$$

They may be found in a paper by Kronig (1927).

The squares of (4*a*) and (4*c*) multiplied by 3 and summed over the magnetic quantum numbers give the i factors referring to the transitions $^1\Sigma \leftrightarrow {}^3\Delta$ (*a*) and $^1\Pi \leftrightarrow {}^3\Delta$ (*a*) and these are to be found in the third column of Tables I and III.

However, multiplet Σ states always belong to Hund's case (*b*). Therefore for the $^3\Sigma$ state we introduce wave functions of the following form

$$\psi_b({}^3\Sigma^{\pm}_{J+1}) = -\sqrt{\frac{J+1}{2J+1}}\,\psi_a({}^3\Sigma^{\pm}_0) - \sqrt{\frac{J}{2J+1}}\,\psi_a({}^3\Sigma^{\pm}_1)$$

$$(7) \qquad \psi_b({}^3\Sigma^{\pm}_J) = \psi_a({}^3\Sigma^{\pm}_1)'$$

$$\psi_b({}^3\Sigma^{\pm}_{J-1}) = \sqrt{\frac{J}{2J+1}}\,\psi_a({}^3\Sigma^{\pm}_0) - \sqrt{\frac{J+1}{2J+1}}\,\psi_a({}^3\Sigma^{\pm}_1)$$

Hence the amplitudes become

$$(8) \qquad z({}^3\Sigma_N, {}^3\Delta_\Omega) = \int \psi_b^*({}^3\Sigma_N) z \psi_a({}^3\Delta_\Omega) d\tau,$$

where $N = J+1$, J, $J-1$ and $\Omega = 3, 2, 1$. Some of the i factors which can be obtained on the basis of (8) are listed in the third column of Table II.

The $^3\Delta$ states can in general be represented well by the formulae of Hund's case (*a*) only for small values of the rotational quantum numbers. With increasing rotational quantum numbers there is a transition toward case (*b*). The wave functions valid with a satisfactory accuracy for any value of the coupling constant $Y = A/B$ can then be represented by

$$(9) \qquad \psi({}^3\Delta_N) = \sum_{\Omega=3}^{1} S_{\Omega,N}(\Delta)\psi_a({}^3\Delta_\Omega)$$

where the transformation matrix elements $S_{\Omega,N}(\Delta)$ are the following:

$$S_{3,J+1} = \frac{\sqrt{(J-2)(J+3)}[u_3+Y-2]}{\sqrt{2C_3(J)}};\quad S_{2,J+1} = \frac{(J-1)(J+3)}{\sqrt{C_3(J)}};$$

$$S_{1,J+1} = \frac{\sqrt{(J-1)(J+2)}[u_3-Y+2]}{\sqrt{2C_3(J)}}$$

$$(10) \quad S_{3,J} = -\sqrt{\frac{(J-2)(J+3)}{2C_2(J)}};\ S_{2,J} = \frac{Y-2}{\sqrt{C_2(J)}};\ S_{1,J} = \sqrt{\frac{(J-1)(J+2)}{2C_2(J)}}$$

$$S_{3,J-1} = \frac{\sqrt{(J-2)(J+3)}[u_1-Y+2]}{\sqrt{2C_1(J)}};\quad S_{2,J-1} = -\frac{(J-2)(J+2)}{\sqrt{C_1(J)}};$$

$$S_{1,J-1} = \frac{\sqrt{(J-1)(J+2)}[u_1+Y-2]}{\sqrt{2C_1(J)}}.$$

Here for normal states (Y positive)

$$
\begin{aligned}
C_1(J) &= 2Y(Y-4)(J-1)(J+2)+(2J+1)(J-2)J(J+2)\\
C_2(J) &= Y(Y-4)+J(J+1)\\
C_3(J) &= 2Y(Y-4)(J-2)(J+3)+(2J+1)(J-1)(J+1)(J+3)\\
u_1 &= [Y(Y-4)+J^2]^{\frac{1}{2}}; \qquad u_3 = [Y(Y-4)+(J+1)^2]^{\frac{1}{2}}
\end{aligned}
\tag{11}
$$

while for inverted states (Y negative) the coefficient of $2Y(Y-4)$ in $C_1(J)$ is equal to $(J-2)(J+3)$ instead of $(J-1)(J+2)$; in $C_3(J)$ it is equal to $(J-1)(J+2)$ instead of $(J-2)(J+3)$.*

To obtain the i factors in the intermediate case between Hund's case (a) and (b) for the $^3\Delta$ term, the amplitudes must be written in the following form:

$$
z(X_{N'};\,{}^3\Delta_{N''}) = \int \psi_b^*(X_{N'})z\psi({}^3\Delta_{N''})d\tau \tag{12}
$$

where $X = {}^1\Sigma$, ${}^3\Sigma$, ${}^1\Pi$. From (12) the total intensities of the transitions ${}^1\Sigma^{\pm} \leftrightarrow {}^3\Delta$, ${}^3\Sigma^{\pm} \leftrightarrow {}^3\Delta$, and ${}^1\Pi \leftrightarrow {}^3\Delta$ can be calculated. These are to be found in the fourth column of Tables I, II, and III. In Table III the constant λ is given by $\sqrt{2}D_3/D_4$ (see (4c)). The expressions are valid for any value of the coupling constant and contain as special cases the expressions for the transitions

$$
X \leftrightarrow {}^3\Delta_{\text{norm}}(a), \quad X \leftrightarrow {}^3\Delta_{\text{inv}}(a), \quad X \leftrightarrow {}^3\Delta(b)
$$

when $Y = +\infty$, $-\infty$, 0. The expressions for the latter special case are given in the fifth column of Tables I, II, and III.† In the tables the $^3\Delta$ terms were assumed to be normal. In case of inverted terms $\Omega = 3$ corresponds not to the state $N = J+1$, but to $N = J-1$ and therefore for the transitions $X-{}^3\Delta(a)$ in the Table II the second indices 1, 2, 3 in the designation of the branches should be replaced by the designation 3, 2, 1 (for ${}^3\Delta(a)-X$ the first index) and in the Tables I and III it is necessary to interchange the branches ${}^OP$, ${}^PQ$, ${}^QR$ and ${}^QP$, ${}^RQ$, ${}^SR$.

Comparing the intensities of each of the branches of the transition ${}^3\Sigma$–${}^3\Delta$ with those of the corresponding branches of the transition ${}^3\Sigma$–${}^3\Pi$, it is found that for low rotational quantum numbers the intensities of the branches ${}^QP_{21}$, ${}^RQ_{21}$, ${}^SR_{21}$, ${}^NP_{13}$, ${}^OQ_{13}$, ${}^PR_{13}$, ${}^OP_{23}$, ${}^PQ_{23}$, ${}^QR_{23}$, P_3, Q_3, R_3‡ are smaller, those of the branches P_2, Q_2, R_2 are greater whilst for high rotational quantum numbers the intensities of the branches P_2, Q_2, R_2 are smaller, those of the branches ${}^QP_{21}$, ${}^RQ_{21}$, ${}^SR_{21}$, ${}^OP_{12}$, ${}^PQ_{12}$, ${}^QR_{12}$, ${}^QP_{32}$, ${}^RQ_{32}$, ${}^SR_{32}$, ${}^OP_{23}$, ${}^PQ_{23}$, ${}^QR_{23}$, are greater than in the case of the transition ${}^3\Sigma$–${}^3\Pi$ having the same coupling

*The exact expression for $C_1(J)$ is the following $C_1(J) = 2Y(Y-4)(J-1)(J+2) + (2J+1)(J-2)J(J+2)+2(Y-2)u_1-4Y(Y-4)+8J$ but the simple form used in the text is satisfactory. A similar formula holds in the case of $C_3(J)$.

†Schlapp (1932) has dealt with the transition ${}^1\Sigma$–${}^3\Delta(b)$, but since he had interchanged two columns of the transformation matrix of the ${}^3\Delta(b)$ term, his results are not correct.

‡In case of inverted terms P_1, Q_1, R_1, ${}^RP_{31}$, ${}^SQ_{31}$, ${}^TR_{31}$ takes the place of ${}^NP_{13}$, ${}^OQ_{13}$, ${}^PR_{13}$, P_3, Q_3, R_3.

constant Y. This comparison helps to recognize the kind of transition since the method of the missing lines in the neighborhood of the zero gap is not always applicable because of too much overlapping.

The author is deeply indebted to Dr. G. Herzberg for suggesting the problem.

REFERENCES

HERZBERG, G. Private communication.
KOVÁCS, I. 1958. Can. J. Phys. **36**, 309.
KRONIG, R. DE L. 1927. Z. Physik, **45**, 458.
SCHLAPP, R. 1932. Phys. Rev. **39**, 806.
VAN VLECK, J. H. 1934. Astrophys. J. **80**, 161.

NOTES

THE RELATIVE ABUNDANCES OF COSMIC RAY NUCLEI OF CHARGE $Z > 3$*

I. J. VAN HEERDEN† AND B. JUDEK

The charge spectrum of heavy nuclei in the primary cosmic radiation has been the subject of a large number of investigations. In recent years stacks of nuclear emulsions have been exposed at very high altitudes, and as a result general agreement has been reached that the flux of light nuclei ($3 \leqslant Z \leqslant 5$) is not negligible at the top of the atmosphere. However, disagreement still exists on the exact abundances of the various groups of nuclei, and much of this uncertainty is due to the extrapolation of the experimentally determined fluxes to the top of the atmosphere.

For the present results, a stack of 72 Ilford G5 stripped emulsions, 12 in. $\times$9 in.$\times$600 μm, was flown from Brownwood, Texas (geomagnetic latitude, 41° N.), on March 9, 1958, for 7.5 hours at a ceiling height of 136,000 feet. The residual pressure for this height is 2.7 g/cm^2. With the packing material surrounding the stack the total amount of matter above the emulsions was equal to 3.2 g/cm^2, which is less than in previous investigations. Less extrapolation is therefore necessary to obtain the fluxes at the top of the atmosphere.

All the emulsions were scanned along a line 5 mm below the top edge for tracks with grain densities at least six times that at minimum ionization. The tracks selected for measurement had to have a minimum projected length of 7 mm per emulsion sheet and a zenith angle $\theta \leqslant 80°$. In order to estimate the efficiency of scanning for Li tracks about one quarter of the stack was scanned by an experienced observer. A comparison with the relative numbers of tracks found by other scanners makes us believe that no Li tracks were missed. To distinguish the Li tracks from those of slowing down α-particles all the suspected Li tracks were followed until they either interacted or left the stack. A total of 612 tracks satisfying the selection criteria were found.

Since the cutoff energy at a geomagnetic latitude of 41° N. is about 1.5 Bev/nucleon, all the primary nuclei entering the stack are relativistic. In principle one ionization measurement should therefore be sufficient for a charge determination. In the present results, however, both the δ-ray density and gap density of each track with a nuclear charge $Z \leqslant 10$ were determined. At least 150 δ-rays of four grains or more and 600 gaps in specified depth regions of the emulsion were counted on each track. These measurements were carried out by two observers working independently, one using a Koristka R4 and the other a Leitz microscope. The results of each observer were calibrated with the aid of charge-indicating interactions, and it was found that the δ-ray calibrations were exactly the same for both observers, whereas the gap

*Issued as N.R.C. No. 5687.

†National Research Council Postdoctorate Fellow. Now at National Physical Research Laboratory, Pretoria, South Africa.

densities differed by about 10%. This was due to the different optical conditions of the two microscopes. The results of each observer were, however, self-consistent.

Figure 1 shows the combined normalized results of the two observers. The charge resolution is good up to $Z = 6$. Nevertheless, several tracks falling near the borderline between the boron and carbon groups have been cross-

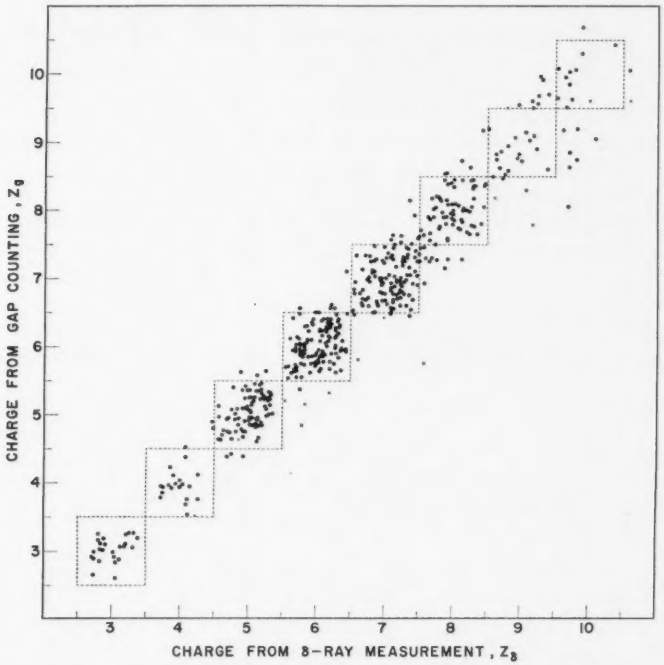

FIG. 1. Comparison of the charge determination by δ-ray density and gap density measurements. The crosses in the figure represent tracks for which the measurements could not be carried out in the specified depth regions of the emulsion.

checked by both observers. No significant differences were found. Table I gives the numbers of light ($3 \leqslant Z \leqslant 5$), medium ($6 \leqslant Z \leqslant 9$), and heavy ($Z \geqslant 10$) nuclei in different zenith angle intervals. They are also expressed as percentages of the total numbers of nuclei in each interval. Table II gives the same results corrected for loss of tracks due to interactions occurring in the emulsions above the scan line and also for particles which entered the stack during ascent and descent (Waddington 1956). Finally, Table III gives the total numbers of light, medium, and heavy nuclei in the interval $0° \leqslant \theta \leqslant 60°$ corrected to the top of the atmosphere using the Bristol fragmentation probabilities published by Rajopadhye and Waddington (1958). These numbers are also given as absolute fluxes and as percentages.

TABLE I

Observed numbers of nuclei in different charge groups

Zenith angle interval	Observer	Light nuclei		Medium nuclei		Heavy nuclei	
		Number observed	Percentage of total	Number observed	Percentage of total	Number observed	Percentage of total
$0° \leqslant \theta \leqslant 30°$	A	32	18±3	121	67±8	27	15±3
	B	37	23±4	91	58±8	30	19±4
	A + B	69	20±3	212	63±5	57	17±2
$30° \leqslant \theta \leqslant 60°$	A	33	28±5	64	54±8	22	18±4
	B	22	22±5	63	62±10	16	16±4
	A + B	55	25±4	127	58±7	38	17±3
$60° \leqslant \theta \leqslant 80°$	A	6	25±11	11	46±17	7	29±13
	B	9	30±11	15	50±16	6	20±9
	A + B	15	28±8	26	48±11	13	24±7

TABLE II

Numbers of nuclei in different charge groups corrected to the top of stack and for ascent and descent

Zenith angle interval	Mean amount of matter, g/cm²	Light nuclei		Medium nuclei		Heavy nuclei	
		Number	Percentage of total in interval	Number	Percentage of total in interval	Number	Percentage of total in interval
0°–30°	3.35	63.2	20±3	198.9	63±5	55.3	17±2
30°–60°	4.52	51.7	24±4	122.2	58±7	37.9	18±3
60°–80°	8.96	15.0	27±8	26.9	48±11	14.1	25±7
0°–60°	3.82	114.9	22±2	321.1	61±4	93.2	18±2

TABLE III

Fluxes of nuclei in different charge groups at the top of the atmosphere

	Light nuclei	Medium nuclei	Heavy nuclei
Total number of nuclei ($0° < \theta < 60°$)	111.5	351.9	108.3
Absolute flux in particles/m² sec sterad	1.14±0.11	3.60±0.19	1.11±0.11
Relative abundance (%)	20±2	62±4	19±2

The value of 0.20±0.02 obtained for the relative abundance of light nuclei is in experimental agreement with the results of Bristol (Waddington 1957), Chicago (Koshiba *et al.* 1958), Rochester (Engler *et al.* 1958), Minnesota (Freier *et al.* 1959), Washington (O'Dell *et al.* 1959), and Torino (Garelli *et al.* 1960). On the other hand, it is inconsistent with the value of about 0.05 obtained by Appa Rao *et al.* (1958) and the value 0.30 of Noon *et al.* (1957). The absolute fluxes are considerably lower than those obtained by previous observers in stacks flown over Texas. This could perhaps be attributed to the fact that the present flight took place during a period of low cosmic ray intensity.

We are now following all the primary and secondary tracks until they either interact or leave the stack. Full details of the present work, including the fragmentation probabilities obtained, will be published at a later date.

Appa Rao, M. V. K., Biswas, S., Daniel, R. R., Neelakantan, K. A., and Peters, B. 1958. Phys. Rev. **110**, 751.
Engler, A., Kaplon, M. F., and Klarmann, J. 1958. Phys. Rev. **112**, 597.
Freier, P. S., Ney, E. P., and Waddington, C. J. 1959. Phys. Rev. **113**, 921.
Garelli, C. M., Quassiati, B., and Vigone, M. 1960. Nuovo Cimento, **15**, 121.
Koshiba, M., Schultz, G., and Schein, M. 1958. Nuovo Cimento, **9**, 1.
Noon, J. H., Hertz, A. J., and O'Brien, B. J. 1957. Nuovo Cimento, **5**, 854.
O'Dell, F. W., Shapiro, M. M., and Stiller, B. 1959. Paper presented at the International Union of Pure and Applied Physics Conference, Moscow, U.S.S.R.
Rajopadhye, V. Y. and Waddington, C. J. 1958. Phil. Mag. **3**, 19.
Waddington, C. J. 1956. Nuovo Cimento, **6**, 748.
Waddington, C. J. 1957. Phil. Mag. **2**, 1059.

Received April 1, 1960.
Division of Pure Physics,
National Research Council,
Ottawa, Canada.

TRIBOLUMINESCENCE IN A MERCURY BUBBLER

L. J. Schoen

Weak light emission may be observed when various gases are allowed to bubble through a depth of several millimeters of mercury contained in a pyrex glass or quartz vessel at atmospheric pressure. The glowing region appears to consist of numerous small flashes of light occurring up to several centimeters above the surface of the liquid depending on the value of the gas flow rate.

Using an $f/0.625$ glass transmission grating spectrograph and an $f/4$ quartz prism instrument, the spectra associated with the observed luminosity has been photographed and identified.

The production of luminosity did not appear to depend critically on the design or dimensions of the mercury bubbler. The two types of bubbler used are shown in Fig. 1. The brightest emission occurred when helium and argon

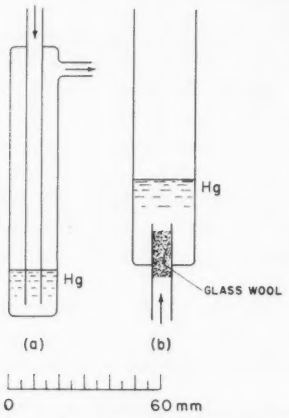

FIG. 1. Two forms of mercury bubbler.

were employed as the bubbling gases. In the experiments with helium, the most intense spectral features were found to be due to a 0.02% air impurity initially present in the gas.* These spectra consisted of the bands of N_2^+ ($B^2\Sigma_u^+ \rightarrow X^2\Sigma_g^+$), the second positive system of N_2 ($C^3\Pi_u \rightarrow B^3\Pi_g$), and bands of OH ($A^2\Sigma^+ \rightarrow X^2\Pi$). The resonance line of Hg I ($^3P_1 \rightarrow {}^1S_0$) also appeared with relatively high intensity. Weaker features due to transitions from upper levels of He I requiring in excess of 21 ev for their excitation and from levels of Hg I above ^3P were also identified. The bands of N_2^+ were missing when argon was used as the bubblant, otherwise the emission corresponded to that observed for helium.

Wavelengths and relative intensities of these spectra are given in Table I. Intensities are visual estimates of plate blackening on an arbitrary scale of 1 to 600. An intensity of 1 indicates a faint trace after a 5-hour exposure with the $f/0.625$ spectrograph used with 103 a–F film. An intensity of 600 is associated with the strongest feature which can just be photographed in 20 minutes with the $f/4$ spectrograph employing 103 a–O plates. The spectral features photographed with the quartz optics are illustrated in Figs. 2*a* and 2*c*. With nitrogen as the bubbling gas, the second positive system of N_2 as well as spectra of OH and Hg I appeared; however, the emission was weaker than for either helium or argon. With ethane as the bubblant, the resulting luminosity was too feeble for spectra to be obtained conveniently.

*I should like to thank Dr. John Herron of N.B.S. for the mass spectrometer analysis.

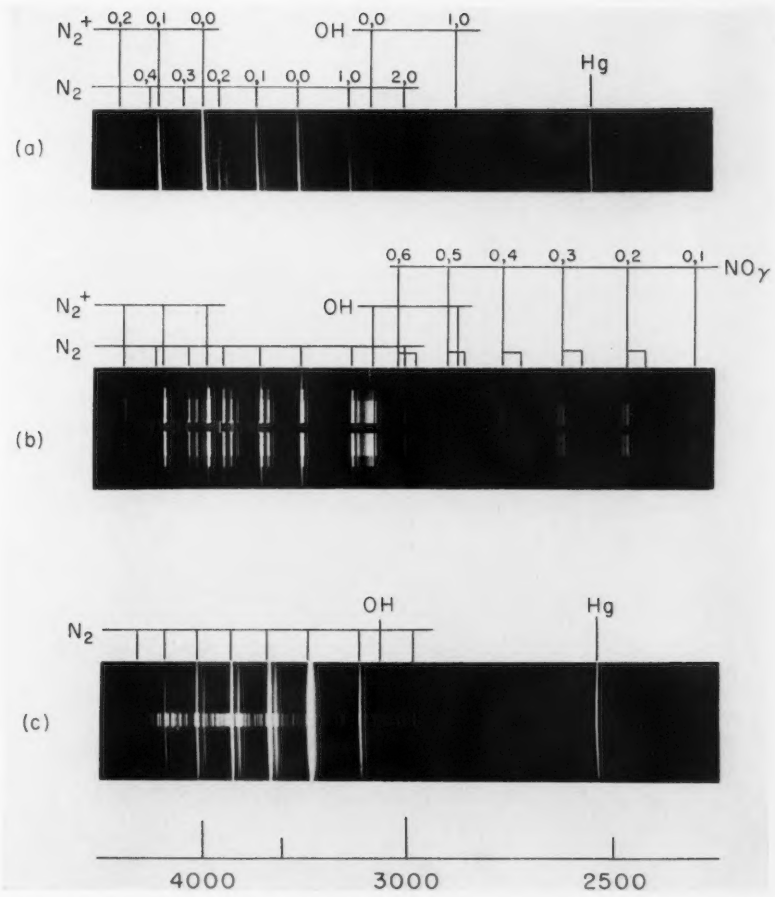

FIG. 2. Mercury bubbler and Tesla discharge spectra.
(*a*) Mercury bubbler with helium; exposure 10 hours; *f*/4 quartz spectrograph.
(*b*) Tesla discharge through helium at atmospheric pressure; exposure 1 minute, 3 minutes, 9 minutes; *f*/4 quartz spectrograph.
(*c*) Mercury bubbler with argon; exposure 8 hours; *f*/4 quartz spectrograph.

TABLE I

Spectra observed in the mercury bubbler with a helium bubblant

Wavelength,[a] Å	Intensity	Identification	
		$N_2(C^3\Pi \rightarrow B^3\Pi)$ (v', v'')	Other
2537	300		$Hg(^3P_1 \rightarrow {}^1S_0)$
2953	10	4, 2	
2962	10	3, 1	
2977	20	2, 0	
3064	45		$OH(A^2\Sigma^+ \rightarrow X^2\Pi)$ 0, 0 R_2
3067	70		$OH(A^2\Sigma—X^2\Pi)$ 0, 0 R_1
3089	75		$OH(A^2\Sigma—X^2\Pi)$ 0, 0 Q_1
3136	60	2, 1	
3159	100	1, 0	
3285	10	3, 3	
3309	10	2, 2	
3339	15	1, 1	
3371	400	0, 0	
3500	20	2, 3	
3537	100	1, 2	
3577	300	0, 1	
3650	3		$Hg(^3D_3 \rightarrow {}^3P_2)$
3672	20	3, 5	
3710	50	2, 4	
3755	100	1, 3	
3805	150	0, 2	
3914	600		$N_2^+(B^2\Sigma_u^+ \rightarrow X^2\Sigma_g^+)$ 0, 0
3943	45	2, 5	
3999	70	1, 4	
4047	m		$Hg(^3S_1 \rightarrow {}^3P_0)$
4059	70	0, 3	
4200	25	2, 6	
4270	m	1, 5	
4278	400	0, 4	$N_2^+(B^2\Sigma_u^+ \rightarrow X^2\Sigma_g^+)$ 0, 1
4344	30		
4358	m		$Hg(^3S_1 \rightarrow {}^3P_1)$
4709	200		$N_2^+(B^2\Sigma_u^+ \rightarrow X^2\Sigma_g^+)$ 0, 2
5016	1		$He(3p^1P^0 \rightarrow 2s^1S)$
5461	3		$Hg(^3S_1 \rightarrow {}^3P_2)$
5770	1		$Hg(^3D_2 \rightarrow {}^1P_1)$
5790	1		$Hg(^3D_1 \rightarrow {}^1P_1)$
5876	6		$He(3d^3D \rightarrow 2p^3P_2^0)$
6678	8		$He(3d^1D_2 \rightarrow 2p^1P_1^0)$

NOTE: m = masked.
[a]Tabulated wavelengths (Pearse and Gaydon 1950; Harrison 1939).

The observed emission is an example of triboluminescence initiated by the hydrodynamic interaction between a flowing gas and a liquid. In the mercury bubbler, electrostatic charging of mercury droplets is known to take place by means of a series of complex processes inherent in bubble formation and disintegration (Harper 1957). In the present case, the luminosity is almost entirely confined to the region near the vessel wall (most clearly seen in the bubbler of Fig. 1*b*), although at pressures of a few millimeters of mercury where the breakdown potential of the gas is reduced, the glowing region is seen to spread throughout the volume of the vessel in a manner characteristic of an electrical discharge process. It appears that a discharge between a charged droplet and the surrounding silica surface is the source of the luminosity

described above. An electrical discharge between the liquid and the vessel wall as a result of frictional charging of the liquid due to its mechanical motion relative to the wall is also thought to be a significant process. The hypothesis of a discharge mechanism as the source of luminosity is further supported by Tesla coil excitation of the same helium–air mixture at atmospheric pressure. Except for the occurrence of the NO_γ system, the spectra of this source (Fig. 2*b*) correspond to the spectra obtained from the mercury bubbler. Since collisional deactivation processes are likely to be important at atmospheric pressure, the observed decrease in luminescence intensity with increasing complexity of the flowing gas is probably a reflection of the relative deactivation efficiencies associated with each of the gaseous species employed.

The observation of bands of N_2^+ in the bubbler with helium as the bubblant but not with argon implies that metastable rare gas atoms act as an intermediate species in the transfer of energy to the nitrogen molecule. In order to excite radiation from the $B^2\Sigma_u^+$ state of N_2^+, at least 18.8 ev are necessary—15.6 ev for the ionization of N_2 and 3.2 ev for the excitation of the resulting ion. The required energy is not available from collisions involving metastable argon in the $J = 0$ of $J = 2$ levels of its first excited state but it could be readily supplied by collision with helium in the long lived $^3S_1$ level lying 19.8 ev above the ground state of the atom.

HARPER, W. R. 1957. Advances in Phys. **6**, 365.
HARRISON, G. R. 1939. M. I. T. wavelength tables (John Wiley & Sons, Inc., New York).
PEARSE, R. W. B. and GAYDON, A. G. 1950. The identification of molecular spectra (Chapman & Hall, Ltd., London).

RECEIVED FEBRUARY 1, 1960.
NATIONAL BUREAU OF STANDARDS,
WASHINGTON, D.C.

LETTERS TO THE EDITOR

Under this heading brief reports of important discoveries in physics may be published. These reports should not exceed 600 words and, for any issue, should be submitted not later than six weeks previous to the first day of the month of issue. No proof will be sent to the authors.

Frequency Measurement of Standard Frequency Transmissions[1,2]

Measurements are made at Ottawa, Canada, using N.R.C. caesium-beam frequency resonator as reference standard (with an assumed frequency of 9 192 631 770 c.p.s.). Frequency deviations from nominal are quoted in parts per 10^{10}. A negative sign indicates that the frequency is below nominal.

Date, April 1960	MSF, 60 kc/s	GBR, 16 kc/s		WWVB 60 kc/s
		5½-hour average*	24-hour average	
1	−175	−168	−167	−80
2	−172	−175	−170	N.M.
3	−162	−172	−167	N.M.
4	−154	−167	−164	−78
5	−164	−167	−166	−79
6	−159	−171	−173	−80
7	−143	−167	−169	−81
8	−173	−164	−162	−79
9	−163	−166	−163	N.M.
10	−174	−172	−172	N.M.
11	−160	−176	−174	−82
12	−172	−167	−160	−82
13	−170	−169	−168	−79
14	−170	−166	−162	N.M.
15	N.M.	−173	−171	N.M.
16	N.M.	−174	N.M.	N.M.
17	N.M.	N.M.	N.M.	N.M.
18	N.M.	N.M.	N.M.	N.M.
19	N.M.	N.M.	N.M.	N.M.
20	−153	−158	N.M.	−79
21	N.M.	N.M.	N.M.	N.M.
22	−155	N.M.	N.M.	−79
23	−153	−157	−155	N.M.
24	−157	−154	−151	N.M.
25	N.M.	−155	N.M.	N.M.
26	N.M.	N.M.	N.M.	−78
27	−143	−149	−146	−75
28	−141	−148	−144	N.M.
29	−153	−151	−152	N.M.
30	−142	−141	−138	N.M.
Midmonthly mean	−159	−163	−160	−79
Midmonthly mean of WWV	−151			

NOTE: N.M. no measurement.
*Time of observations: 00.30 to 04.00 U.T.
11.00 to 13.00 U.T.

RECEIVED MAY 16, 1960.
S. N. KALRA
DIVISION OF APPLIED PHYSICS,
NATIONAL RESEARCH COUNCIL,
OTTAWA, CANADA.

[1]Issued as N.R.C. No. 5746.
[2]Cf. Kalra, S. N. 1959. Can. J. Phys. 37, 1328.

Experimentally Measured Vibrational Levels in H_2^+

An electron selector has been used to obtain experimental values for the separation of some vibrational levels in N_2^+, NO^+, and H_2^+. These are believed to be the first such measurements made using electron bombardment techniques. The results on H_2^+ are of particular interest because no spectroscopic data exists for this, the simplest molecular structure.

The lower curve in Fig. 1 represents the potential energy diagram of the neutral hydrogen molecule. Using a Morse function for the potential, the levels of the various vibrational states may be calculated by quantum mechanical methods (e.g. Herzberg 1950). These theoretical values have been verified by spectroscopic observations (e.g. Richardson 1934). The waves on the various levels represent qualitatively the probability of the nuclear separation. At ordinary mass spectrometer source temperatures, the population of the first excited level in neutral hydrogen is negligible, the molecules being in the ground state ($v'' = 0$).

The upper curve in Fig. 1 represents the potential energy diagram of H_2^+. This has been calculated theoretically for a Morse function (Hylleraas 1931) and the vibrational levels established. These values agree with those calculated by extrapolation of the observed

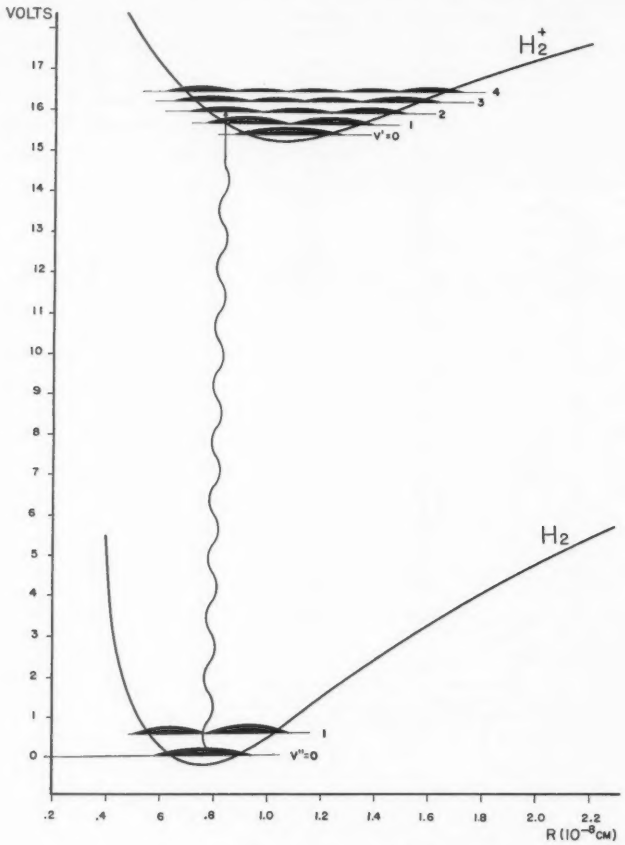

FIG. 1. Vibrational energy states of H_2 and H^+.

vibrational levels for various excited states of the neutral hydrogen molecule (e.g. Richardson 1929). However, no direct experimental measurements have been made of these levels. The probable values of nuclear separation are indicated qualitatively for several levels by wavy lines.

Appearance potential measurements of the H_3^+ ion formed from H_2 by electron bombardment have been made using the electrostatic electron selector (Marmet and Kerwin 1960). Several typical curves are shown in Fig. 2, where the H_3^+ ion current has been recorded as a function of the electron energy. Since the energy spread of the selector beam is about 0.03 ev, relatively sharp breaks are obtained, and a number of them are seen to be separated by about 0.25 ev.

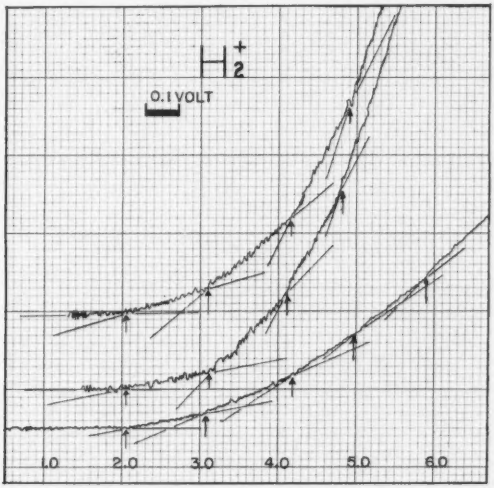

FIG. 2. Appearance potential curves for H_3^+.

Average values of the differences in electron energy required to produce successive breaks were taken from 20 runs. They are here compared with the differences between the first six vibrational levels as calculated from Richardson's constants (Herzberg 1950).

SELECTOR	THEORETICAL
	$v = 1$, 0.269 ev
A 0.27±0.02 ev	2, 0.253 ev
B 0.25±0.02 ev	3, 0.237 ev
C 0.23±0.02 ev	4, 0.221 ev
D 0.21±0.02 ev	5, 0.208 ev
	6, 0.192 ev

Our selector values clearly show the narrowing vibrational intervals. While our experimental error does not permit unambiguous assignment, the intervals appear to correspond to the first vibrational levels.

As may be noted in Fig. 1, the most probable transition from the ground state of the molecule to the ion is not to the first vibrational level, but to one such that a probable nuclear separation is equal to that in the molecule (Franck–Condon principle). There is a certain probability for transition to nearby levels. Experimentally, the probabilities may be calculated from the slopes of the appearance potential curve segments. In our case, the relative probabilities were:

to A: 0.4, B: 0.6, C: 1.0, D: 0.7.

This confirms the general picture of Fig. 1, and the fact that the nuclear separation is greater for the ion than the molecule. If our first level is indeed the ground one, then the most probable transition lies 0.75 ev above the theoretical 15.4-ev jump from the molecular ground to the ionic ground state. Such a value of 16.1 ev has been frequently observed, and our values agree with Bleakney's analysis of the conflicting data on the appearance potential of H_3^+ (Bleakney 1932).

BLEAKNEY, W. 1932. Phys. Rev. **40**, 496.
HERZBERG, G. 1950. Spectra of diatomic molecules (D. Van Nostrand Company, Inc., New York).
HYLLERAAS, E. A. 1931. Z. Physik, **71**, 739.
MARMET, P. and KERWIN, L. 1960. Can. J. Phys. **38**, 787.
RICHARDSON, O. W. 1929. Trans. Faraday Soc. **25**, 686.
——— 1934. Molecular hydrogen and its spectrum (Yale University Press, New Haven).

RECEIVED APRIL 22, 1960.
PAUL MARMET AND LARKIN KERWIN
CENTRE DE RECHERCHES EN PHYSIQUE,
UNIVERSITÉ LAVAL, QUÉBEC.

THE PHYSICAL SOCIETY

MEMBERSHIP of the Society is open to all who are interested in Physics.

FELLOWS pay an Entrance Fee of £1 1*s*. ($3.15) and an Annual Subscription of £2 2*s*. ($6.00).

STUDENTS: A candidate for Studentship must be between the ages of 18 and 26, and pays an Annual Subscription of 5*s*. ($0.75).

MEETINGS: Fellows and Students may attend all Meetings of the Society including the annual Exhibition of Scientific Instruments and Apparatus.

PUBLICATIONS include the *Proceedings of the Physical Society*, published monthly, £12 12*s*. ($36.00) per annum, and *Reports on Progress in Physics*, published annually. Volume XXII, 1959, is now available (price £3 3*s*. ($9.45)). Members are entitled to receive any of the Publications at a reduced rate.

Further information can be obtained from:

THE PHYSICAL SOCIETY
1, LOWTHER GARDENS, PRINCE CONSORT ROAD
LONDON, S.W.7, ENGLAND

NOTES TO CONTRIBUTORS

Canadian Journal of Physics

MANUSCRIPTS

General.—Manuscripts, in English or French, should be typewritten, double spaced, on paper 8½×11 in. **The original and one copy are to be submitted.** Tables and captions for the figures should be placed at the end of the manuscript. Every sheet of the manuscript should be numbered. Style, arrangement, spelling, and abbreviations should conform to the usage of recent numbers of this journal. Greek letters or unusual signs should be written plainly or explained by marginal notes. Characters to be set in boldface type should be indicated by a wavy line below each character. Superscripts and subscripts must be legible and carefully placed. Manuscripts and illustrations should be carefully checked before they are submitted. Authors will be charged for unnecessary deviations from the usual format and for changes made in the proof that are considered excessive or unnecessary.

Abstract.—An abstract of not more than about 200 words, indicating the scope of the work and the principal findings, is required, except in Notes.

References.—References should be listed **alphabetically by authors' names,** unnumbered, and typed after the text. The form of the citations should be that used in current issues of this journal; in references to papers in periodicals, titles should not be given and only initial page numbers are required. The names of periodicals should be abbreviated in the form given in the most recent *List of Periodicals Abstracted by Chemical Abstracts.* All citations should be checked with the original articles and each one referred to in the text by the authors' names and the year.

Tables.—Tables should be numbered in roman numerals and each table referred to in the text. Titles should always be given but should be brief; column headings should be brief and descriptive matter in the tables confined to a minimum. Vertical rules should not be used. Numerous small tables should be avoided.

ILLUSTRATIONS

General.—All figures (including each figure of the plates) should be numbered consecutively from 1 up, in arabic numerals, and each figure referred to in the text. The author's name, title of the paper, and figure number should be written in the lower left corner of the sheets on which the illustrations appear. Captions should not be written on the illustrations.

Line drawings.—Drawings should be carefully made with India ink on white drawing paper, blue tracing linen, or co-ordinate paper ruled in blue only; any co-ordinate lines that are to appear in the reproduction should be ruled in black ink. Paper ruled in green, yellow, or red should not be used. All lines must be of sufficient thickness to reproduce well. Decimal points, periods, and stippled dots must be solid black circles large enough to be reduced if necessary. Letters and numerals should be neatly made, preferably with a stencil (**do NOT use typewriting**) and be of such size that the smallest lettering will be not less than 1 mm high when the figure is reduced to a suitable size. Many drawings are made too large; originals should not be more than 2 or 3 times the size of the desired reproduction. Whenever possible two or more drawings should be grouped to reduce the number of cuts required. In such groups of drawings, or in large drawings, full use of the space available should be made; the ratio of height to width should conform to that of a journal page (4¾×7½ in.), but allowance must be made for the captions. **The original drawings and one set of clear copies (e.g. small photographs) are to be submitted.**

Photographs.—Prints should be made on glossy paper, with strong contrasts. They should be trimmed so that essential features only are shown and mounted carefully, with rubber cement, on white cardboard, with no space between those arranged in groups. In mounting, full use of the space available should be made. **Photographs are to be submitted in duplicate;** if they are to be reproduced in groups one set should be mounted, the duplicate set unmounted.

REPRINTS

A total of 100 reprints of each paper, without covers, are supplied free. Additional reprints, with or without covers, may be purchased at the time of publication.

Charges for reprints are based on the number of printed pages, which may be calculated approximately by multiplying by 0.6 the number of manuscript pages (double-spaced typewritten sheets, 8½×11 in.) and including the space occupied by illustrations. Prices and instructions for ordering reprints are sent out with the galley proof.

Contents

M. J. Laubitz—Thermal and electrical properties of Armco iron at high temperatures - 887

W. G. Henry and J. L. Rogers—The magnetic susceptibilities of some diamagnetic alloys. The primary solid solutions of cadmium, indium, tin, and antimony in copper and in silver; zinc, gallium, germanium, and arsenic in silver; copper in silver and silver in copper - - - - - - - - - 908

A. E. Litherland and G. J. McCallum—An illustration of a type of triple correlation measurement which can be easily interpreted - - - - - - 927

Richard Stevenson—Magneto-optical rotation in very high fields - - - - 941

T. J. Kennett and H. G. Thode—Diffusion phenomena and isotope effects in the extraction of fission-product xenon and krypton from irradiated U_3O_8 945

I. Kovács—Intensities in $\Sigma-\Delta$ and $\pi-\Delta$ transitions of diatomic molecules - 955

Notes:

I. J. van Heerden and B. Judek—The relative abundances of cosmic ray nuclei of charge $Z \geqslant 3$ - - - - - - - - - - - - - - - - - - 964

L. J. Schoen—Triboluminescence in a mercury bubbler - - - - - - 967

Letters to the Editor:

S. N. Kalra—Frequency measurement of standard frequency transmissions 971

Paul Marmet and Larkin Kerwin—Experimentally measured vibrational levels in H_2^+ - 972

Printed in Canada *by* University of Toronto Press